UNIVERSITY OF NAPLES "FEDERICO II"

FACULTY OF ENGINEERING

SPACE SCIENCE AND ENGINEERING DEPARTMENT
"LUIGI G.NAPOLITANO"

XIX PhD Course on Aerospace, Naval and Quality Engineering

Development, installation, calibration and data processing of airborne instruments for remote sensing and in-situ measurements

Tutor:
Ch.mo Prof.
ANTONIO MOCCIA

Co-tutor:
Dott.
VINCENZO MAGLIULO

PhD Student:
Dott.Ing.
MARCO ESPOSITO

Academic year 2005 – 2006
COORDINATOR: Ch.mo Prof. ANTONIO MOCCIA

ACKNOWLEDGMENTS

In the first instance, I must tank at my family that are always very close to me, and support me since I was a child.

Next, I tank at the ERALab staff of the CNR ISAFoM where this thesis was carried out, in particular at Maurizio, Paolo and Silvia for their patience and support me every day during my activity. I have to say thank at my supervisor Enzo for providing with the opportunity to be free to explore my research interest.

Chapter 1

INTRODUCTION

1.1 Introduction and thesis outline

The research work presented focuses on several aspects of the methodologies and technologies that are correlated with the use of the two SkyArrow's 650 TCNS ERA (Environmental Research Aircraft), operated by the "*Mediterranean agricultural and forest ecosystems institute*" of the Italian "*National Research Council*" of Naples.

Measurements in the Planetary boundary layer (PBL) are the main subject for the use of the environmental research aircraft. The PBL is the part of the atmosphere that is mostly influenced by the earth's surface and so responds to surface forcing with a timescale of less than one hour. It is beginning near the ground and reaching up to a maximum of 3 km as defined by Stull (1988). Within the PBL the air flow can be assumed as permanently turbulent with vertical and horizontal wind components, enabling a transport of heat and gases.

With the measurement of temperature, humidity and gas concentrations in the PBL it is possible to calculate heat fluxes and mass budgets for gas transports (see Appendix A). Those results are needed for validations of the respiration and gas and heat exchanges of vegetation and therewith improvements on fertilization and ground treatments in agriculture. They also help to get an idea about the interactions of atmosphere and soil related to the size of the considered area.

Wind components are vital for calculating any atmospheric fluxes as well as the location of the measurement with its specific vegetation and conditions.

High resolution images in the visible, near-infrared and thermal infrared domain also allow to derive relevant indicators of crop water demand on an area of regional extent by use of

Normalized Difference Vegetation Index (NDVI) to calculate map crop coefficients, and also on the potential benefit of advanced indicators, like the evaporative fraction sometimes used for crop water stress recognition (Menenti and Choudhury, 1993; Su, 2002).

   The thesis is composed by two major parts: part I focuses on remote sensing, part II focuses on in-situ measurements issues.

   Chapter one gives an introduction on the atmospheric boundary layer (Pisani, 2005) and on the use of small aircrafts to probe it (Crawford et al, 1992). *Chapter two* gives an overview on the observing platform, from the point of view of the SkyArrow as an aircraft and on the "Mobile Flux Platform" to familiarize the reader with sensors installed onboard (NOAA technical draft; sensors datasheets).

   With *chapter Three* starts the section regarding remote sensing issues; after a general introduction both on remote sensing and on passive optical sensors (Rees, 2001), the developing of a small, rugged system in PC104 form factor to manages a set of cameras is described. The work focuses on the engineering process design (NASA, 1995; Arin 2002) of the system following requirements provided by both the type of the images to acquire and the standard nominal remote sensing mission performed by the skyarrow aircraft. The test and some of the campaigns performed by the aircraft during both national and European research project are present as examples.

   The *chapter four* describes the laboratory calibration of the thermal camera FLIR A40M by means of the MIKRON black body source as a reference. The chapter starts with an introduction on the uncooled microbolometer technology (Lentz, 1998) used by the camera, and lists the commonly parameters used in literature to characterize detectors (Legrand et al, 2000; Slater, 1996; Sensor Inc, 2004). A brief explanation of the physical laws used to manage the radiometric quantity are done. After that the experiment performed at "*Laboratoire des Sciences de l'Image, de l 'Informatique et de la Télédétection* (LSIIT) "of "*Louis Pasteur*" university in Strasbourg is described and the results are shown.

   With *chapter five* begin the section focused on the in-situ measurements issues. The three-dimensional wind vector is computed by taking the vector sum of the aircraft relative air velocity and the ground-relative aircraft velocity (French et al, 2006; Ekman et al; 1999; Lenschow, 1986, Leise and Maters, 1991). The theory of the subsonic potential flow past a sphere (Eckman et al, 1999; Leise and Masters, 1991;Brown et al; 1983) is presented as a preamble to the calculation of the angle of attack and sideslip, dynamic and static pressure and then the true air speed of the aircraft. The above quantities are referred at the aircraft

coordinate system, to rotate them in the earth coordinate system the blending in frequency space by taking the Fourier transform technique (Ekman et al, 1999) to recover the attitude angles at the right frequency is presented and the results on a test data set is shown. The same technique is presented to recover the GPS data velocity from the low frequency of the acquisition to the adequate frequency needed to calculate the wind vector.

The *chapter six* regards static (wind tunnel) and dynamic calibration and systems performance tests conducted by evaluating the computed wind vector during certain prescribed flight maneuvers (French et al, 2006; Lenschow, 1986; Tjernstrom and Friehe, 1991; Boghel and Baumann, 1991). A calibration flight performed in the 2005 is reported, consideration on the state on the atmospheric boundary layer by means of vertical profile and data results are shown.

1.2 Light aircraft to probe the PBL

Aircraft have had a long history of use far meteorological research. Indeed, the history of aircraft closely parallels the history of meteorology. This is not surprising, since flying requires accurate weather information and, conversely, aircraft provide a convenient and unique platform far collecting meteorological information. Thirty years ago, before the widespread use of pressurized aircraft, a large fraction of aircraft flight lime was within the boundary layer. Even now, commercial jet aircraft must at least pass through the boundary layer on takeoff and landing. Thus, the structure of the boundary layer is stilI very relevant to the needs of aviation. At the same time, developments in aviation technology have led to improved tools far observing the planetary boundary layer (PBL) from aircraft.

One of the major advantages of an aircraft as a boundary layer measurement platform is its mobility. An aircraft can probe the entire depth of the boundary layer (with the exception of the Iowest 15 m or so) and can obtain statistically significant measurements about an order of magnitude faster than possible with direct fixed-point measurements. Furthermore, an aircraft can be used far either vertical profiling or horizontal traverses, or some combination of the two. Compared to fixed-point observations, which are limited to sampling air advected by the wind, aircraft can measure along a path at any arbitrary angle with respect to the wind, and can measure in a frame of reference that moves with the wind.

Unfortunately, an aircraft's mobility also creates some disadvantages. The aircraft motion needs to be accurately measured and corrections need to be applied to the data. Furthermore, most aircraft need to fly relatively fast (compared to the wind) in order to stay airborne. Therefore, corrections need to be applied far compressibility, adiabatic heating, and flow distortion induced by the aircraft. This complicates the use of aircraft and the subsequent analysis of aircraft data. Furthermore, aircraft are not suitable far long-time-series measurements. Thus, fixed-point measurements (towers, tethered balloons, etc.) are, in many cases, complementary to aircraft measurements. A large array of sensors have been flown on aircraft far research in the boundary layer. Various are the types of instrumentation used on aircrafts, and various are the problems associated with the measurements.

With the advent of systems (INS and GPS) to measure attitude, velocity and position, aircraft motion could be measured. In particular, motion-induced errors could now be removed from wind measurements (Lenschow 1986), however, large flow distortion errors still remained (Wynyard et al. 1985; Wyngaard 1988; Crawford et al. 1996). Throughout the

1970's and early 1980's, scientists rapidly developed new research sensors to probe the atmosphere and view the Earth's surface. These state-of-the-science sensors still lacked microprocessor controllers. Thus, large aircraft were still required. Since mid-1980, impressive advances have been made in the development of smaller, faster, and more powerful microprocessors. Phenomenal increases in data storage capacity have also been seen. As a result, sensors and data acquisition systems became smaller, lighter, and consumed significantly less power. Advances in navigation systems such as OMEGA/VLF, LORAN-C, and currently global position system (GPS) have followed this same trend. For the first time, large aircraft were not required to carry a heavy payload of sensors, data acquisition systems, and multiple scientists. These emerging technologies have made it possible to use small aircraft for various types of research applications. Large aircraft have a long and distinct history in sciences and have played an important role in many discoveries within the atmosphere. Unfortunately, the flight hour cost for a large multi-engine aircraft has become prohibitive for many applications and efficiency is further reduced by associated logistical complexities. While large aircraft are required for particular applications, there are many measurements that can be made more accurately from much smaller aircraft with state-of-the-science sensors and data acquisition systems at a fraction of the cost. There are several types of small aircraft which are ideally suited for atmospheric research. These airframes are designed to minimize flow distortions that would otherwise corrupt various *in situ* measurements. These aircraft are also capable of flying at low altitudes and at slow speeds, a necessary requirement for air-surface exchange research. In addition, small aircraft are simpler to maintain and operate without sacrifices in safety. The acquisition and operating costs are one to two orders of magnitude *less* than large aircraft.

1.3 Atmospheric temperature profile

The more important part of atmospheric phenomena can be classified with altitude. This feature allows splitting atmosphere in several shells that are defined by variations of some parameters. In particular, atmospheric chemical composition and solar irradiance define surface temperature and its variations with altitude. From temperature profile it can be noted that its value decreases with height with a constant gradient up to tropopause. Usually troposphere top has a maximum over the Earth's equator (from about 15 km to 20 km in winter and summer time, respectively) and a minimum at poles (from about 0 to 10 km in winter and summer time, respectively).
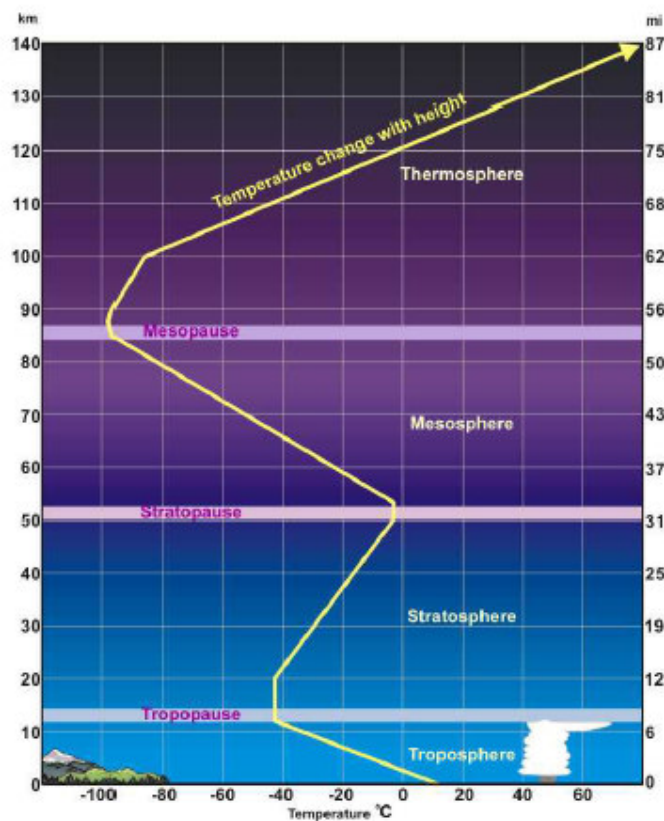
Fig. 1.1 General temperature profile for Standar Atmosphere.

The air mass circulation is driven by heat exchanging with earth surface which happens in the first layer of atmosphere, called planetary boundary layer (PBL); its height changes from about 0.5 km during night time to about 2.5 km in the day. Above PBL, the free troposphere extends up to tropopause. Because of high turbulence, it can be assumed that troposphere is well mixed, which means that, at least for molecular constituents, the fractional composition is constant up to tropopause (actually it the same up to ~100 km). Troposphere is the most

important region for meteorological phenomena and it is the atmospheric shell containing about the 80% of total air mass. Above the tropopause the temperature increases again up to ~50 km and this layer defines the stratosphere.

Because the air temperature in the stratosphere increases with altitude, it does not cause convection but drives to a stabilizing effect in the region. Ozone plays the major role in regulating the thermal regime.

of the stratosphere. In fact, because of photo-chemical reactions, solar radiation in UV range (mainly between 290 and 320 nm) is converted to kinetic energy when O3 molecules absorb ultraviolet radiation resulting in heating of the stratosphere. The following layer is named mesosphere and ranges between ~50 and ~90 Km height. Again the temperature decreases with height reaching a value of -140° C.

Typical clouds in mesosphere are the noctilucent clouds, formed by volcanic or meteoric dusts. Finally, thermosphere is the upper layer, where temperature increases up to 1200°C.

1.4 Atmospheric pressure and density profiles

To describe atmospheric pressure profile, we need to introduce the assumption that the atmosphere is in hydrostatic equilibrium, which means that the forces due to gravity and pressure are balanced. If ρ is the air mass density, g the gravitational acceleration, P(z) is the pressure (in Pascal) at the height z, then:

$$-\frac{1}{\rho(z)}\frac{\partial p_z}{\partial z} = g \qquad (1.1)$$

The standard model (U.S. Standard Atmosphere, 1976) allows neglecting the variations of g with altitude, so that the previous relation can be re-written as:

$$\frac{\partial p_z}{\partial z} = -g\rho(z) \qquad (1.2)$$

that is known as the standard hydrostatic equation. In the first approximation, the (1.2) can be solved introducing the perfect gas low. So, if V is the considered atmospheric volume, T(z) is the temperature at height z, N in the numbers of moles, and R* is gas constant, it results:

$$\rho(z) = \frac{NM}{V} = \frac{M_{air}p(z)}{R^*T} \qquad (1.3)$$

where M_{air} = 28.9 g/mol. Substituting the previous relation into the ep. (1.2) and integrating it from height z = 0 to z = z_0:

$$p(z) = p_0 \exp\left[-\frac{gM_{air}}{R^*T}z\right] \qquad (1.4)$$

where p_0 is the pressure at the sea level, taken to be the standard pressure (760 mm Hg) at standard temperature (15° C).

From the numerical point of view, molecules in Earth atmosphere exceed in number the aerosol particles by several orders of magnitude. In fact, the single molecule scattering processes (both elastic and inelastic) cannot be neglect, even if the cross sections process is smaller than that one corresponding to particles. The fractional volume of the basic molecular constituents of atmosphere is assumed to be the same as long as the height increases up to 100 km. The variation of density can be shown starting again from the perfect gas law:

$$\frac{N}{V}N_A = N_T(z) = \frac{P(z)}{RT(z)}N_A = \frac{P(z)}{k_BT(z)} \tag{1.5}$$

where first and second members are multiplied by Avogadro's number N_A, k_B is the Boltzman constant, and $NT(z)$ is the total number of molecule per cubic meter at the considered altitude z. Afterwards, the numerical density of ith atmospheric molecular component is done by:

$$n_i(z) = f_i N_T(z) \tag{1.6}$$

and them mass density profile will be:

$$\rho_i(z) = \frac{n_i(z)M_i}{N_A} \tag{1.7}$$

Of course, from (1.7) total atmospheric density profile is:

$$\rho(z) = \sum_i \rho_i(z) \tag{1.8}$$

1.5 Planetary Boundary Layer

Boundary Layer is a term defining the moving fluid layer adjacent to a solid body, the Earth's surface.

The definition of a fluid is often based on property of resistance to rate of shear as a material that deforms continuously and permanently under the application of a shearing stress, no matter how small it is. Viscosity is formally defined as the ratio between the shear stress and the shear rate. So it is the resistance to the rate of shear. When a fluid is stationary, its molecules are in a constant state of motion with a random velocity, say v. On the other hand, when the fluid is in motion, superimposed on this random velocity there is a mean velocity V, which is the mean velocity at of all the fluid. At the interface between the fluid and the solid surface, there exists an interaction between the molecules or atoms of the fluid and those of the solid. The collision rate and surface roughness result in interactions that are strong enough to reduce the bulk velocity of the fluid to zero. This velocity is greater as long as the distance from the surface increases. Viscosity thus plays a role in determining flow patterns. The boundary layer is defined as the thickness of the gradient region from the zero speed to the free-stream velocity.

The boundary layer has thickness of about 1/10th of troposphere. Shearing forces generated by wind flow, the surface friction, and thermal variation creates a buoyancy force that PBL experiences as turbulence. Furthermore, Coriolis force influences the PBL dynamic as well. Internal turbulence is responsible for effective transport of heat, momentum and pollutants. According to literature, the planetary boundary layer can be divided in several layers. The convective boundary layer is the turbulent portion of the atmosphere. It can be divided into three parts, the surface layer, the mixed layer and the entrainment zone. The surface layer is the lowest layer. During the day, this layer is superadiabatic and statically unstable. In the night, because of absence of heating it becomes stable when the surface is cooler than the overlying atmosphere. In this layer, small scale structures can be observed, such as buoyant vertical plumes and even dust devils. The moisture content of this layer is dependent on the recent history. The wind profile shows a logarithmic increase with height, but it is close to zero on the surface. The mixed layer is so called due to the intense mixing in this layer which can be generated mechanically by wind shear or convectively by buoyancy. A uniform mixing results in almost constant values of variables like potential temperature and specific humidity over the vertical extent of the mixed layer. The non-instantaneous nature of the mixing process, the entrainment of warm air from the free troposphere, and heating from the warm

ground contribute to the deviation of these scalars from a constant value. The buoyancy generated turbulence can be described based on the solar radiation balance. The major portion of the solar radiation (50%) is absorbed by the ground, about 30% is reflected by the atmosphere, and the remainder is absorbed by the clouds and other constituents in the atmosphere such as water vapour, ozone, dust, etc. Hot air masses, heated by surface, tend to rise and are replaced by surrounding cooler and denser air. When the air in contact with the surface is heated relative to the cold air overlaying it, the water vapour produced by evaporation at the surface is carried vertically by vigorous convection. As water vapour absorbs radiation, it affects the radiative balance.

The final equilibrium depends on the balance between the radiative and convective effects and is called radiative-convective equilibrium. Convection is controlled by the decreasing rate of temperature with height, the "lapse rate". In fact, convection occurs only when lapse rate exceeds a certain value. An air parcel that moves up adiabatically upward a lower pressure zone becomes less dense and expands its volume. This process involves a temperature decrease, with a lapse rate of -9.8 °C/Km (adiabatic lapse rate). When lapse rate is smaller the warm moving parcel could keep its ascending motion because of its own buoyancy. This unstable condition defines the turbulent motion. Convection will stop when equilibrium condition will be reached. On the other hand, the latent heat can affect turbulent convection. Actually, for an ascending air parcel containing water vapour, latent heat is released with height when air is saturated with water vapour. Above the height of saturation the lapse rate is almost the same of dry adiabatic lapse rate. For the lower troposphere the value of the so cold moist adiabatic lapse rate depends from relative humidity, temperature and pressure: for instance, its value is about 6.5°C/Km at 20°C. The moist and dry adiabatic lapse rates are used to describe upward rising air and descending air, respectively. Afterwards, because of its role in convective motion, water vapour can be used as tracer for the growth/decay of the convective boundary layer.

Because of decay of heat flux at sunset, the turbulence that was previously present in the wellmixed layer begins to decay. Consequently, a layer gets established with the same initial state variables and same concentration of variables as the previous layer. This layer has neutral stability and it is called residual layer, and it has not contact with surface. All moisture incoming from mixed layer are accumulated each night in the residual layer.

During the night a stable nocturnal boundary layer is formed. It is characterized by stable thin layer, almost without turbulence. The main feature of the nocturnal layer is the temperature inversion at its top: in fact during the night Earth's surface get cold due to infra-

red emission, then the ground becomes cooler faster than the air above it, so the temperature increases with height giving rise to an inversion layer at the top of nocturnal boundary layer because the temperature takes again its normal trend.

Chapter 2

OBSERVING PLATFORM CHARACTERISTICS

2.1   Introduction

The Sky Arrow 650 TCNS ERA is a tandem seat aircraft designed and manufactured in Italy by Iniziative Industriali Italiane (Meteor) S.p.A., a company manufacturing gliders, airplanes and Remotely Piloted Vehicles since 1947. The a.m. versions of the Sky Arrow have been designed as sport and recreational aircraft, as well as for training, research and aerial surveillance.

The Sky Arrow TCNS, being almost entirely made of carbon fiber in epoxy resin, feature a strong composite structure and therefore have a very high strength to weight ratio. It is a single engine, high wing, T-tail and fixed tricycle landing gear aircraft.

The Sky Arrow 650 has been type certified in March 1996 in Italy JAR-VLA (Joint Aviation Regulations – Very Light Aircraft) and in October 1997 in the U.S.A. The TCNS versions are in compliance with FAR 23, Amendment 42, requirements, as listed in F.A.A. Advisory Circular AC-23.11 dated December 02, 1992.

The engine is certified to FAR 33 and the propeller to FAR 35. Noise has been tested in accordance with FAR 36, and ICAO.

The Sky Arrow 650TCNS are type certified for day and night VFR in the U.S.A. and those countries that recognize Advisory Circular AC-23.11. They are used for recreation, sport, training and aerial reconnaissance. In the U.K. they are also certified in the Transport Category (passenger).

The craft, due to the tandem configuration, are also usable for military "ab initio" training. For this reason pneumatic gyroscopic instruments, with the relevant engine drive and pump, are part of the standard configuration. Due to the possibility to be used in night operations,

navigation, strobe, landing, cabin and map lights are installed, as well as an additional alternator.

The fuselage is almost entirely made of carbon fiber sandwich in an epoxy resin matrix Kevlar is used in some areas, such as the cabin, where added strength is requested for crash worthiness.

The airfoil is a Gottinga 398 modified for better handling at low speeds. Each wing is attached to the fuselage with 3 bolts (two at the root rib and one at the wing strut) secured by castle nuts and easily removable safety pins. The wing and the control surfaces are made of carbon fiber. The two wing spars are of "C" section. Wing flaps are actuated electrically and can be positioned at 0, 10, 20 and 30 degrees.
The ailerons are actuated via aluminium control rods and bellcranks.

The tricycle landing gear is fixed. The main gear leaf springs are made of fiberglass roving. The nose gear strut is steel and carbon fiber. It features a "donut" type shock absorber and a shimmy damper. The nose gear is free castoring. Steering is provided by a combination of hand-operated differential braking of the main wheels (low speed) and rudder actuation (high speed).

The engine is a Rotax 912 S, certified to FAR 33, with a maximum power of 98 hp at 5.800 rpm. The engine is a horizontally opposed, 4 cylinder, 4- stroke type. It features liquid cooled cylinder heads and air cooled cylinders, dual ignition, dry sump lubrication, dual carburetors and a propeller drive reduction gear box with clutch
The engine features one internal and one external alternator. The engine mount is made of aircraft steel tubing. The propeller is 2 blade, fixed pitch, certified to FAR 35.

Electric power is provided by a twelve volt battery located in the nose of the airplane and is supplied to the electrical system via a bus. An external 40 amp alternator, driven by a belt connected to the propeller shaft, provides power to the battery and the main electrical bus. A second 18 amp internal alternator provides power to the engine ignition system and also serves as a source of emergency power in the event of a malfunction of the primary alternator.

Circuit protection is provided by circuit breakers located on the instrument panel. The instrument panel is prepared to accept various instruments in addition to the standard one (see last page).

CHARACTERISTICS	650 TCNS
Length	7,6 m (24,9 ft)
Height	2,6 m (8,4 ft)
Wing span	9,7 m (31,8 ft)
Wing loading	48,0 kg/m2 (9,8 lbs/sq. ft.)
Power loading	6,6 kg/hp (14,6 lbs/hp)
Seats/arrangement	2/Tandem
Engine type	Rotax 912 S
Engine power (@ 5.800 rpm)	98 hp
Propeller	2-blade, fixed-pitch
Composite structure ultimate load	+8g -4g
Standard empty weight *	400 kg (880 lbs)
Maximum gross weight	650 kg (1.430 lbs)
Useful load	250 kg (550 lbs)
Fuel capacity	68 lt (18 gals)
Fuel consumption (@ 75% power, sea level)	16 lt/h-12 kg/h (4,3 gal/hr)
20 lt/h-15 kg/h	
(5,3 gal/hr)	
Performance **(650 kg / 1430 lbs gross weight)**	
Speed not to be exceeded (VNE)	132 kts (244 km/h)
Maximum speed, sea level	107 kts (198 km/h)
Cruise speed (@ 75 % power, s.l.) 90 kts	97 kts (180km/h)
Stall speed (s.l., full flaps, pwr off)	40 kts (74 km/h)
Take off run	177 m (580 ft)
Take off distance over 50 ft obst.	380 m (1247 ft)
Landing run	135 m (443 ft)
Landing distance over 50 ft obst.	215 m (705 ft)
Rate of climb, sea level	4,3 m/s (850fpm)
Service ceiling (crew limit)	4.100 m (13.500 ft)
Endurance (75 % power, no res.)	3h 25'
Max. range (75 % power, no res.)	610 km (330NM)

Tab. 1.1 three side view od the SkyArrow ERA

Nella seguente tabella vengono sommariamente descritte le caratteristiche dimensionali del velivolo impiegato durante la campagna di raccolta dei dati sperimentali.
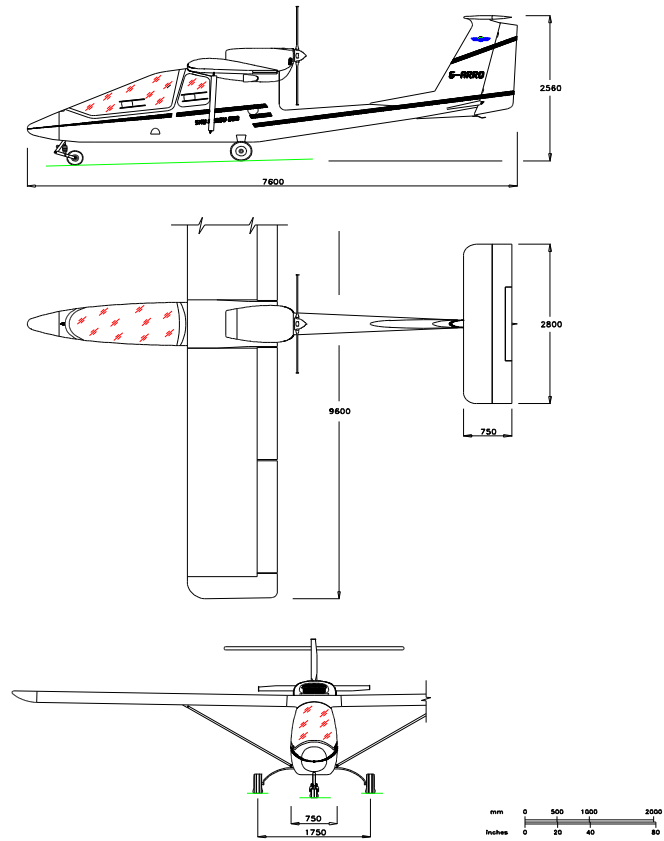
Fig. 2.1 three side view od the SkyArrow ERA

2.2   Mobile Flux Platform (MFP)

   The possibility to use small aircrafts for measuring surface mass and energy fluxes wa
demonstrated in a number of pilot experiments over the past decade. In particular, the
scientists of NOAA have shown that aircraft flux measurements can be very accurate and
reliable and still be executed on small lightweight aircrafts. Critical in the development of this
type of aircraft is its capability to fly at low altitude and low speed, thereby allowing
comparisons between flux estimates from ground sites and from the aircraft, and allowing to
make flux estimates at high spatial resolution.

   The aircraft has been developed to host the Mobile Flux Platform (MFP) which consists of a
set of sensors for atmospheric measurements (figure 2.2).
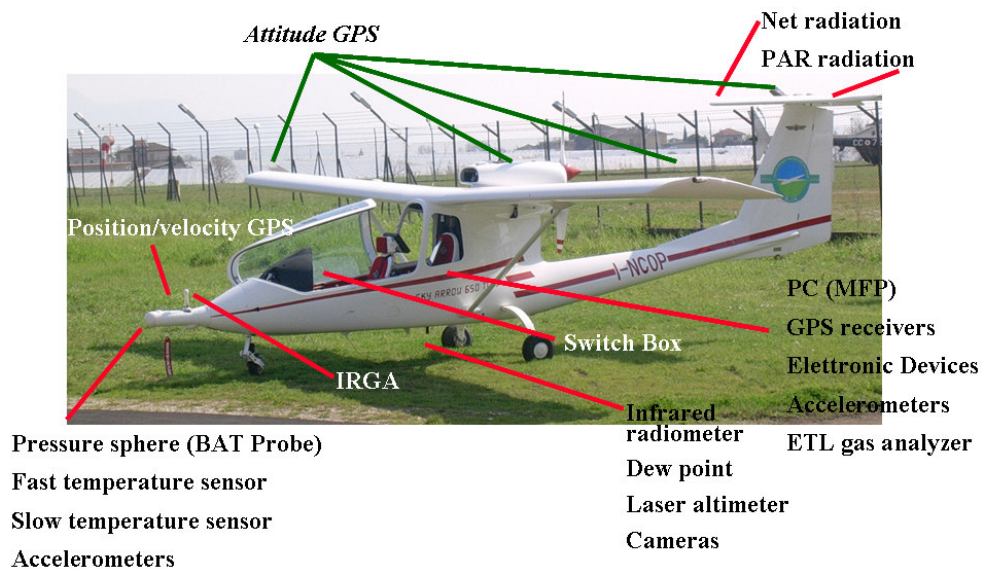
Fig. 2.2 SkyArrow ERA with the exact location of the sensors and instruments mounted
Onboard

The pusher engine configuration is ideal for turbulence measurements, because it allows
instruments to be mounted on the nose of the fuselage where they can project into the
relatively undisturbed air ahead of the aircraft. In addition, the high wing configuration results
in a high vertical separation between the probe and the wing, minimizing flow distortion
effects in the probe region due to air circulation around the wing, the so called 'upwash' effect
(Crawford et al., 1994). With its clean aerodynamics due to the pusher configuration, the
SkyArrow is thus able to perform low-and-slow air-surface-exchange measurements.

2.2.1   MFP Computer:

The MFP computer is purchased from off-the-shelf components to aid in replacement and troubleshooting if any part of the computer should fail in service.   The computer itself consists of a single-board computer and industrial chassis from American Portwell Technologies. Two PCI serial cards from Quatech and a custom ISA card finish the system.

Following the main characteristics:

- CPU - Intel Pentium3 850MHz CPU
- Hard Disk - 40 GB HDD
- IOMEGA 250M ZIP
- RAM - 128MB SDRAM, PC-100

2.2.2   *Auxiliary Box*

The Auxiliary box is custom built at NOAA/ATDD. It contains circuit boards for signal conditioning of the auxiliary REM A/D module, power distribution to the assorted discrete instruments, switching circuits for master power control, a pilot-controlled switch box, a set of orthogonal 3-D accelerometers, and a REM A/D module.

Two analog signal-conditioning boards – These boards are used for analog signal input and conditioning prior to being ingested by the BAT-REM module.

One power distribution board – This board is used to provide 12 VDC power to the MFP computer, the BAT probe assembly, the MFP auxiliary box, and the discrete MFP components.

One switching circuit for master power control – This board and associated pilot-controlled switch box is used to switch power to the MFP computer and the MFP discrete instruments.

Pilot-controlled switchbox – Provides switches for the pilot to control data file write, markers, and events.

Orthogonal 3-D accelerometer board – This board contains a set of 3-D orthogonal accelerometers used to measure the motion of the center of gravity of the aircraft. These are used differentially with the 3-D orthogonal accelerometers in the BAT probe assembly to measure high-frequency pitch, roll, and heading angles.

REM Module – This is a data acquisition module produced by Airborne Research Australia and is capable of digitizing 16 analog channels with 16-bit resolution and providing the data via serial stream to the host MFP computer (reference site [5])

The REM module is a standalone unit designed to perform analog to digital conversion of 16 analog channels, time tag the data, and report the data via serial data stream. A REM serial interface card controls the timing of the data acquisition conversions with a 1 kHz clock and provides incoming serial data to an address port on the computer.

2.2.3   BAT Probe Assembly

The BAT probe assembly is a system of circuit boards and electronic hardware encased in a weatherproof fiberglass/carbon fiber housing that is mounted on the nose of an aircraft. The probe assembly consists of a pressure sphere with 9 holes used to measure the magnitude and direction of the incident wind vector on the hemisphere. A tapered cone afterbody houses a BAT-REM module that is used for digitizing the analog signals and providing a serial data stream to the host MFP computer, much like the BAT-REM module in the auxiliary box. In addition to pressure measurements, a set of three orthogonal accelerometers is also installed in the pressure sphere to measure high frequency motion of the hemisphere in three dimensions. High and low frequency air temperature measurements are made utilizing a PRT probe and a micro-bead thermister. Static pressure measurements from the pressure sphere round out the BAT probe instrument suite.

BAT-REM Module – This is a data acquisition module produced by Airborne Research Australia and is capable of digitizing 16 analog channels with 16-bit resolution and providing the data via serial stream to the host MFP computer (Reference Page, [6] and [7]).

The hard disk is used for primary onboard data storage. The Zip drive with IDE interface is used for secondary data storage.

The pilot's switch box contains an instrument power switch, a computer power switch, a file write switch, an event button, and a marker switch. In addition, two LED's are used to indicate power and system status.

The pilot's display is a color flat panel VGA display (640x480 resolution) that interfaces to a standard ISA VGA card in the computer box. The normal mode of operation of the BATSTORE program is an 80-column by 25-row text screen.

In addition to the minimum equipment components, several additional instruments may be added to the basic system to enhance measurement capabilities. The following are a list of instruments added to the Italian Sky Arrow ERA aircraft (the interface mode for each instrument is listed in parenthesis following the instrument name):

- ATDD/FRD turbulence measurement probe (with internal REM module) (BAT-REM)(serial interface)

- Licor-7500 open-path Infrared Gas Analyzer (IRGA) CO_2/H_2O (analog interface)

- Everest Interscience IR temperature sensor (analog interface)

- Riegl distance measuring laser (serial interface)

- Edgetech dewpoint sensor (analog inteface)

- Novatel OEM-G2 RT20 GPS system (serial interface)

- Javad AT-4 GPS attitude system (serial interface)

- StarPanel Technologies flat panel monitor M3300E (pilot)

- LCD touch screen monitor (mfp operator)

- REBS Q*7 net radiometer (analog interface)

- Licor Quantum (PAR up/PAR down) (analog inteface)

2.2.4   Discrete MFP Components

The following components are installed in the aircraft in addition to the core MFP components discussed above. Each is interfaced either through the analog A/D BAT-REM module in the auxiliary box, or directly to the Quatech ESC-100-D9 eight-port serial card in the MFP computer.

- *Edgetech dew point sensor*

This chilled-mirror is used to directly measure the dew point temperature of the air adjacent to the aircraft. It contains a mirror and temperature control assembly that is mounted just below the aircraft in the downward-looking instrument bay directly behind the pilot in the Sky Arrow 650 ERA. Data is acquired via analog output that is digitized by the BAT-REM module mounted in the MFP auxiliary box.

(Reference Page:[8])

- *Everest Interscience InfraRed temperature sensor*

This instrument is mounted so as to point straight down toward the Earth while the aircraft's wings are level. It provides a high-frequency measure of the temperature of the surface directly below the aircraft. The instrument is mounted just below the aircraft in the downward-looking instrument bay directly behind the pilot in the Sky Arrow 650 ERA. Data is acquired via analog output that is digitized by the BAT-REM module mounted in the MFP auxiliary box.

(Reference Page: [9])

- *Javad AT4 GPS attitude system*

This system is used to measure the pitch, roll, and heading angle of the aircraft with respect to Earth at 20 Hz. The system utilizes four antennas to make its attitude measurement. The first antenna is mounted on the top of the BAT probe assembly. The second is mounted on top of the vertical fin and horizontal stabilizer. The third is mounted on top of the left wing near the wing/strut junction, and the fourth is mounted on top of the right wing near the wing/strut junction. Data is acquired through one of the eight serial ports on the Quatech ESC-100-D9 eight-port serial card in the MFP computer.

(Reference Page:[10])

- *Li-Cor 7500 open-path Infrared Gas Analyzer (IRGA)*

  This instrument is used to measure concentrations of CO_2 and H_2O in the atmosphere with high frequency, and reduced absolute precision. Frequency response is 20 Hz, and the instrument is mounted so that its sample volume is exposed to the free-stream flow, approximately 40 centimeters behind the pressure sphere. Data is acquired via analog output that is digitized by the BAT-REM module mounted in the MFP auxiliary box.

  (Reference Page: [11])

- *REBS Q*7 net radiometer*

  This system is used to measure the difference between incoming and reflected solar radiation. The instrument is mounted on the left side of the aircraft's horizontal stabilizer, along with the Li-Cor PAR sensors. Data is acquired via analog output that is digitized by the BAT-REM module mounted in the MFP auxiliary box.

- *NovAtel OEM-G2 RT-20 GPS system*

  This system is used to measure the position and velocity of the aircraft using differential corrections at 10 Hz, and time reference for the MFP system. Time data is obtained from an onboard clock that is synchronized with GPS time, obtained from the GPS satellites. The antenna for this system is mounted on the top of the BAT probe assembly. Data is acquired through one of the eight serial ports on the Quatech ESC-100-D9 eight-port serial card in the MFP computer.

  (Reference Page: [12])

- *Riegl laser*

  This is a laser range finder that is mounted so that is looks downward from the bottom of the aircraft. The laser reports distance at programmable time intervals (up to 100 Hz) via an RS-232 serial port. Data is acquired through one of the eight serial ports on the Quatech ESC-100-D9 eight-port serial card in the MFP computer. (Reference Page: [13])

- StarPanel Technologies flat panel monitor M3300E

This flat panel monitor is used to provide the pilot with a visual display of the data output from the MFP system. It is powered by a 12 VDC source from the MFP auxiliary box. (Reference Page: [14]).

2.2.5 Aligning the data in time

Data from each serial device is aligned in time using GPS time tags, when possible. The NovAtel GPS provides the master clock and programmable frequency timing signal generator that is used to provide timing synchronization for the entire MFP system. A 1 Hz time-tag message is output on the NovAtel GPS serial port and used to mark the beginning of each second for purposes of separating data from other instruments into 1-second time intervals.

When time tags are not available from a particular device (e.g. the BAT-REM modules), the devices are individually triggered using TTL level signals derived from a programmable oscillator on the NovAtel GPS. The fundamental frequency of the oscillator is 500 Hz. The 500 Hz TTL signal is then passed through a divide-by-10 circuit on the ISA card in the MFP computer. The resulting 50 Hz signal is then used to trigger the start of a 20 ms measurement period for each BAT-REM module. This ensures each BAT-REM module is synchronized to the GPS clock. The software then stores successive data points as they are received on the serial port in the placeholder for the current second until the new 1 Hz time-tag message is received from the NovAtel GPS, at which point the next BAT-REM messages are stored in the placeholder for the new current second.

In the case of devices with free-running clocks, such as the Riegl laser, the clock on the laser is programmed to "free-run" at whatever output frequency is desired. Data points are then collected and stored sequentially in the placeholders for the current second until the new 1 Hz time-tag message is received from the NovAtel GPS, at which point the next messages are stored in the placeholder for the new current second.

A note about the ATDD/FRD turbulence measurement probe: This is an assembly that consists of a hemispherical dome with pressure measurement ports and a tapered cone onto which the hemisphere mounts. Mounted on the front of the aircraft, the BAT probe measures

the magnitude and direction of the wind vector incident on the hemisphere. Using GPS to measure the magnitude and direction of the velocity vector of the aircraft with respect to Earth, the wind velocity with respect to Earth can be computed.

PART I: REMOTE SENSING

DESIGN AND REALIZATION OF THE REMOTE SENSING SYSTEM (*ERACAM*)

3.1   Introduction

This chapter will describe the 'process' followed to 'design' and 'realize' the data acquisition system for remote sensed images installed onboard the SkyArrow aircrafts operated by CNR ISAFoM.

This work, inserted in this research project of the ISAFoM institute, has as target, the realization of a complete and versatile airborne platform, which can give the possibility to apply different methodologies at the same acquisition mission. In fact, as the platform is delivered from the maker, the mission is realizable with the system present on board the aircraft (MFP), only if related to the "*Fluxes Measurement Mission*". With this upgrade, the platform will be able to collect both thermal and composite remote sensed images and at the same time fluxes data.

This gives the possibility to collect much more information with relation to the interaction between the atmosphere and soil, by use of the remote sensed images to evaluate several vegetation index (i.e. NDVI, VI etc..), thermal inertia, albedo, very high resolute evapo-transpiration maps and so on.

At present, other users that utilize airborne platforms, to collect atmospheric and soil parameters, have to use different platforms to collect the same information pocket. After the upgrade however, the SkyArrow can do this same job without requiring a second platform.

Generally, when more aircraft are available, the planning is to use the fluxes measurement aircraft at lowest altitude, and the remote sensing aircraft at the highest altitude; with this

methodology it is possible to have the information related at the level of flight at the same time, but, obviously it is more expensive.

Since the flight parameters for the two missions are different (i.e different altitudes), doing this job with one platform with both the systems onboard, can be used in missions where the monitored area is not too large, so the delay between the fluxes measurement and the remote sensing measurement is diminished, and the information collected are utilizable as if they are collected instantaneously.

Generally, for a mission where the remote sensed images are used to upscale the fluxes measured on a bigger area (by use of thermal and NDVI mapping), the delay between the two kind of measurements give the possibility to use one platform instead of two platforms.

Often, the fluxes measurements are made at different altitudes to evaluate the "*flux divergence*", to predict the real flux at soil level; in this kind of mission the use of remote sensing at the highest altitude, allows the operator to optimize the mission collecting also the remote sensed images.

3.2   General considerations on remote sensing

Remote sensing means measuring an object at a distance without physical contact with it. Eyesight is a form of remote sensing. When the eye sees an object, the electromagnetic radiation (reflected light) from the surface of the object is registered. The radiation contains information about the surface and we see colour and form. A scanner in a satellite also records electromagnetic radiation.

A white surface reflects equal amounts of radiation of all wavelengths of visible light, whereas a green leaf reflects less radiation in the red and blue parts of the visible spectrum than in the green.

This gives an excess of green light (compared to red and blue) and the leaf looks green. So the composition of the electromagnetic reflection, the spectral signature, tells us about the surface emitting or reflecting the radiation.

The ability of airborne systems to distinguish between various spectral signatures is critical for their use in mapping, where the distinction between different surface and area types is essential.

The human eye can only perceive radiation within a limited range of the electromagnetic spectrum. So instruments for remote sensing outside the visible wavelengths actually represent an extension of our visual field and they give access to additional information about the physical world surrounding us.

Electromagnetic radiation from a surface is either a reflection (reflected light) or an emission (radiation emitted from the surface itself). Reflected sunlight is for obvious reasons only measurable in daylight, whereas emission can be measured at all times.

Thermodynamics indicates that a body at temperature different from 0 Kelvin, i.e. an object on Earth, emits radiation proportionally to its temperature.

Surface temperature is a key factor for emission. The sun has a surface temperature of 6000 degrees Kelvin (K) and maximum emission in the visible light range. A surface with a temperature of about 1000K, e.g. a fire in the forest, has its maximum emission in the middle infrared spectrum. The surface temperature of the Earth is about 290K and a emission maximum around 14 micrometers, also called the thermal infrared range. There is a direct correlation between surface temperature and degree of emission at a given wavelength. The surface temperature can be calculated on the basis of remote sensing of the thermal infrared emission.

Surfaces with different temperatures have maximum emission at different wavelengths.

The maximum emission of the sun is in the wavelength 0.483 micrometres, whereas that of the Earth is at 14 micrometres.

Emission from a surface is a function of its surface temperature, which means that surface temperature can be calculated on the basis of remote sensing of surface emission.

As the Earth only radiate small amounts of energy in visible light, it can only be seen because it reflects visible light from the sun. Sun-rays hitting the Earth can either be absorbed and thus contribute to the heating of the Earth or be reflected and seen by the human eye or sensed by a camera. The albedo value of a surface indicates how large a percentage of the sunlight is reflected.

The reflection from bare ground increases slightly from the visible to the infrared range of the spectrum. There are great differences between different types of soil, dry and humid land. Different mineral compositions of the surface are also reflected in the spectral signature.

Generally, water only reflects in the visible light range. As water has almost no reflection in the near infrared range it is very distinct from other surfaces. Thus water surfaces will be clearly delimited as dark areas (low pixel values) in images recorded in the near infrared range.

The spectral signature for green plants is very characteristic. The chlorophyll in a growing plant absorbs visible and especially red light to be used in photosynthesis, whereas near infrared light is reflected very effectively as it is of no use to the plant.

In this way the plants avoid unnecessary heating and loss of juice through evaporation. Therefore the reflection from vegetation in the near infrared and in the visual ranges of the spectrum varies considerably. The degree of difference reveals how large a part of the area is covered with growing green leaves (leaf area index).

3.2.1   Passive optical sensors

Cameras and their use for aerial photography are the simplest and oldest of sensors used for remote sensing of the Earth's surface. Cameras are framing systems which acquire a near-instantaneous "snapshot" of an area, of the surface. Camera systems are passive optical sensors that use a lens (or system of lenses collectively referred to as the optics) to form an image at the focal plane, the plane at which an image is sharply defined.
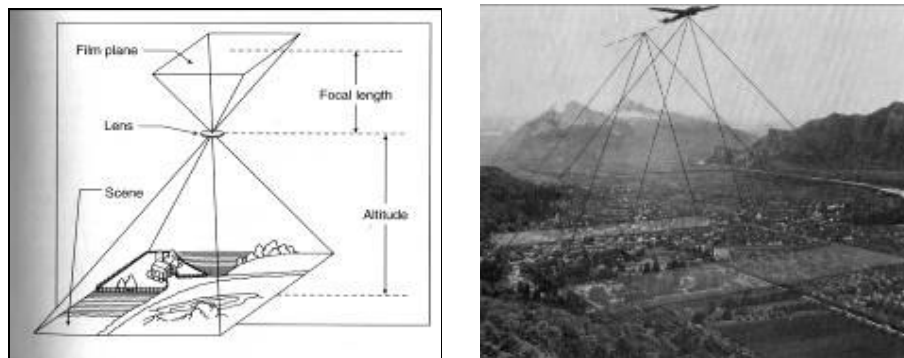

Fig 3.1: geometric rappresentation of passive optical sensor

Photographic films are sensitive to light from 0.3 μm to 0.9 μm in wavelength covering the ultraviolet (UV), visible, and near-infrared (NIR). Panchromatic films are sensitive to the UV and the visible portions of the spectrum. Panchromatic film produces black and white images and is the most common type of film used for aerial photography. UV photography also uses panchromatic film, but a filter is used with the camera to absorb and block the visible energy from reaching the film. As a result, only the UV reflectance from targets is recorded. UV photography is not widely used, because of the atmospheric scattering and absorption that occurs in this region of the spectrum. Black and white infrared photography uses film sensitive to the entire 0.3 to 0.9 μm wavelength range and is useful for detecting differences in vegetation cover, due to its sensitivity to IR reflectance.

Fig 3.2: Normal and False colour rappresentation

Colour and false colour (or colour infrared, CIR) photography involves the use of a three layer film with each layer sensitive to different ranges of light. For a "*normal colour photograph*", the layers are sensitive to blue, green, and red light - the same as our eyes. These photos appear to us the same way that our eyes see the environment, as the colours resemble those which would appear to us as "normal" (i.e. trees appear green, etc.). In colour infrared (CIR) photography, the three emulsion layers are sensitive to green, red, and the photographic portion of near-infrared radiation, which are processed to appear as blue, green, and red, respectively. In a "*false colour photograph*", targets with high near-infrared reflectance appear red, those with a high red reflectance appear green, and those with a high green reflectance appear blue, thus giving us a "false" presentation of the targets relative to the colour we normally perceive them to be.

Cameras can be used on a variety of platforms including ground-based stages, helicopters, aircraft, and spacecraft. Very detailed photographs taken from aircraft are useful for many applications where identification of detail or small targets is required. The ground coverage of a photo depends on several factors, including the focal length of the lens, the platform altitude, and the format and size of the film. The focal length effectively controls the "*angular field of view*" of the lens (similar to the concept of instantaneous field of view) and determines the area "seen" by the camera. The longer the focal length, the smaller the area covered on the ground, but with greater detail (i.e. larger scale). The area covered also depends on the altitude of the platform. At high altitudes, a camera will "see" a larger area on the ground than at lower altitudes, but with reduced detail (i.e. smaller scale). Aerial photos can provide fine

detail down to spatial resolutions of less than 50 cm. A photo's exact spatial resolution varies as a complex function of many factors which vary with each acquisition of data.

Most aerial photographs are classified as either "*oblique*" or "*vertical*", depending on the orientation of the camera relative to the ground during acquisition. "*Oblique aerial photographs*" are taken with the camera pointed to the side of the aircraft. High oblique photographs usually include the horizon while low oblique photographs do not. Oblique photographs can be useful for covering very large areas in a single image and for depicting terrain relief and scale. However, they are not widely used for mapping as distortions in scale from the foreground to the background preclude easy measurements of distance, area, and elevation.

"*Vertical photographs*" taken with a single-lens frame camera is the most common use of aerial photography for remote sensing and mapping purposes. These cameras are specifically built for capturing a rapid sequence of photographs while limiting geometric distortion. They are often linked with navigation systems onboard the aircraft platform, to allow for accurate geographic coordinates to be instantly assigned to each photograph. Most camera systems also include mechanisms which compensate for the effect of the aircraft motion relative to the ground, in order to limit distortion as much as possible.

When obtaining vertical aerial photographs, the aircraft normally flies in a series of lines, each called a "*flight line*". Photos are taken in rapid succession looking straight down at the ground, often with a 50-60 percent overlap between successive photos. The overlap ensures total coverage along a flight line and also facilitates "*stereoscopic viewing*". Successive photo pairs display the overlap region from different perspectives and can be viewed through a device called a "*stereoscope*" to see a three-dimensional view of the area, called a "*stereo model*". Many applications of aerial photography use stereoscopic coverage and stereo viewing.

Aerial photographs are most useful when fine spatial detail is more critical than spectral information, as their spectral resolution is generally coarse when compared to data captured with electronic sensing devices. The geometry of vertical photographs is well understood and it is possible to make very accurate measurements from them, for a variety of different applications (geology, forestry, mapping, etc.). The science of making measurements from photographs is called "*photogrammetry*" and has been performed extensively since the very

beginnings of aerial photography. Photos are most often interpreted manually by a human analyst (often viewed stereoscopically).

"Multiband photography" uses multi-lens systems with different film-filter combinations to acquire photos simultaneously in a number of different spectral ranges. The advantage of these types of cameras is their ability to record reflected energy separately in discrete wavelength ranges, thus providing potentially better separation and identification of various features. However, simultaneous analysis of these multiple photographs can be problematic. "*Digital cameras*", which record electromagnetic radiation electronically, differ significantly from their counterparts which use film. Instead of using film, digital cameras use a gridded array of silicon coated CCDs (charge-coupled devices) that individually respond to electromagnetic radiation. Energy reaching the surface of the CCDs causes the generation of an electronic charge which is proportional in magnitude to the "brightness" of the ground area. A digital number for each spectral band is assigned to each pixel based on the magnitude of the electronic charge. The digital format of the output image is amenable to digital analysis and archiving in a computer environment, as well as output as a hardcopy product similar to regular photos. Digital cameras also provide quicker turn-around for acquisition and retrieval of data and allow greater control of the spectral resolution. Although parameters vary, digital imaging systems are capable of collecting data with a spatial resolution of 0.3m, and with a spectral resolution of 0.012 mm to 0.3 mm. The size of the pixel arrays varies between systems, but typically ranges between 512 x 512 to 2048 x 2048.

For some remote sensing instruments, the distance between the target being imaged and the platform, plays a large role in determining the detail of information obtained and the total area imaged by the sensor. Sensors onboard platforms far away from their targets, typically view a larger area, but cannot provide great detail. Compare what an astronaut onboard the space shuttle sees of the Earth to what you can see from an airplane. The astronaut might see your whole province or country in one glance, but couldn't distinguish individual houses. Flying over a city or town, you would be able to see individual buildings and cars, but you would be viewing a much smaller area than the astronaut. There is a similar difference between satellite images and airphotos.

The detail discernible in an image is dependent on the "*spatial resolution*" of the sensor and refers to the size of the smallest possible feature that can be detected. Spatial resolution of passive sensors depends primarily on their "*Instantaneous Field of View (IFOV)*". The IFOV

is the angular cone of visibility of the sensor and determines the area on the Earth's surface which is "seen" from a given altitude at one particular moment in time. The size of the area viewed is determined by multiplying the IFOV by the distance from the ground to the sensor. This area on the ground is called the "*resolution cell*" and determines a sensor's maximum spatial resolution. For a homogeneous feature to be detected, its size generally has to be equal to or larger than the resolution cell. If the feature is smaller than this, it may not be detectable as the average brightness of all features in that resolution cell will be recorded. However, smaller features may sometimes be detectable if their reflectance dominates within a particular resolution cell allowing sub-pixel or resolution cell detection.

3.3   System process design

The cameras chosen for the airborne remote sensing system ERACam are:

- 2 Duncantech MS4100 (RGB/CIR)
- FLIR A40M

DuncanTech's MS4100 high-resolution, progressive-scan digital camera for remote sensing, aerial photogrammetry, and high-end color imaging acquires data with a resolution of 1,920 x 1,080 pixels at a rate of 10 frames per second. The RGB camera employs a color-separating prism and three charge-coupled device (CCD) sensors to support red-green-blue. The multispectral "CIR" cameras capture 3 bands of imagery Green, Red, and NIR. Multispectral Images are saved in TIFF image file format with 3 bands per image. In the table below are showed the specifications of the spectral responses of the two multispectral cameras.

Fig 3.1: Duncantech MS4100

Band	CIR Configuration (nm)			RGB Configuration (nm)		
	Range	Center	Width	Range	Center	Width
Blue	-	-	-	438-482	460	45
Green	512-599	555	87	512-560	540	40
Red	618-707	662	89	640-680	660	40
NIR	763-850	806	87	-	-	-

Tab 3.1: Duncantech CIR/RGB spectral specifications

| Duncantech MS4100	
Image Device	1-Inch Interline Transfer CCD
Picture Elements	1920(H) x 1080(V)
Pixel Size	7.4 x 7.4 micron
Pixel clock rate	25 MHz
Sensing Area	14.2 x 8 mm
Image output	Digital Image OutputCameraLink, EIA-644 (LVDS) or RS-422: 8 bits x 4 taps or 10 bits x 3 taps
Frame Rate	10 frames per second
Signal/Noise	60 dB
Lens Mount	Nikon Bayonet Mount
Electronic Shutter:	Range: 1/10,000 -1/10 sec. Controlled via RS232
Gain Selection	Range: 0-36 dB. Controlled via RS
External Trigger	Input Edge or level, three modes
External Trigger Source	BNC or Frame Grabber (Optical isolator on BNC)
Exposure Control	Manual or Automatic
White Balance	Manual or Semi
Noise Reduction	Correlated Double Sampling
Usability Features	Digital cross hairs, Color
Operating Temperature	0-50 C
Operating Voltage	12 VDC
Power Consumption	15 Watts
Weight:	1.8 kg
Programmable Functions	Gain, exposure time, multiplexing, trigger, modes, custom processing

Tab: MS4100 specifications
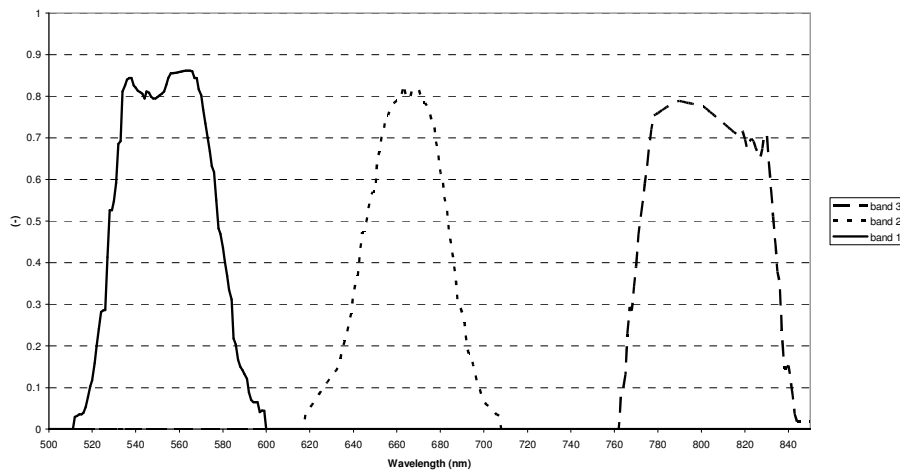
Fig 3.1: CIR spectral response curves

The FLIR A40M thermal infrared cameras are FLIR long wave, handheld, Focal Plane Array cameras that are capable of temperature measurement. This camera are best suited for Preventive Maintenance, Research and Development, and Medical Applications. These Cameras store images on a PCMCIA Card, and the images can be analyzed using one of several available FLIR software packages. The Camera can store images digitally and download those images via Fire Wire.

Fig 3.1: FLIR A40M

FLIR A40M	
Field of view/min focus distance	24° X 18°/0.3m
Spatial resolution (IFOV)	1.3 mrad
Frame rate	50 Hz/60 Hz
Focus	Automatic or Manual
Detector Type	Uncooled microbolometer
Array format	320 x 240
Spectral response	7.5 -13 microns
Image output	RS170 EIA/NTSC or CCIR//PAL IEEE-1394 Firewire or RJ-45 Ethernet options
Accuracy	+/- 2 ^{o}C, +/- 2% of reading
Temperature range	-40 ^{o}C to +120 ^{o}C; 0 ^{o}C to +500 ^{o}C Up to +2000 ^{o}C (optional)
M**easurement mode**	Spot/manual (up to 6 movable), Area (up to 4 movable),Isotherms and Delta T
Emissivity correction	Variable from 0.1 to 1.0
Measurement corrections	Reflected ambient, distance, relative humidity, external optics
Image storage Type	Built-in flash memory 50Hz / 60Hz full frame recording in PC (Firewire version)
File format - Thermal	JPEG with 16 bit measurement data
Field of view/min. focus distance	7° x 5.3^o/4m; 12° x 9°/1.2m; 45° x 34°/0.1m; 80° x 60°/0.1m
External power	110/220VAC, 50/60Hz power adapter or 12/24V DC
Humidity	10% to 95% non-condensing
Operating temperature range	-15 ^{o}C to 50 ^{o}C
Storage temperature range	-40 ^{o}C to +70 ^{o}C
Encapsulation	IP 40
Operational Vibration/Shock	2G, IEC 68-2-6/25G IEC-68-2-29
Weight	1.4 Kg
Size	207 mm x 92 mm 109 mm
Tripod mounting	1/4" – 20
PC interface	IEEE 1394 or RJ-45 Ethernet, RS-232
Digital input (TTL)	Shutter disable, store image, batch enable
Digital output (TTL)	Spot/area threshold alarm, internal temperature sensor alarm, V-sync
Analog input	External temperature sensor, 0 - 5 V
Analog output	Spot/area temperature 0 - 5 V, internal temperature sensor 0 - 5 V

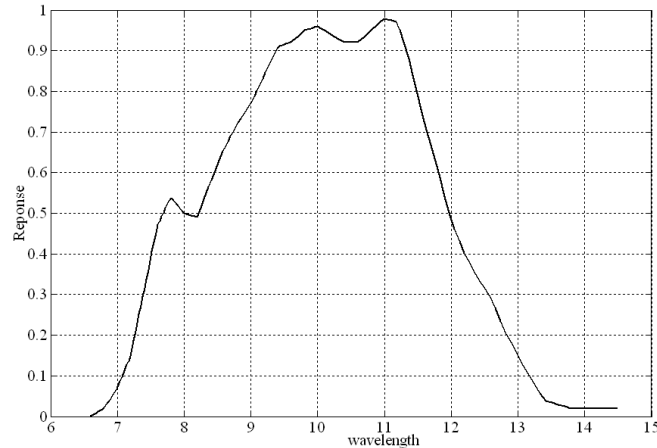*Tab: FLIR A40M specifications*

Fig 3.1: FLIR A40M spcectral response curve

In this section we explain how the system design was carried out, and which "System Engineering Process" was followed to design properly the system. Systems engineering should be thought of as a problem-solving discipline with its own set of tools and processes. It is a relatively young discipline and is still evolving. The tools, processes, and even the terminology are still not fully developed in comparison with the traditional engineering disciplines. There are two common ways to view system engineering activities. One way is to start with the customer's point of view and look at successive levels of detail. The second view is to look at the various activities that must be accomplished as the systems engineering project moves along in time.

The NASA Systems Engineering Handbook ( ) was written to apply to the development of large NASA projects by providing broad descriptions of processes, tools, and techniques.

According to the NASA systems engineering approach, a system is designed, built, and operated so that it accomplishes its objective in the most cost-effective way, considering performance, cost, schedule, and risk. Since cost is a fundamental constraint, the cost-effective focus is a key consideration in this process.

The System Engineering Process used by NASA is outlined in these following 7 steps:

1. Recognize Need/Opportunity
2. Identify and Quantify Goals
3. Create Alternative Design Concepts

4. Do Trade Studies

5. Select Concept

6. Increase the Resolution of the Design

7. Perform the Mission

Martin's approach can be accepted as a guide for systems engineering. In this SEP, he asks questions to check the steps if properly organized. In this SEP, there are 8 steps:

1. Need

2. Operations Concepts

3. Functional Requirements

4. System Architecture

5. Allocated Requirements

6. Detailed Design

7. Implementation

8. Test

For the design of the ERACam system we have developed an our SEP that better matches our process. We can accomplish at the points before as:

1. The target

2. Operations Concepts

3. Functional Requirements

4. System Architecture

6. Detailed Design

7. Implementation

8. Flight test and operative campaigns

3.3.1 The target

What we need is an airborne remote sensing system that must be capable to produce thermal and multispectral mapping of the area observed at the same time of fluxes measurements, and must be capable also to provide us with the following image's information:
- time of the acquisition
- position of the centre of the image
- attitude of the cameras at moment of the acquisition

3.3.2 Operations Concepts

The system will be carried onboard a two-seat light aircraft, SkyArrow 650TCNS, where the payload allowed and electrical power available are limited.

The system must be capable to store images at different frame rate to ensure the coverage of the area observed, from high frame rate at low altitude, to low frame rate at high altitude. Since the platform is a light aircraft with 650 Kg of maximum take off weight, is preferable that during the operative mission the whole crew of the aircraft is composed by the pilot, both for endurance and manoeuvrability and safety of the aircraft. This implies that the system must be capable to operate in automatic mode, or almost in semi-automatic, giving at the pilot the task of managing elementary push-button (to switch on and off) and of surveying status indicator of the system during the normal conduct of the aircraft. The presence of the operator is allowed during flight test and during short and complex missions. The endurance of the aircraft is of about three hours, then the system must be capable to store at least three hours of image acquisition.

Then the summary of the operations concepts are in the following table:

OPERATIVE CONCEPTS
Low power consumption
Low weight and dimensions
Resistance to shock and vibration
Automatic or semi-automatic mode
3h of flight storage

Tab 3.1: Operative Concepts

3.3.3   Functional requirements

To design the remote sensing system that must manage several cameras, it is necessary to introduce a set of "*Functional requirements*" on which we base our considerations for the dimensioning.

The most important parameter is the "*maximum frame rate*" that the system has to ensure during an acquisition, that is, the maximum number of images collected for each second. From it we can calculate the "*maximum data rate*" that will go through the bus of the system. This parameter leads to the dimensioning of the system. The data rate is directly related to frame rate, frame sizes and the number of bits that are used to decoding the information for each pixel :

$$data\_rate = a * b * n * fps \qquad (3.1)$$
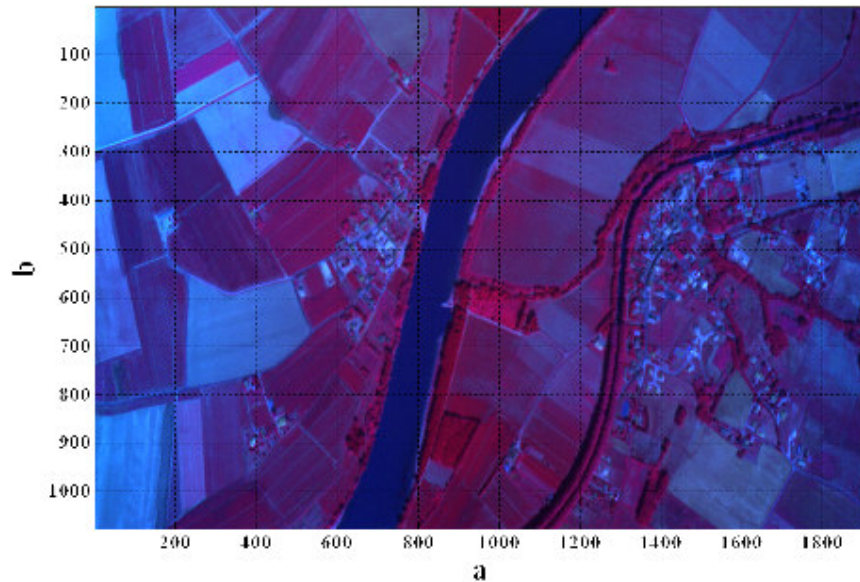
Fig 3.3: Multispectral image with a-columns and b-rows

Where "*a*b*" is the number of pixels of the image, "*n*" is the number of bits for each pixel, and "*fps*" are the frames per second to acquire.

The first step is to calculate the maximum frame rate, and to do it we have to consider the worst case between the several possible configurations that arises on basic considerations on geometry of vertical photograph .

Following considerations on the geometry of vertical photograph.

In photogrammetric terms there are nine orientation elements of a near-vertical photograph: six "*outer-orientation*" elements and three "*inner orientation*" elements:

Outer orientations:

3 translations: X,Y,Z

3 rotations : tip (Φ) phi, tilt (ω) omega, swing (k) kappa.

The aviation counterparts of the above rotational elements are :

Pitch (tip)

Roll (tilt)

Yaw (swing)

Inner orientation:

Principal Distance (PD); (calibrated focal length *f*).

Principal Point (PP); (position of PP: 2 shifts, x and y)

The inner orientation elements refer to the survey camera and, as a consequence, are known to a high degree of accuracy. In this contest the nominal focal length of the camera is good enough, but is not sufficiently accurate for metric work.

Another important parameter is the desired "*Scale (M)*" (or the "*Scale number (m)*") of a vertical photograph. This leads also at total frame rate, hence at the data rate of the system, and then is strictly correlated with electronic design of the system.

The scale is defined as:

$$M = f/H \qquad\qquad (3.2)$$

where f is the focal length and H is the mean high above ground level. In our calculation for survey flight planning we use the reciprocal of scale:

$$m = H/f \qquad\qquad (3.3)$$

Equation 3.3 serves as well for the rare conditions where the terrain is flat, but does not take into account either topographic relief or camera tip and tilt. Flying height can usually be controlled to within 1%, but there will always be small variation in scale from one image to another along a given flight line, particularly in condition of strong turbulence. Topographic relief or camera tilt and tip will also cause variation in scale from point to point within each photograph.

Apart from the occasional single pin-point photograph, most vertical are taken as a series of overlapping flight strips. The general accepted degree of forward overlap is 60% ± 5%, which provides for a number of conditions:

1. Good stereoscopic cover between successive frames.
2. Full coverage in the event of damage of any frame.
3. Adequate provision against scattered cloud obscuring the mission area (usually sufficient to allow to up for one or two octa of flight cumulus).
4. Reasonable safety against undue terrain variation, or camera tilt due to turbulence, drift, etc.

The base of a pair of forward-overlapping vertical images (also known as the *air base*) is the movement of the camera between two air stations along a given flight line, as is shown in figure 3.4.

The images collected with the system described in this chapter are defined as "*Vertical aerial photographs*". They are acquired along the "*flight line*". The line that joins the images centre along the flight line is called "*nadir line*".

To ensure the total coverage of the region flew by the aircraft is common to set an "*overlap*" between consecutive images. This is done to avoid the possibility that delay during the acquisition leads to a portion of the observed area lost.
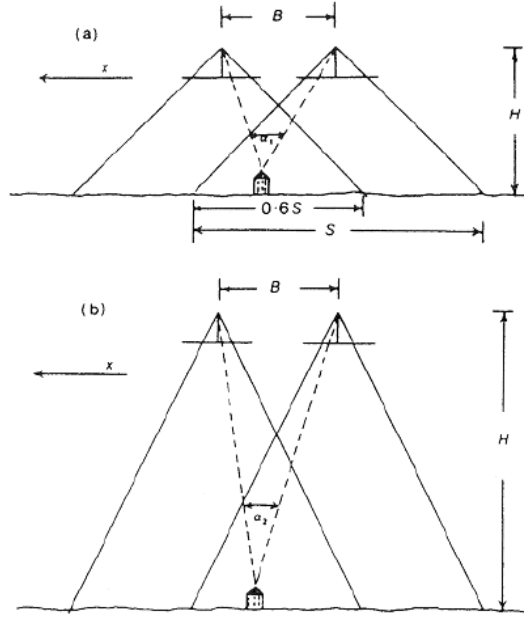
Fig 3.4: the air base "B" of an overlapping pair of photographs is provided by two camera station along the flight line. The 60% overlap provides for stereoscopic observation.

The calculation of the optimum "*frame rate*" to ensure the requested overlap is explained by the following parameters:

The swath along track S is given by:

$$S = 2 * H * \tan\left(\frac{\vartheta}{2}\right)[m] \qquad (3.4)$$

The "frame timing" (time between two captured images) is given by:

$$t = \frac{(1 - overlap) * S}{v}\left[\frac{\sec}{frame}\right] \qquad (3.5)$$

Where S is the dimension of the swath along-track and v is the aircraft ground velocity, hence the frame rate is given by:

$$fps = \frac{1}{t}\left[\frac{frame}{\sec}\right] \qquad (3.6)$$

To calculate the data rate expressed in Kb/s (or MByte s-1), we have to make a trade-off between the scale, the resolution cell and the swath of the image. The figure 3.5 shows that the multispectral camera has a better resolution, while the figures 3.6 and 3.7 show that the two cameras have different across-track field of view but almost the same along-track field of view.
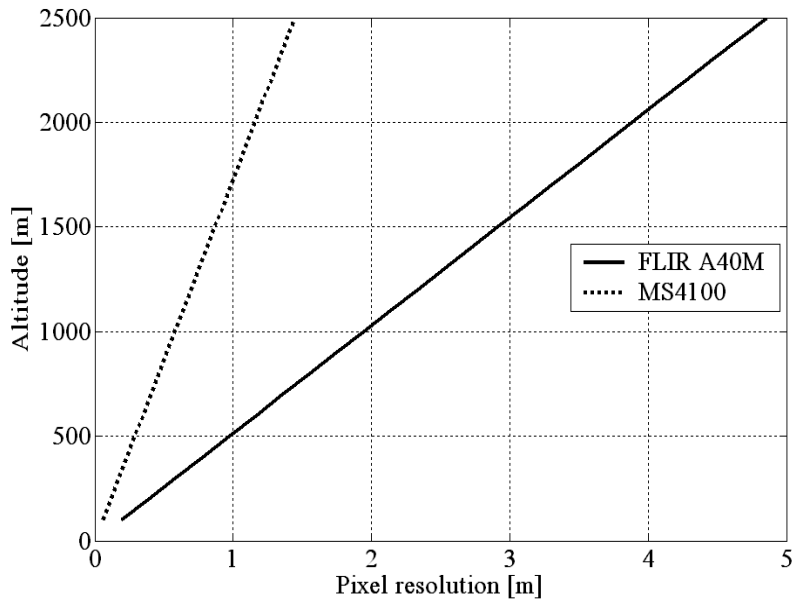

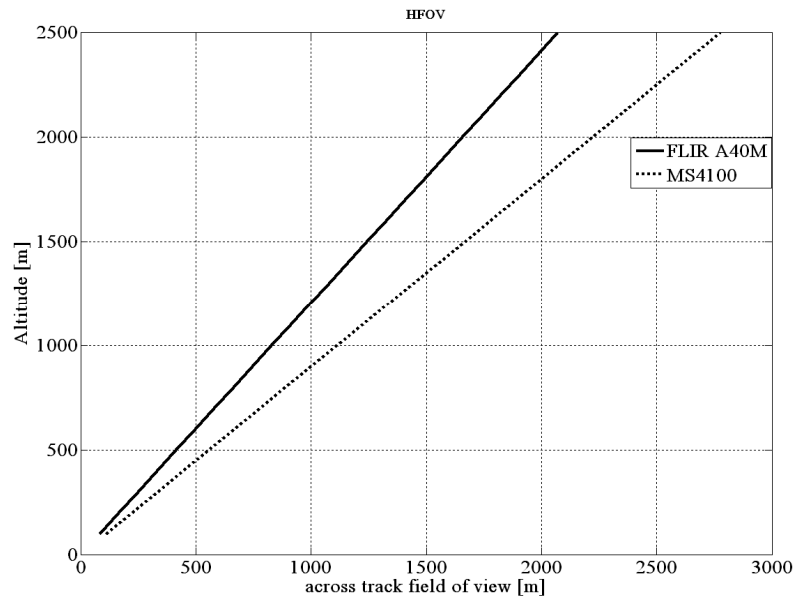*Fig 3.5: The variation of the pixel resolution for both the thermal (FLIR A40M) and multispectral camera (MS4100).*

Fig 3.7: The variation of the along track field of view for both the thermal (FLIR A40M) and multispectral camera (MS4100) respect with the high abovethe ground level.
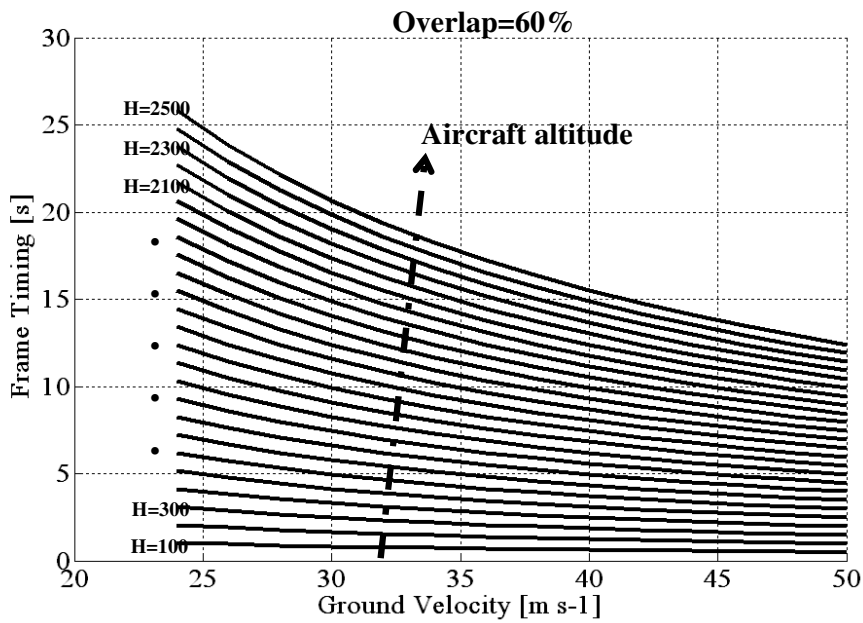

Fig 3.8: The variation of the frame timing of the MS4100 with the aircraft ground velocity and the high above ground level to held an overlap of 60%.

Given an aircraft ground velocity and the mean high above ground level, we can calculate the frame timing of the acquisition from the equations 3.1 to 3.6. As is showed from the figure 3.8, the frame timing growths with the high and decreases with the aircraft ground velocity.

In the table 3.2 are reported the image specifications for two possible high and for a given aircraft ground velocity of 40 m s-1 (the cruise speed of the SkyArrow aircraft):

	H=165M		H=2500M	
	MS4100	A40M	MS4100	A40M
HFOV [m]	183.3	136.61	2777.3	2069.9
VFOV [m]	102.31	102.51	1550.2	1553.16
Resolution [m]	0.095	0.427	1.447	6.468
Frame timing [s]	1	1	16	16
Data rate [Kb s-1]	~ 49766	~1075	~ 3110	~ 67

Tab 3.2: image specifications for two opposite cases

The worst case, that leads the design of the system, is obviously that one at lower high, that correspond at frame timing of one second for what the data rate is of about 51000 Kb s^{-1} (~ 6.3 MB s^{-1}).

The PCI bus is one of the older buses in a modern system. It is the bus which connects all the expansion cards in a system to the main chipset, along with IDE and USB.

The PCI bus is a 32-bit wide bus running at 133MHz. Using our familiar calculation we can now easily calculate its maximum bandwidth.

32 (bits) * 133,000,000 (Hz) = 4256,000,000 bits s^{-1}

(4256,000,000/8) = 532MB s^{-1}.

3.3.4   System Architecture

As we told in the Operative Concepts sections three are the requirements that drives the leads the system architecture:

      1. Low power consumption

      2. Low weight and dimension

      3. Resistance to shock and vibration

The SkyArrow has two power generators applied on the engine, the first one is capable to generate 600 W and it is used solely by the avionic users, the second one is intended for the scientific instruments and generates 250 W (ERA generator).

The power available, then, for the ERACam system is 250 W minus the power needed from the Mobile Flux Platform. To evaluate the MFP power consumption we have used a digital multimeter (ISO-TECH IDM 97/97/RMS) to measure both the voltage and the current when both the sensors and the computer of the MFP system are switched on. In total the MFP system needs 170W of power, remaining with an available residual power of 80W.

The cameras that the system should be able to manage for the moment are listed in the following table, where is also reported the power consumptions of the different cameras:

CAMERA	NOMINAL POWER	MAXIMUM POWER
FLIR A40M	9.5 W	15 W
Duncantech MS4100	-	12 W
Sony XC-ST70CE	-	2.1 W
SU 128 1.7-RT	-	8.5 W

Tab 3.2: Cameras power consumptions

The ERACam system, then, could be designed in order to consume maximum 42 W; the idea is to develop a versatile system that could be capable to manage also other cameras. For this reason, and to give a safety margin to the system, our power requirement is assumed to be 30 W.

The second kind of requirement regards the dimension and the weight of the system, where the volume available inside the aircraft is limited. Thus, we have to reduce as much as possible the dimension of the system.

Along with availability of low-power processors and main boards, one of the main challenges of building a small computer is peripheral size and power consumption. The computer industry has provided many solutions in the storage arena such as miniature 2.5" Hard Drives, Slim-CD CDROMs and DVDROMS and lately Compact Flash disk storage solutions used to store operating systems and content.

The form factor devices that answers at the constraints above found on the market is the PC104 plus.

3.3.4.1   PC104 form factor

PC/104 is an ideal system component for industrial applications since it solves space- and power-sensitive constraints, yet it does not sacrifice the architecture, hardware, and software compatibility of a true PC. The modules are small, rugged, and support both the ISA and PCI expansion in self-stacking modules spaced 0.6-inches apart. PC/104 is unique in that it can serve either as a mezzanine bus expansion module, single board computer, or both. The PC/104-Plus architecture was developed to take advantage of the versatility and simplicity of the PC market for embedded applications. Like the desktop PC, PC/104-Plus has the ability to add auxiliary boards to expand the capabilities of the CPU. But instead of using slot cards, PC/104-Plus adds additional modules using stack-through connectors. This has two advantages: it reduces the system size and it makes the system more rugged so that it can better withstand shocks and vibrations.

 A designer can either design and build their own specialty I/O board in-house or find hundreds of vendors with thousand of products worldwide. PC/104 is simply a repackaged, modular version of the PC.

A need therefore arose for a more compact implementation of the PC bus, satisfying the reduced space and power constraints of embedded control applications. Yet these goals had to be realized without sacrificing full hardware and software compatibility with the popular PC bus standard. This would allow the PC's hardware, software, development tools, and system design knowledge to be fully leveraged. In other words, the PC bus had to be standardized while capturing all of the benefits the design engineer wanted from the PC bus.

PC/104 was developed in response to this need. It offers full architecture, hardware, and software compatibility with the PC bus, but in ultra-compact (3.6" x 3.8") stackable modules. PC/104 is therefore ideally suited to the unique requirements of embedded control applications - including full standardization by an international group of over 160 companies who manufacture products based on our PC/104 standard.

The PC/104-*Plus* specification establishes a standard for the use of a high speed PCI bus in embedded applications. Incorporating the PCI bus within the industry proven PC/104 form-factor brings many advantages to its users, including fast data transfer over a PCI bus, low cost due to PC/104's unique self-stacking bus, and high reliability due to PC/104's inherent ruggedness.

A PCI-enhanced version of PC/104 was developed by Ampro Computers, Inc. (Sunnyvale, Calif) and offered to the PC/104 Consortium in September 1996. The Consortium formed a working group to review and finalize the specification, and PC/104-*Plus* was subsequently approved by the Consortium's voting members in February 1997.

The main objective in defining an addition of PCI to PC/104 was to preserve the attributes that have made PC/104 so successful in embedded applications, namely:

- Compact ....3.6 by 3.8 inches (90 x 96 mm) module size
- Self-stacking ....expands without backplanes or card cages
- Pin-and-socket bus connector..........reliable in harsh environments
- Four-corner mounting holes ....resistance to shock and vibration
- Low power consumption ....low power consumption and low heat generation
- Fully PC compatible ....reduced development costs and fast time-to-market

In addition, it was important that the new embedded form of PCI also be . . .

- Stackable and usable along with standard PC/104 modules (in the same stack)

This added requirement enables newly designed PC/104-*Plus* modules to be used in conjunction with the wide variety of preexisting PC/104 "legacy" modules.

Since the 104 pins of the standard PC/104 bus connectors are fully occupied with the signals of the "ISA" (PC/AT) bus, a new 120-pin stackable connector was needed to handle the additional signals of the 32-bit PCI bus. A 120-pin high-density (2mm) connector that precisely matches the stacking and other dimensional requirements of PC/104 was developed.

A unique connector pin "shroud" was also created, to: (1) guide the male portion of the PCI connector as it mates with the female portion of the next connector in the stack; and (2) protect the PCI connector pins, which are slightly thinner and therefore somewhat more vulnerable than those of the ISA connector.

The resulting combination of PC/104 with PCI, called "PC/104-*Plus*," meets all the objectives listed above. In addition, extensive simulations have been used to validate its reliability for both current 33 MHz PCI bus chipsets and future 66 MHz PCI silicon.

The choice was about pc104 for different reasons; on the top there are considerations about the environment where the system has to works. In fact the airborne application, especially with light aircraft such as the SkyArrow, are very hard to manage due to the high level of vibration and possible shocks, for what standard PC form factor with classical slots can have malfunctions. With pc104 the problems regarding those issues are solved by use of four-corner mounting holes present on each device, that doesn't allow the devices to leaves one from another and to increase the resistance to shock and vibrations.

Moreover the system in pc104 form factor is very modular, with the possibility to increase the number of instruments just adding in the stack the device that manage it.

Even in the military market, PC/104, PC/104-*Plus* modules are used for missiles, mobile systems, imaging systems and other high-end digital processing applications. Table 1 shows typical military applications within these areas that use PC/104 COTS boards.

Due to their self-stacking bus, PC/104 and PC/104-*Plus* products are a compact form-factor (3.6" x 3.8") with a high level of expandability. They are also economical since they require no backplane or card cage for interconnection. Low power consumption also helps to make PC/104 family products an optimal choice for several hard applications.

In many cases, an engineer cannot simply select a board-level product that has all the required features and has been officially tested. The selection criteria must extend as well to the technical expertise and the financial stability of potential vendors as well as their ability to meet delivery and service expectations over time. With product selection, it is important to examine the fit between the customer's and the supplier's business models, including such criteria as warranties and long-term availability. Selecting appropriate products often requires the selection of appropriate vendors who will honor long-term availability commitments and agree to adapt and upgrade their products for an extended period of time. Vendors must be

committed to both long-term reliability and long-term availability as the foundations of their businesses.

3.3.5 *Detailed Design*

The realization of an airborne remote sensing system is based on the design and on a research of physical, electric and electronic interface needed for the operation of the system itself.

As we told, the most important parameter is the "*data rate*" that the system has to manage. In particular, it determines both the type of CPU and the peripheral interfaces.

Then the choice of the CPU is determined by the trade-off between the frame rate needed for the standard remote sensing mission and the maximum frame rate that the frame grabbers on the market can give.

For acquisition time and position of the images acquired by the system it's used the novatel GPS unit installed on the nose of the aircraft. This GPS unit is also used from the Mobile Flux Platform to refer each data at the time and positions held by the aircraft during the flight. The GPS unit sends trigger signals at all the sensors to synchronize their acquisition. To collect instantaneously also the remote sensed images we use the PPS (Pulse Per Second) output from the novatel to give triggers at both the cameras and framegrabbers at each second. When the trigger signal is acquired by the framegrabbers, the cameras acquires the images and by serial communications time and positions are read, and the images are stored by cameralink for the MS4100, and by firewire for the Flir.

Figure 3.9 shows the connection between GPS, cameras and frame grabbers.

With the acquisition time by the novatel GPS unit, is possible also to refers the images collected at the attitude of the aircraft, since the two systems (MFP and ERACam) share the GPS time and the trigger signals. Obviously we are able also to refers at each image the following parameters:

- Air temperature
- Dew point temperature
- Net radiation
- PAR radiation
- Wind magnitude and direction
- Carbon dioxide and water vapour content

These parameters are useful when radiation transfer model are used to characterize the atmosphere between the soil and the aircraft.
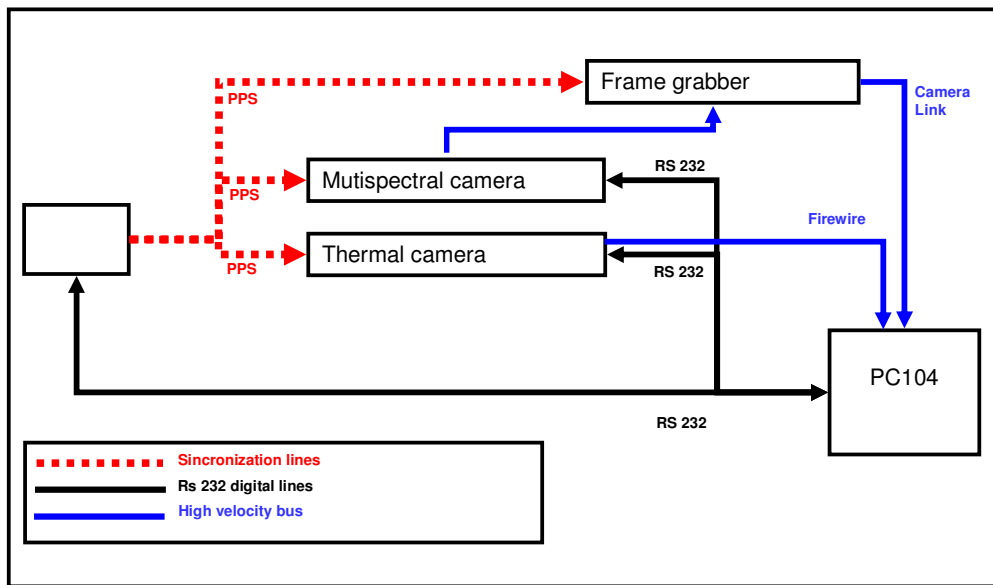

Fig 3.9: System concept diagramm

Below description of the component choose.

The M570 board is a new CPU module (1Ghz), available in a standard PC/104-Plus format, based on VIA EDEN processors, an x86 family compatible processor, compatible both with Intel MMX instruction set and AMD- 3Dnow!. 1 SODIMM memory slot is provided for the insertion of up to 512MB SDRAM. On the module is realised a PC-like architecture, with a VIA VT8606 "Twister-T" Northbridge and a VIA VT82C686B Southbridge.

The VIA VT8606 "Twister-T" is an high performance Northbridge, which provides control of SDRAM (supports PC100 and PC133 SDRAM) and implements a PCI rev. 2.2 Bus Controller. PCI bus is besides made externally available through the PC/104-Plus Connector (this is optional). It integrates a Savage4 AGP4X Graphic Core, which is able to control a CRT screen (with a resolution up to 1600*1200 with 16.8 million colours or 1920*1440 with 64K colours, depending on system memory frame buffer size) and simultaneously drive TFT Flat Panels through its dual channel LVDS interface. It is possible to reach a resolution up to 1280*1024 on TFT displays. Driving voltages for LCD display are generated on board.

The VIA VT82C686B Southbridge provides to all other features of this PC-like module: first of all, it manages EIDE interface, which is available through a standard 44 pin connector, able to accept both standard 2.5" Hard Disk Drives (UltraDMA-66 mode is supported) and

Solid State Disks (DOM), which can be supplied by SECO. On board there is also an hole for fastening of DOMs simply by using two screws and a 10mm spacer, in order to avoid problems in environments with potential vibrations problems.

The Southbridge besides take control of 16-bit ISA bus, that is the main interface of the M570 module through the standard 64+40 pins PC/104 connector.

Other peripherals, directly controlled by the Southbridge, are the 2 USB 1.1 ports, the mouse and keyboard interface and the two standard RS-232 Full-Modem COM ports (one of them configurable to work in RS-232, RS-422 or RS-485 mode).

Besides, it controls the parallel port, which is BIOS configurable to work in standard XT/AT mode (SPP), bidirectional mode, ECP mode, EPP mode and can also be programmed for the connection of an external Floppy Disk Drive.

The board has also an Ethernet controller on, with installed 10/100BaseT interface, and an amplified audio interface, with two channels amplified to 1W per channel.

It requires only an external +5VDC and generates all the internal voltages through an additional power supply module M571, mounted vertically on two dedicated connectors. On the power connector is also possible to connect +12VDC and -12VDC : +12VDC is internally used to produce a MOSFET switched supply voltage for inverter units for flat panels' lamps; -12VDC is not internally used. Both these voltages are available on PC- 104 and PC/104+ connectors for expansion units requiring them.

For the safety of the module, it monitors temperature, fan speed and voltages, in order to avoid dangerous situations in case of overheating.

Fig 3.10: CPU M570 1Ghz

The PCI-1428 is a highly flexible IMAQ device that supports a diverse range of Camera Link-compatible cameras from various camera companies. The PCI-1428 acquires digital

images in real time and stores the images in onboard frame memory or transfers them directly to system memory. Featuring a high-speed data flow path, the PCI-1428 is ideal for both industrial and scientific environments.

The PCI-1428 supports the Camera Link Base configuration, and the VHDCI 68-pin connector provides access to the 8-bit x 4 mode of the Camera Link Medium configuration.

Easily synchronizing several functions to a common trigger or timing event is a common challenge with image acquisition devices. The PCI-1428 uses the Real-Time System Integration (RTSI) bus to solve this problem. The RTSI bus uses National Instruments RTSI bus interface and ribbon cable to route additional timing and trigger signals between the PCI-1428 and up to four National Instruments DAQ, motion control, or IMAQ devices. The RTSI bus can even synchronize multiple IMAQ hardware captures.

Fig 3.11: PCI 1428 Camera Link

The ADP-1012 backplane was designed to enable the user to obtain rapidly a development or demonstration system, for CPU modules in PC/104-Plus (or PC/104) standard and especially for CPU modules belonging to the Eurotech PC/104-Plus products family. The ADP-1012 backplane:

1 - allows the simultaneous use of PC/104-Plus modules and standard ISA/PCI cards

2 - provides the connection to a standard PC/AT power supply unit (optionally ATX)

3 - comes with a DC/DC converter to generate the 3,3V voltage (not present in the PC/AT PSU)

4 - is supplied with a flat cables set enabling the connection of the serial ports, the parallel port and the keyboard on DB9, DB25 and DIN respectively (a PS/2 mouse is available as option).

5 - includes a speaker, a reset pushbutton and a backup battery (for the Real Time Clock).

It was choose because the not availability in the first period of developing the system, of a camera-link frame-grabber in Pc104 form factor, and then to use a frame-grabber in PCI form factor made by National Instruments.
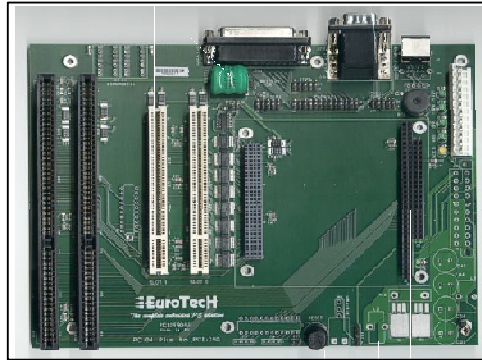

Fig 3.12: Back Plane adapter PCI/PC104

The Em104P-1394 is a high performance Controller providing 3 serial ports conforming to the IEEE-1394 OHCI specification - popularly known as FireWire. The Em104P-1394 provides an ideal interface for attaching high speed Audio, Video and Storage peripherals to an embedded system. Automatic detection and configuration of devices (without the need for on-board jumpers) ensures robust system operations and high reliability . The Em104P-1394 provides a distinct advantage over other communications and interfacing controllers by allowing multiple devices to be attached simultaneously on the high serial bus. Three serial ports are provided enabling up to 63 devices to be connected with cable lengths of over 4.5M. The Em104P-1394 is supported by a suite of drivers for Windows98SE/Me/2000/XP and Mac OS. The DTX3-FW is an ideal solution for solid-state video recording, machine vision, digital image capture and processing and hot-pluggable storage peripheral interfacing.
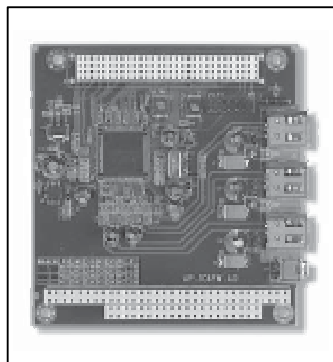
Fig 3.13: em104P 1394 card

The M442 module is a low-cost integrated module which offers the chance of expanding the communication possibilities of a PC/104 based system.

The M442 module integrates 4 serial ports: two of them are RS-232C standard serial ports in a Full Modem configuration. The other two ports can be settled to work also in RS-232C Full Modem mode, or in a RS-422 or RS-485 mode.

The control of the serial ports is made by a 16C554 Quad-UART controller, which can guarantee up to 1.5 Mbps transmit/receive operation (24MHz max), and offers·16 byte transmit FIFO and 16 byte receive FIFO with error flags.

The ports are by default set as standard COM's, but it is possible to map the ports at user decided addresses, 8-bytes spaced each other. Even IRQ lines are software configurable.

All these features are made available in a standard PC/104 module: all PC BUS signals are available on a male/female strip connector (2.54mm pitch), common to all **PC/104** modules. It allows an easy direct interconnection, without the need of a passive back plane. By fixing the modules with plastic screws and spacers, then, it is possible to reach a good mechanical stability.

Practically, a system composed of some modules maintains the same mechanical dimensions of 3.5" x 3.8" (90 x 96 mm), growing in height by 0.6" (15.2 mm) for each added module: this represents a very good choice for assembling complete systems requiring reduced dimensions.
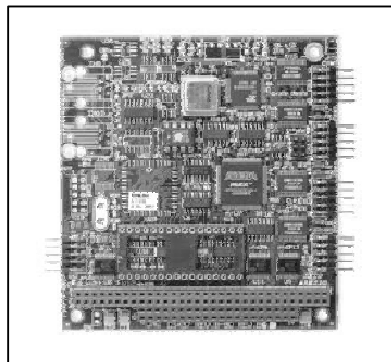

Fig 3.14: RS232 card

The Matrox Meteor-II /Camera Link frame grabber acquires digital video from cameras compliant with the Camera Link Specification. The board is available for the PCI and

PC/104-*Plus* form factors. This device will be installed in the next ERACam system already in developing in the ERA Laboratory

For the next generation system, we want manage the thermal camera and both the multiospectral camera (CIR/RGB) at same time. To do this job we have selected the presented framegrabber that allows also to decoding each pixel of the image at 10bit.

The Matrox Meteor-II /Camera Link interface features two Camera Link-compliant video input connectors, and can grab data from Camera Link area or line scan video sources, including one, two, or four tap monochrome sources, and component RGB sources. Both form factors support acquisition from one camera, or simultaneous acquisition from synchronized cameras, either two monochrome, or one monchrome and one RGB. You can also connect and switch (non-simultaneous acquisition) from between two monochrome, two RGB, or one monochrome and one RGB source.
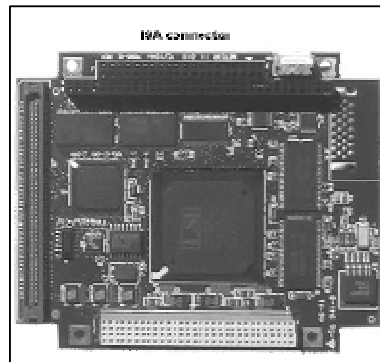
Fig 3.15: Matrox Meter II Camera Link

3.3.6   Implementation

The system was assembled and camera placed in a aluminium rack (fig 3.16) e mounted on the bottom place of the fuselage of the aircraft.

Figure 3.16 shows the system both with and without the aluminium case, where is possible to identify also the ATX power supply used to give the power at the backplane adapter between PC104 and PC104plus. Figure 3.17 shows the both the cameras and the laser altimeter installed on the bottom plate of the aircraft. To dump the rack from shock and vibration we have used two standard dumpers.

Fig 3.16: ERACam system with and without the case

Fig 3.17: The cameras and laser installed in the aircraft

The software to control the acquisition and the camera parameters was developed in LabView environment. Two versions were developed, one for the automatic mode available when the mission is conduct without the operator (pilot alone), and one for the manual mode available when the operator is present onboard the aircraft.

Figure 3.18 shows the cockpit of the aircraft during a mission flight, in the bottom of the image is highlighted the LCD screen with the control software in automatic mode.

Fig 3.18:The ERACam software visualization screen in automatic
mode on the LCD screen of the cockpit

Figure 3.19 shows a zoom of the automatic software where is possible to identify the following leds:

- GPSTime status: gives information about the serial communication between the system and the novatel GPS
- Snap status: gives information about the status of the acquisition by the cameras
- Trigger status: gives information about the trigger that the GPS sends to the cameras
- Save status: to ensure that the images are correctly stored on the hard drive.

More is possible to have information about the time of acquisition, the second since the start of the acquisition, the images saved on the hard drive.
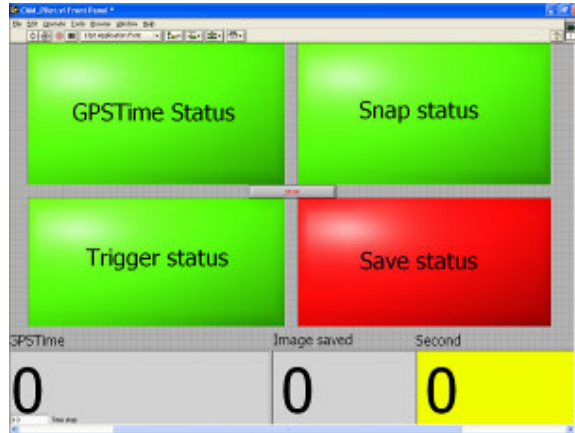
Fig 3.19:The ERACam software visualization screen in automatic mode

In figure 3.20, instead, is showed the acquisition software that works in manual mode. To manage it the operator must be present on the aircraft, because there are too many controls to be done from the pilot. With it is possible to set some parameters:
- gain of each channel
- integration time of each channel
- frame rate of acquisition

- etc

The images acquired is also displayed in real time on the screen, than the operator can apply correction if something should not works

Fig 3.20:The ERACam software visualization screen in manual mode

3.3.7   *Flight test and flight Campaigns*

Following the first test performed in the Napoli's area. It is showed the flight planning (figure 3.21), and the execution (figure 3.22). The flight was planned at different altitude to recover images at different scale and resolution, so has been possible to evaluate the actual definition af the camera at different altitude.

Fig 3.21:Flight planning over the Solfatara (Naples)
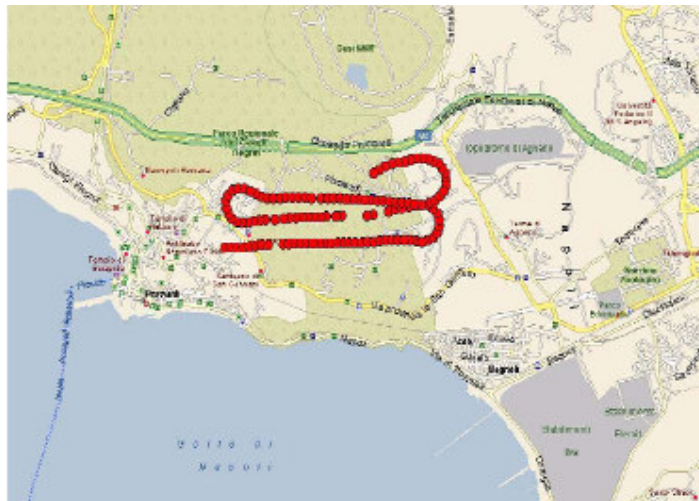
Fig 3.22:Thermal mapping of the Benevento province area

Problems of vibrations during the flight caused some problems at the system that some time lost images as it can seen from figure 3.22, where are reported the location of the centre of each image acquired. However the imposed overlap has ensured the coverage of the observed

area. Figure 3.23 is an impressive thermal image of the solfatara site, where the temperature in the hot points is up to 60°C, instead the mean background temperature is of about of 15-20°C.

It is also reported as a product example, the temperature mapping instead of pixel by pixel related to specific range of temperature (figure 3.24).
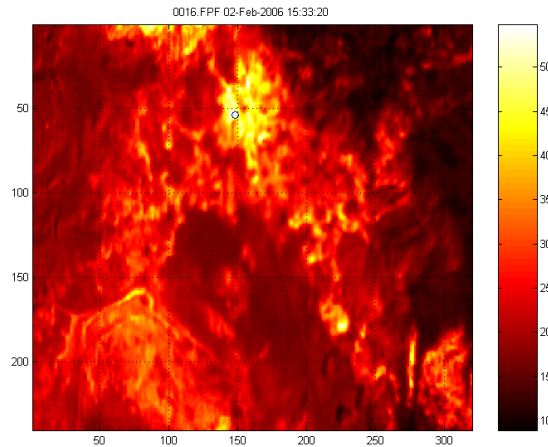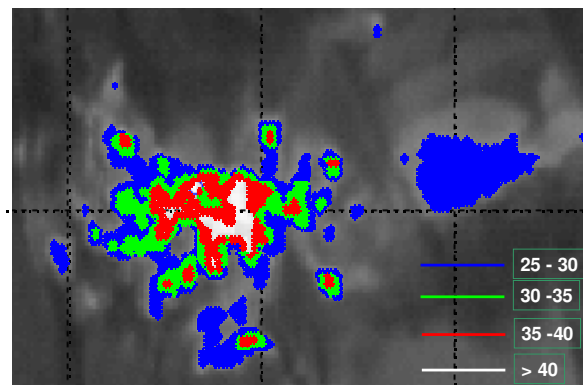

Fig 3.23:Thermal image of the Sofatara site

Fig 3.24:Thermal mapping of the Solfatara site

The system was then fully mature to be utilized for research flights within ISAFoM scientific missions, it has been tested on several campaigns made around the Europe region. Following a brief list:

- EC 6PQ Carboeurope-IP "*Regional Experiment Intensive Campaign*" over Les Landes area (France), NDVI and thermal mapping of the region.

- EC 5PQ MIND project over Las Majadas (Extremadura, Spain).
- EC 5PQ MIND project over Tolfa (Viterbo, Italy)
- Prusst Calidone project, multispectral and thermal mapping of the Benevento's rivers (Italy)

Figure 3.25 shows CIR and thermal images over Las Majadas site, with the track of the aircraft during EC 5PQ MIND campaign.

Figures 3.26 and 3.27 show respectively the multispectral and thermal images over the city of Benevento the first one, and a therma mapping application of the river of the city.
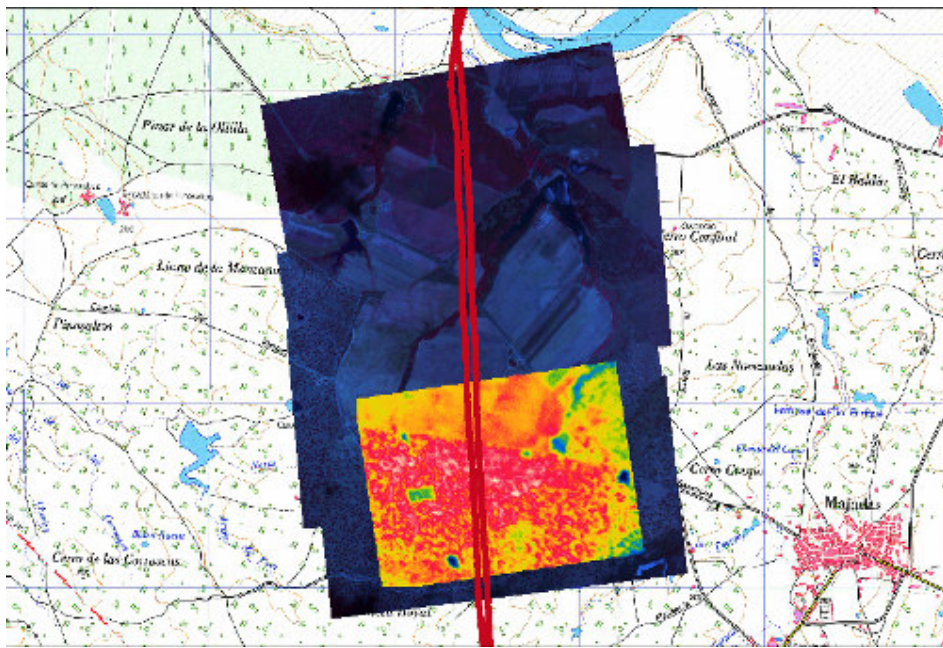
Fig 3.25:Multispectral mapping with CIR and thermal images overlapped on a map of the "Las Majadas" (Spain) site on June 2005
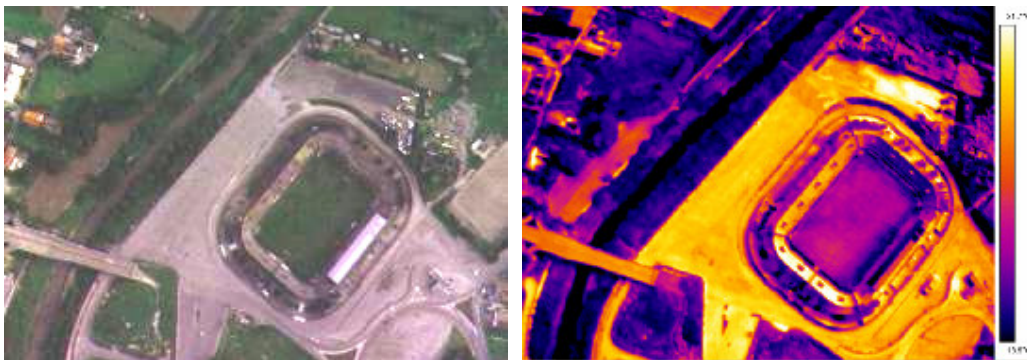
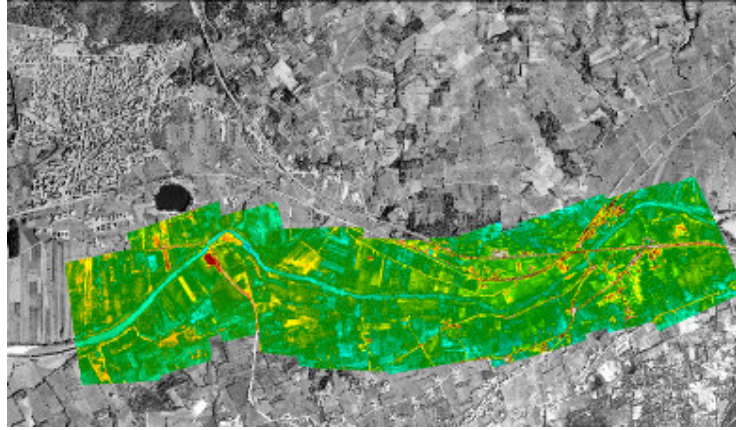*Fig 3.26:RGB and thermal images over Benevento City*

Fig 3.27:Thermal mapping of the Benevento province area

Chapter 4

RADIOMETRIC LABORATORY CALIBRATION OF A THERMAL CAMERA

4.1 Introduction

In this chapter is described the radiometric calibration of the FLIR A40M. The maker of this infrared camera calibrates their cameras automatically prior to shipment for temperature and this sometimes gives the perception that temperature is the only measurement required or available.

Some reasons lead the calibration of the thermal camera; in several applications related to ecosystems analysis or similar, quantify the radiant energy incoming from targets at given temperature is needed; moreover the maker calibrates the camera for a large range of temperatures, diminishing the total accuracy of the camera.

Calibrating the camera in a short range of temperature comparable with the temperatures commonly measured during remote sensing missions of the SkyArrow, this work tries to improve the accuracy of the camera and to give the possibility to retrieve also radiance information from the thermal images collected.

For many years the scientific, range and phenomenology, and research market has seen major advancements in thermal imaging systems to help identify, measure, and track the heat signatures/energy signatures of various sources, both friendly and foe. The fast paced sensor and software advancement has sometimes resulted in misused terms and improper data representation.

For example, infrared (IR) cameras have gotten smaller, faster, smarter, less expensive and easier to operate creating a "point and shoot" type expectation. This ease of operation in itself is a great for the infrared measurement community as a whole; however, this has sometimes

causes many newcomers to the industry to assume that temperature and radiometry are interchangeable measurements and equivalent.

4.2 Definitions

Is needed to understand the basic difference between thermography and radiometry to help determine the appropriate measurement technique for their application. A few common thermographic and radiometric definitions are provided below.

Thermography is simply defined as the measurement of temperature variations. The typical unit of measure for imaging thermography is temperature, i.e. degrees Celsius, degrees Fahrenheit, or Kelvin.

Radiometry is simply defined as an absolute measurement of radiant flux. The typical unit of measure for imaging radiometry is radiance [Watts sr^{-1} m^{-2}].

In even simpler terms think of thermography as "how hot" the object is, where as radiometry is "how much energy" the object is giving off. Albeit related, "how hot" an object is and "how much energy" an object is giving off are not the same things. Other terms that are commonly used in the range community include the following.

- Irradiance – The amount of energy that falls onto a sensor per unit area. [W/cm2]
- Radiant Intensity – The amount of energy per solid angle emitted by a target or energy source. [W/sr]
- Mean Temperature – The average temperature of a source. [^{o}C, ^{o}F, or K]
- Blackbody – An object (surface of cavity) that emits energy according to Planck's blackbody equation.
- Emissivity – The ratio of the infrared radiation emitted by a surface to that emitted by a blackbody at the same temperature and wavelength.
- Hardbody – A solid object or material that behaves like a blackbody (emissivity=1.0) or greybody (emissivity<1.0).

4.2.1   *Spectral Bands of Interest*

Figure 4.1 below is a chart identifying the traditional sensor technologies with respect to the electromagnetic spectrum. The two most common types of sensor technologies are Thermal and Photon. Thermal sensor technologies include those where resistance or capacitance changes with respect to heat incident on the sensor material. Such sensors include bolometers and microbolometers.

A bolometer is a resistor whom resistance is a function of it's temperature. Semi-conductors bolometer usually drop in resistance as temperature rises, while metals exhibit the opposite behaviour. By measuring the fractional change in resistance, one can measure a temperature change in the environment.

Photon sensors are more common in the range community due to higher sensitivity and higher spatial resolution. Photon sensors are measured with respect to the amount of photon flux (flux density) that is incident on the sensor material. Common photon sensors include Indium Antimonide (InSb), Indium Gallium Arsenide (InGaAs), or Quantum Well Infrared Photodetector (QWIP) detector materials.

Some other common sensor materials not shown on Figure 4.1 are Mercury Cadmium Telluride (MCT), Platinum Silicide (PtSi), and Amorphous Silicon.

As seen on Figure 4.1, many detector materials cover a distinct spectral range. For instance, InSb can be configured to detect photons with wavelengths as low as 1.0 microns and as high as 5.5 microns. Because of this phenomenon, the ability to add special customized filters to any of these systems helps one narrow the system's spectral response and achieves further measurement flexibility. Traditionally, cold filters, filters that are stabilized at or near the same temperature as the detector, are the most accurate and desired filters for signature measurements. Warm filters, filters that are commonly screwed onto the back of the optical lens outside of the detector/dewar assembly, are also commonly used but tend to provide more radiometric calibration uncertainty due to varying IR emission with ambient temperature changes.
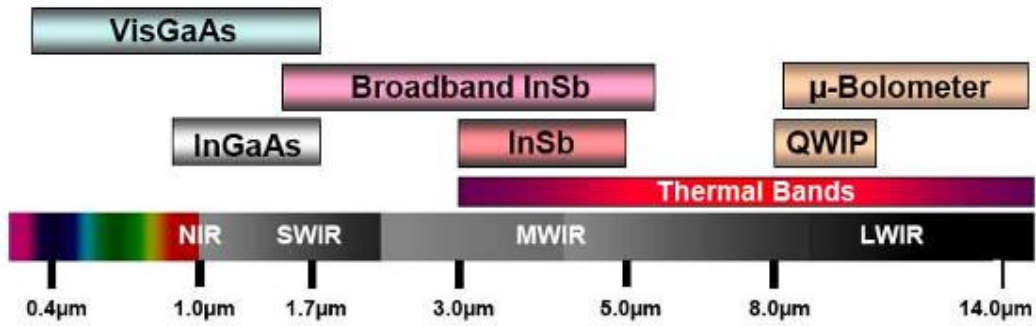
Fig 4.1: traditional sensor technologies

4.2.2.1   Microbolometer technology

VOx microbolometer technology is a thin layer of vanadium oxide and it's sandwiched two thin insulating layers. VOx is a temperature-sensitive material, undergoing a larger fractional change in resistance for a given temperature change than many other semi-conductors.

Individual sensor elements use the change in electrical resistance of a VOx resistor deposited onto the tiny "platelets" fabricated by silicon micromachining in a silicon foundry. Incoming target radiation heats the VOx causing a change in electrical resistance, which is readout by measuring the resulting change in bias current. The structure can be dimensioned to operate at 30 Hertz. That is, the thermal conductance of the isolating legs can be adjusted to match the time-constant for 30-hertz operation. An example of a microbolometer element is pictured below.
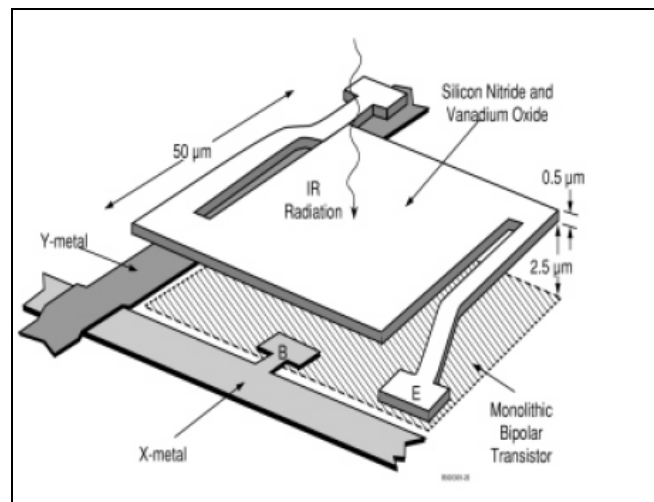
It consists of a two-layer structure. An interconnecting readout integrated circuit (ROIC) is applied to the silicon process wafer and then the microbolometer structure is built on top of the readout circuitry. First a pattern of islands _ wavelength thick are deposited on the readout circuitry. Most of today's camera manufacturers use the 320 by 240 microbolometer array. However there is an excellent alternative for many commercial applications – the 160 by 120 array. The smaller array and its resulting camera can be produced at a much lower cost. Far more arrays can be produced on a single wafer and the yield is higher for the smaller array. In addition, one of the most expensive components of an infrared camera is the lens and its cost is proportional to the array size.

The ROIC is a standard silicon based circuit. It measures the IR signal from each bolometer and sends the data off-chip in a digital format.

The ROIC first biases each pixel to a voltage V_{biases} for a short period of time. Global heating compensation is done to correct for the bolometer change in resistance caused solely by bias heating. A coarse off-set adjustable for each pixel, accounts for process variations in resistance.

The offset, calculated on a uniform image, tunes the output of each bolometer signal into an analog to digital (A\D) converter. Once in a digital format, the data is passed to the interface electronics and shipped off-chip to a signal processing card (SPC) that provides fine gain and offset correction so the image is uniform.

A uniform black shutter (see figure 4.3), controlled by SPC, is used to get a uniform image for correction data. The SPC first records a frame looking at the shutter, then stores whatever value is subtracted from each pixel value to get the output exactly in the middle of the range. A fine offset correction is done every few minutes to correct for slow drift in pixel offset.
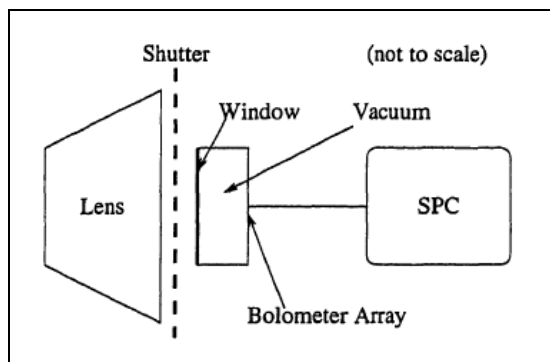

Fig 4.3: Lens and shutter location

4.2.2 Relationship between Radiance and Temperature

An effective blackbody temperature measurement can be derived from a radiance measurement by applying a radiometric calibration, temperature vs. radiance model, and emissivity of the material under test. Radiance values are first obtained by generating and applying a radiometric calibration.

The next couple of paragraphs in conjunction with Figure 4.2 help define and outline the basic steps involved in calibrating an infrared camera system in order to produce a radiometric measurement and, ultimately, a thermographic measurement.
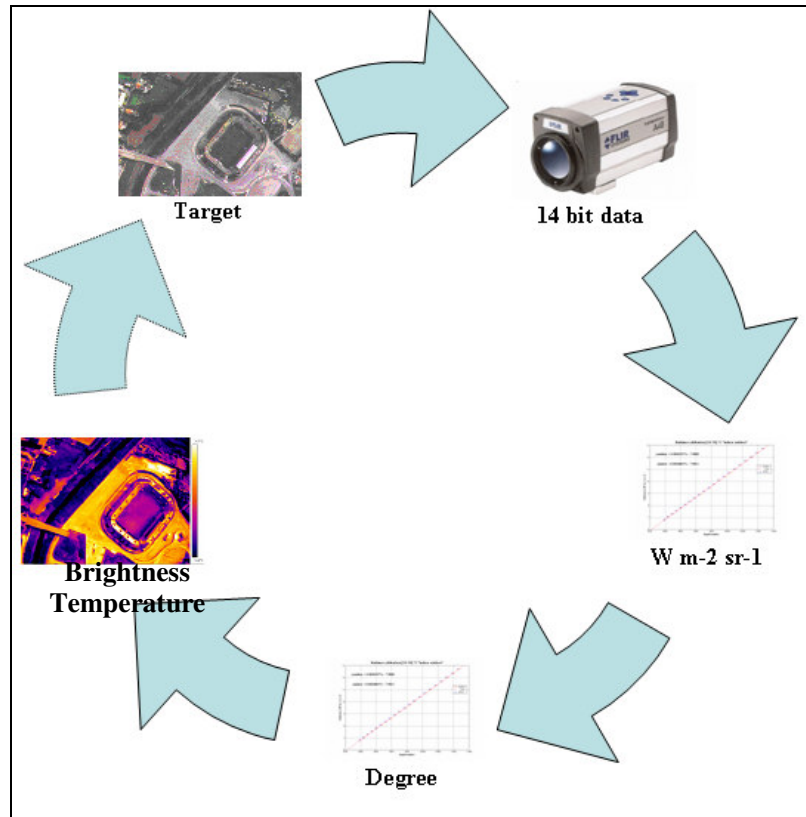

Fig 4.4: Operational diagram to obtain brightness temperature from a target

Starting in Figure 4.2 at 9 o'clock and moving clockwise, the object, in this case a stadium, has a certain energy signature. This signature is first seen by the infrared camera itself through heat as found with a thermal detector such as a VOx microbolometer. The amount of energy that is seen by the infrared camera/detector produces a signal voltage and therefore creates a

digital count level through the system's A/D converter. In our case, the FLIRA40M camera has a 14-bit dynamic range which will create count values ranging from 0-16383. The more IR photons incident on the camera's detector in the detector's spectral band, the higher the digital count. Moving clockwise in Figure 4.2, the digital counts are being transformed into radiance values. However, before this can happen, the infrared camera system needs to be calibrated using a blackbody source for the temperature ranges of interest. Calibration of the infrared system is done by measuring the digital counts versus a series of known temperature and radiance levels produced by a uniform blackbody with a known emissivity and known distance. Once the imager's counts for each blackbody temperature measured are logged, the data are then passed through an in-band radiance curve fit algorithm to produce the appropriate in-band radiance vs. counts values given the camera system's normalized spectral response function.. Next step is to create a lookup table or curvefit to relate the radiance values of a measured object to its effective blackbody temperature. Generating temperatures as described earlier is a more difficult task if the object of interest has multiple emissivity and material characteristics. However, if one knows the target's emissivity then the temperature can be derived from the radiance calibration using the following three different methods.

1. Using Plank's Equation – assumes a spectral bandpass and calculates temperature using Planck's equation.
2. Using a curvefit of temperature vs. radiance from your radiometric calibration
3. Using a Look up Table created the same data used in method 2 above.

Applying this equation to the object of interest is one way to determine the temperature of the object from its measured radiance. Notice that the relationship between radiance and temperature is not a linear relationship.

4.2.3   *Detector Characteristics*

The performance of optical detectors is commonly described by a number of different figures of merit, which are widely used throughout the field of optical detection. They were developed originally to describe the capabilities of a detector in responding to a small signal in the presence of noise. As such, they are not always pertinent to the detection of laser light. Often in laser applications—for example, in laser metalworking—there is no question of detection of a small signal in a background of noise. The laser signal is far larger than any other source that may be present. But in other applications, like laser communications, infrared thermal imaging systems, and detection of backscattered light in laser Doppler anemometry, the signals are small, and noise considerations are important. It is also worthwhile to define these figures of merit because the manufacturers of detectors usually describe the performance of their detectors in these terms.

4.2.3.1   *Responsivity*

Responsivity gives a measure of the detector's sensitivity to radiant energy. It's specified as the ratio of the detector output to the light input. For a detector that generates a current output, the responsivity is the ratio of the root mean square (rms) signal current (measured in amperes) produced by the detector to the incident radiant power (measured in watts) at the entrance to the detector. If the signal output is represented as a voltage, it's the ratio of rms signal voltage per watt of incident radiation. Equations 1 and 2 show these relationships. Thus, the responsivity is essentially a measure of the effectiveness of the detector for converting electromagnetic radiation to electrical current or voltage. Responsivity will vary with changes in wavelength, bias voltage, and temperature. Responsivity changes with wavelength since the reflection and absorption characteristics of the detector's sensitive material change with wavelength. Temperature changes affect both the optical constants of the detector material and its collection efficiency.

4.2.3.2   *Spectral Response*

If we plot the absolute responsivity as a function of wavelength, we have what is called a spectral response curve. This curve is commonly shown as a relative response curve in which the peak of the response curve (highest responsivity) is set equal to 100%. All other points are

relative to the peak. A common practice is to make an absolute calibration only at the peak of the response curve. Thus, to determine the absolute responsivity at some other wavelength, we find the percent relative response at this wavelength. Then we multiply it by the absolute value of amps/watt at the peak of the curve.

4.2.3.3   Noise Equivalent Power and Noise equivalent Delta Temperature

The responsivity defined above gives a measure of how much output you can expect from a given detector for a specified input. For many optical applications, the signal is much larger than any noise source that may be present. The responsivity alone is adequate to characterize detector performance. But in many other situations you must detect a small signal in the presence of noise. For example, in optical fiber telecommunications, you must detect a laser signal after it has travelled many kilometers through the fiber. The available signal may not be much larger than the noise sources. You must distinguish the signal from the random fluctuations that make up the noise. In this case, other detector parameters become more important than the responsivity.

One such parameter is the noise equivalent power (often denoted NEP). The NEP is the radiant power that produces a signal voltage equal to the noise voltage from the detector.

Before we describe the NEP in detail, let's discuss noise sources in photodetectors. Noise is a rather profound subject. In this module we can do little more than present the fundamental ideas and apply them to photodetectors. Noise can be any undesired signal. It can be divided into two broad categories: externally induced noise, and internally generated noise. External noise, as the name implies, includes those disturbances that appear in the system as a result of an action outside the system. Two examples of external noise are hum picked up from 60-hertz power lines and static caused by electrical storms. Internal noise, on the other hand, includes all noise that's generated within the system itself. We now know that every resistor produces a discernible noise voltage and every electronic device (such as vacuum tubes and semiconductor elements) has internal sources of noise. You can think of internal noise as an ever-present limit to the smallest signal that the system can handle. The NEP is related to the internal sources of noise generated within the photodetector.

The following types of noise are those most likely to be found in a photodetector and bolometer systems:

a. *Johnson Noise*: Any resistor acts as a generator of noise that is called Johnson noise. The mean square noise voltage is directly proportional to the value of the resistance. Johnson noise

is sometimes called thermal noise. It occurs in all conducting materials. It's a consequence of the random motion of electrons through a conductor. The electrons are in constant motion, but they collide frequently with the atoms or molecules of the substance. Each free flight of an electron constitutes a minute current. The sum of all these currents taken over a long period of time must, of course, be equal to zero. But their ac component is Johnson noise.

   b. *Shot Noise*: The term "shot noise" is normally associated with vacuum tubes in which the stream of electrons creates a noise due to the random fluctuations in the rate of arrival of electrons at the anode. This noise may be likened to the noise of a hail of shot striking a target. Hence the name shot noise.

   Shot noise is present in all photon detectors due to the random arrival rate of photons from the source of radiant energy under measurement and background radiation. This shot noise is often called "photon noise." Photon noise is the true ultimate limitation to detector performance. Even if all internal noise sources were eliminated, photon noise would set the ultimate limit for detector performance.

   In semiconductor diodes and photomultipliers, the shot noise associated with the random generation of carriers is the major noise source. In photoconductors the major source of noise is associated with both the generation *and* the ultimate recombination of the charge carriers. That is, it's associated with the fluctuations in the rate at which charge carriers are generated and recombine. It's often referred to as generation-recombination (g-r) noise.

   c. *Excess Noise***:** At low frequencies, there are many types of noise for which the noise power varies inversely with frequency. A common term for this type of noise is 1/f (pronounced one over f) noise. It's also known as excess noise since it exceeds shot noise at frequencies below a few hundred cycles. A variety of names are used to designate the 1/f noise associated with specific devices. It's called modulation noise in semiconductors such as transistors, diodes, and detectors; contact noise in carbon-type resistors and their electrical contacts; and flicker noise in vacuum-tube cathodes. There are no simple mathematical expressions to describe these types of noise. In fact, some are not well understood to this day. The important consideration about these sources of internal noise is that any one or a combination of the noise currents will determine the lower limit of detectability of a photodetector system.

   Now we have a basic foundation on the subject of noise. We can discuss how manufacturers of photodetectors rate their devices in terms of noise. This lets us compare different types of detectors based on their noise equivalent ratings.

The amount of optical power incident on the surface of a photodetector that produces a signal at the output of the detector just equal to the noise generated internally by the detector is the noise equivalent power (NEP). This is usually the minimum detectable signal level. (Signal-to-noise ratios less than 1 can be useful under some circumstances). Since, under these conditions, the signal power is equal to the noise power, we can say the signal-to-noise ratio is equal to one.

Another computable figure of merit more suitable for routine testing is the noise equivalent temperature difference (NEDT). NEDT is the temperature difference of a scene needed to give a unity signal to noise ratio. Sometimes it is divided into spatial and temporal components in an attempt to better model the human preferences.

The minimum resolvable temperature difference (MRTD) is a purely human test of system performance. It is defined as the minimum temperature difference between 4-bar target and background needed for a trained observer to resolve the image. From a user standpoint, MRTD is a better predictor of system performance. From a routine testing standpoint, NEDT is faster and easier to measure.

For each channel is then possible to derive noise equivalent power (expressed in W) and the noise equivalent delta temperature (expressed in mK) as:

$$NEP = \frac{\sigma_c \times A \times \Omega}{S} \qquad (4.1)$$

$$NEDT = \frac{NEP}{\frac{dL}{dT} \times A \times \Omega} = \frac{\sigma_c}{S \times \frac{dL}{dT}} \qquad (4.2)$$

A similar measure is often used to describe the performance of an entire system. It's noise equivalent irradiance (NEI). NEI is the radiant flux density necessary to give an output signal equal to the detector noise. The NEI is given by the following equation:

$$NEI = \frac{\Phi_e \times V_n}{V_s} \qquad (4.3)$$

where:

NEI = Noise equivalent irradiance in W/cm^2 to produce an *S/N* ratio of unity at the output of the system.

V_s = rms value of signal voltage at output of detector.

V_n = rms value of noise voltage at output of detector.

When used to describe the performance of an entire system, NEI expresses the irradiance (W/cm2) at the entrance to the detector required for an S/N ratio of unity at the output of the system electronics.

4.2.3.4   *Detectivity (D) And D**

When we compare several detectors, the one with the highest output for a given radiation input is said to have the best responsivity. However, when we compare the detectors in terms of their detecting ability (that is, in terms of the minimum detectable radiant flux) the best detector is the one with the lowest NEP. If we take the reciprocal of the NEP, we can define a new term, called the detectivity. The higher the value of the detectivity, the better the detector. The detectivity (*D*) is a function of the following:

1. Area of detector.
2. Bandwidth of the measurement system.
3. Bias voltage.
4. Wavelength of radiation.
5. Temperature of detector.

The NEP—and hence the value of detectivity—depends on the area of the detector. This makes it difficult to compare the intrinsic properties of two different types of detectors. To remove this dependence, we use another term, called D* (pronounced "Dee-star"), to rate photodetectors. D* is given by the following equation:

$$D^* = \frac{\sqrt{A_d \times B}}{NEP} \tag{4.4}$$

D* = Spectral detectivity, cm (Hz)$^{1/2}$W^{-1}.

where:

A_d = Area of photodetector, cm2.

B = Bandwidth of measuring system, hertz.

NEP = Noise equivalent power, watts.

Note the rate unusual units, cm $(Hz)^{1/2}W^{-1}$, in which D* is expressed. The value of D* is independent on the area of the detector. Thus D* is popular as a measure of the intrinsic merit of a detector material. It's often used to compare detectors of different types.

There's a convenient way to remember the significance of D*. Recall that it is the signal-to-noise ratio when one watt of radiation is incident on a detector with a sensitive area of 1 cm2 and the noise is measured with an electrical bandwidth of 1 hertz. Thus, the term D* is a normalized detectivity that's convenient for comparing the performance of detectors with different areas when used in circuits with different bandwidths.

It's customary for manufacturers to write D* followed by three numbers in parentheses. Thus, D* (850, 990, 5) = 6.3 * 101 3 cm $HZ^{1/2}$/watt means that the measurement was made at a wavelength of 850 nanometers and bandwidth of 5 hertz. If the bandwidth is unit, the last term is omitted, since unity bandwidth is implicit in the definition of D*.

4.2.3.5   Quantum Efficiency

Quantum efficiency (QE) is the ratio of countable events (such as photoelectrons or electron-hole pairs) produced by the incident photons to the number of incident photons. Note that it doesn't include subsequent photons produced by amplification processes. If, over a period of time, an average of 10,000 photoelectrons is emitted as the result of the absorption of 100,000 photons of light energy, then the quantum efficiency will be 10%. Quantum efficiency is related to the responsivity as follows: It's equal to the current responsivity times the photon energy in electron volts of the incident radiation. It's normally expressed as a percentage. (Note, however, that responsivity sometimes includes subsequent gain.) Quantum efficiency is just another way of measuring effectiveness of the basic radiant energy in producing electrical current in a detector. It's given by this simple equation:

$$QE = R_d \frac{12408}{\lambda_\chi} \times (100) \tag{4.5}$$

QE = Quantum efficiency in percent.

where:

R_d = Responsivity of detector l c in m A/m W.

-83-

l c = Wavelength in angstroms (Å).

Note that the manufacturer has plotted the quantum efficiency (electrons/photon) curve as a function of wavelength as indicated in Figure 3. It's interesting to note that the quantum efficiency of the dark-adapted human eye is a maximum of approximately 3% at a wavelength of 5100 Åm m. This means that the signal-to-noise performance of the eye is equivalent to that of an ideal detector that produces one recorded photo-event for each 33 incident photons within the wavelength band to which it is most sensitive.

For most material, the quantum efficiency is very low. But on the best sensitized commercial photosurfaces, the maximum yield may be as high as three photoelectrons for four light quanta. Another exception to the above statement is the avalanche photodiode. Here the quantum efficiency may exceed unity, since avalanche photodiodes provide internal gain and may deliver more than one electron for each photon of incident light.

4.2.3.6   Linearity

Photodetectors are characterized by a photocurrent response that's linear with incident radiation over a wide range. Any variation in responsivity with incident radiation represents a variation in the linearity of the detector. In effect, we're saying that, if we plot the output current of the detector versus the input radiation level, the slope of the line from the lowest level of radiation to the highest level of radiation shouldn't change. Noise in the detector or system will determine the lowest level of incident radiation detectable. The upper limit of this input/output linearity characteristic is established by the maximum current capability that the detector can handle without becoming saturated (no change in output for a change in input). Linearity may be stated in terms of maximum percent deviation from a straight line over a range of input radiation levels. For example, it can be given as follows: Maximum deviation from a straight line over the range of 10^{-12} watts/cm2 to 10^{-4} watts/cm2 incident on the surface of the detector is less than 5%, or linearity is better than 5% over eight decades of illumination.

Many factors may contribute to the deviations in linearity. Radiation levels in excess of the manufacturer's stated maximum level may cause irreversible damage to the detector surface. In many cases, saturation of the detector response can occur at high light levels. A rating usually is given for the maximum allowable continuous radiation level for a given detector. If the radiation is in the form of a very short pulse, it's possible to exceed the continuous level by a factor of ten or more without damage or noticeable changes in linearity.

4.3.2.7   Response Time

If a constant source of radiant energy is instantaneously turned on and irradiates a photodetector, it will take a finite time for current to appear at the output of the device and for the current to reach a steady-state value. If the same source is now instantaneously turned off, it will again take a finite time for the current to follow the change and decay back to its initial zero level. The term "*response time*" normally refers to the time it takes the photocurrent generated by the detector to rise to a value that's 63.2% of the final or steady-state value reached after a prolonged period of time. The "*recovery time*" is the time it takes the photocurrent to fall from its steady-state value to a value that is 36.8% of the steady-state value.

Photodetectors are apt to be used for detection of fast pulses. So, a more important term, called "*rise time*," is used to describe the speed of response of the detector. Rise time is the time difference between the 10% point and the 90% point of the peak amplitude output on the leading edge of the pulse. "Fall time" is measured between the 90% point and the 10% point of the trailing edge of the pulse waveform. This sometimes is referred to as the decay time.

The time measured between the first appearance of current and the appearance of radiation incident on the surface of the detector is called the "*delay time*." This time may be insignificant compared to the rise time. The time measured between the extinction of radiation incident on the detector and the first indication of a change in the current output is the "storage time." Adding the storage time to the fall time gives what is called the "turn-off time."

Rise-time and fall time are the most significant of these pulse response times. These are the two terms most often quoted by manufacturers in their literature. The rise time of a device that transmits or displays waveforms is taken as the rise time of the output (or displayed) waveform if the device were driven with a theoretically perfect step function (zero rise time). In practice, we use a source whose rise time is much less than the rise time of the device under tests. Ideally, we'd like to have a source with a rise time less than or equal to 1/10 of the rise time of the detector being tested. Another factor to consider is the rise-time limitation introduced by cables or of the display device, for example, the oscilloscope or recorder. As an example, if we fed a perfect step function into a detector and then an oscilloscope, we could determine the output rise time by the following empirical equation:

$$t_t = \left(t_d^2 + t_s^2\right)^{1/2} \tag{4.6}$$

t_t = Rise time of combination of devices.

where:

t_d = Rise time of photodetector.

t_s = Rise time of display device (oscilloscope) and cables.

4.3   Infra-red radiometry

A radiometer (Desvignes, 1987) is the instrument necessary for measurements. In a very general way, a radiometer comprises three parts indicated in Figure 4.3
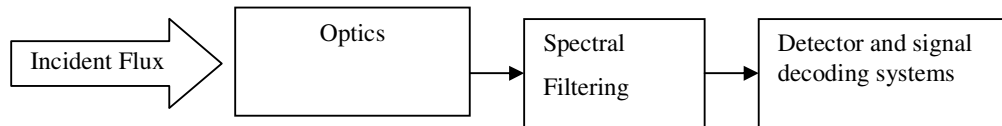 :

Figure 4.3 General diagram of a radiometer operation

Is possible to distinguishes in particular two types of radiometers:
- with fixed aiming, determined by the Field of View (FOV)
- imaging, for whom the instantaneous Field of View (IFOV) samples (1D or 2D) the total Field of View (FOV).

It is shown easily that the signal delivered by a radiometer is written:

$$Signal = C \ L^{sensor} \left[A_P \ \Omega_{IFOV} \right] \qquad\qquad (4.7)$$

where Ap is the surface of the pupil of entry of the instrument, Ω_{IFOV} the solid angle associated with the IFOV, C a coefficient of conversion of the electromagnetic power at the entry of the sensor into electric signal, these three factors being instrumental factors. The signal is thus proportional to the radiance of the defined target as the spot of analysis delimited by the IFOV. Radiance is supposed to be uniform here on the target. If the radiance is not uniform on the sensor (important FOV), the expression above must be integrated with angular and space co-ordinates.

4.3.1   *Spectral filtering*

Spectral filtering is an essential element of a radiometer. There still, one distinguishes:

- radiometer with single spectral band
- radiometer having several distinct spectral bands
- spectro-radiometer having the capacity to measure continuously on a certain spectral interval thanks to a device of sampling or continuously variable selection.

Only instruments either with fixed field, or imagers 2D, with band spectral discrete were used in this work. The spectral band-width of the instrument is then defined by its function filters noted f_λ.

If is $L_\lambda(\theta,\varphi)$ the radiance emanating from the target delimited by the IFOV, the radiance perceived by the sensor is given by:

$$L^{sensor}(\theta,\varphi) = \int L_\lambda^{t\,\arg et}(\theta,\varphi) f_\lambda d\lambda \qquad\qquad (4.8)$$

4.3.2   Brightness temperature

In the infra-red, as one saw, the radiance of target is always the sum of several terms. In all cases one can quantitatively compare radiance measured to the radiance which would emanate from a black body of suitable temperature T_B:

$$L^{sensor}(\theta, \varphi) = \int L_\lambda^0(T_B) f_\lambda d\lambda \qquad (4.9)$$

T_B is the brightness temperature, which is not a true temperature but a parameter depend on the direction and filter function provided by the manufacturer of the instrument. T_B is also called black body equivalent temperature.

.

4.3.3   *Handling of the measured radiometric quantities.*

The signal provided by a radiometer is generally expressed in brightness temperature. This information is not sufficient for the exploitation of measurements and in particular for the inversion of the radiometric equation of radiance entry in the sensor. It is necessary to have expressions give us the possibility to connect brightness temperature to the radiance seen by the sensor, and in addition, at the same time the inverse operation, from the radiance measurement to the brightness temperature. This implies the knowledge of the instrument filter function which balances the spectral distribution of the received radiation of the target. In order to make this relation independent from the amplitude of the filter function and to take into account only spectral weighting, by applying the theorem of the average, we have:

:

$$L^{sensor}(\theta, \varphi) = \int L^0_\lambda(T_B) f_\lambda d\lambda = L^0_{\lambda_c}(T_B) \Delta\lambda, \qquad \Delta\lambda = \int f_\lambda d\lambda \qquad (4.10)$$

It is possible to define the *equivalent spectral radiance* $L^0_{\lambda_c}(T_B)$ [W m^{-2} sr^{-1} µm^{-1}]:

$$L^0_{\lambda_c}(T_B) = \int L^0_\lambda(T_B) \bar{f}_\lambda d\lambda, \qquad \bar{f}_\lambda = f_\lambda / \Delta\lambda \qquad (4.11)$$

where $\bar{f}_\lambda$ is the normalized filter function.

The concept of equivalent spectral radiance makes it possible to establish a quantitative relation between the integrated radiance measured by the instrument, represented by T_B and, by means of the Planck's function, the "central" wavelength λ_c (T_B).

From there, several possibilities arise in practice:

- to represent numerically the relation $\lambda_c(T_B)$ by adjustment with a function λ (polynomials) for a given range of temperatures,
- to use a mathematic function to numerically represent the value of equivalent spectral radiance in an interval of temperature. Two forms of function are often used: exponential or law of power.

For the later needs for this work, the mathematical relations representing the variation of equivalent spectral radiance are developed below on the interval of temperature [280 K - 350

K]. The parameters are given with the number of significant figures necessary not to introduce an error being added to skew resulting from the mathematical form of the approximation.

- representation with a central wavelength

Radiance is calculated starting from the temperature and the wavelength by the Planck's law:

$$L_{\lambda_c}^0(T) = \frac{c_1}{\lambda_c^5} \frac{1}{[\exp(c_2/\lambda_c T) - 1]} \tag{4.12}$$

The law of variation in the length of central wave according to the temperature is represented by a polynomial of fourth degree:

$$\lambda_c = a_4 \, T^4 + a_3 \, T^3 + a_2 \, T^2 + a_1 \, T + a_0 \tag{4.13}$$

This representation of radiance is very sensitive in term of precision to the numbers of significant figures, which justifies knowing the coefficients of the polynomial with 10 significant figures. The coefficient of correlation of the law determined for each sensor is 1,00.

- exponential approximation with two parameters (Pietras, 1996) :

$$L_{\lambda_c}^0(T) \cong a \, . \, e^{-b/T} \tag{4.14}$$

The parameters are given with the number of significant figures required to avoid the introduction of a skew.

- approximation by a power law (Slater, 1980):

$$L_{\lambda_c}^0(T) \cong \alpha \, T^n \tag{4.15}$$

If the interval of temperature can be taken rather small, the coefficients α and n are then appreciably independent from temperature, which makes the relation above operational

4.4 Laboratory calibration sessions

4.4.1 The measures

The laboratory calibration was carried out at "*Laboratoire des Sciences de l'Image, de l 'Informatique et de la Télédétection* (LSIIT) "of "*Louis Pasteur*" university in Strasbourg, where a MIKRON M345 (fig 4.5) Black body source is available (see tab 4.1 for the specification).

As we told in the precedent section, to detect the brightness temperature of a given target is necessary to refer the camera output to a known source of radiation at a certain temperature, which is by a black body source. Since the behaviour of the microbolmeter is linear with the radiance, the first step is to find the linear relation between the radiance incoming at the sensor and the digital counts of the Focal Plane Array, and then to calculate the brightness temperature from both the plank's law and the sensor filter function.

The calibrations performed were at two different temperatures: the first one was the *outdoor* calibration and was at the ambient temperature of 4°C (see fig 4.9 left), the second one was the *indoor* calibration at an ambient temperature of 20°C (see fig 4.9 right). The temperatures were dictated by the two ambient temperatures available, that is the ambient temperature of the laboratory and the outside temperature.

Generally the SkyArrow remote sensing campaigns are made at 2200m (7000ft) above ground level, since the vertical gradient temperature, with stable atmospheric conditions, is of about 0,0065 ^{o}C m^{-1}, in the summer time (i.e. in August) at our latitudes the ground temperature generally changes between 25 and 30°C, hence at flight level probably there is a temperature that changes between 11 and 16°C; in the winter time, instead, the ground temperatures changes between 10 and 20°C, then, at flight level in stable atmospheric conditions, the temperature changes between 0 and 7°C. Those are two boundary cases where the camera should operate, for that we could expect a realistic description of the behaviour of the sensor calibrating it at the two temperatures that we have in and outside the laboratory.

The black body source temperature range is of 0-180°C, the indoor calibration was performed between 4-110°C, the outdoor calibration instead was performed setting the black body source at temperatures from -10°C to 94°C, since is possible to set the black body source at 10 degree less the ambient temperature

The characteristics of the two calibration sessions are reported in table below:

OUTDOOR CALIBRATION	INDOOR CALIBRATION
Ambient Temperature: 4°C	Ambient Temperature: 20°C
Temperature range: -11/94 °C	Temperature range: 10/120 °C
Temperature step: 2°C	Temperature step: 2°C
Distance: 30 cm	Distance: 30 cm
Focus: ∞	Focus: ∞
Camera temperature range firmware: - -40/120 °C - 0/500 °C	Camera temperature range firmware: - -40/120 °C - 0/500 °C

Tab4.1: Calibration sessions characteristics

Since the ranges of temperatures of the black body during the two calibration sessions are different, we operate on the intersection between them, which is between 10 and 94°C.

Due to the fact that the common remote sensing campaign are made on Mediterranean forest and agricultural ecosystems, where is possible to assume that the maximum temperature is up to 50°C, we have separated the range of calibration in two subset.

We have processed the data so to have the following calibration curve:

1. calibration curve for target temperature between 10 and 50°C
2. calibration curve for target temperature between 50 and 94°C

In this way is possible to improve to accuracy of the sensor, applying the one or another curve regards both to the target observed and the atmospheric conditions.

As is possible so see from the table above we have placed the camera at 30 cm in both the calibration session, that is the min-focus distance of the camera, also we have set the focus of the camera to ∞, that is the value that is used during in-flight acquisition.

Figures 4.6 show the camera both inside and outside the laboratory during the calibration acquisitions, and figures 4.7 and 4.8 show two example of data acquired; figure 4.7 on the left shows the thermal image of the black body, on the right, instead, is possible to see the central part of the image (up) and the relative Gaussian distribution of the temperature centred on 16°C (down).

The same on figure 4.8 for the outdoor acquisition.

Fig4.5: MIKRON M345 and FLIRA40M

BLACK BODY SOURCE
Temperature range: 0-180°C
Accuracy thermometric: ± 0.2°C
Temperature resolution: 0.01°C
Stability: 0.1°C for 8h
Source Non-Uniformity: ± 0.2°C
Aperture diameter: 4"x 4"
Emissivity: 0.97

Tab 4.2: Black Body source specifications

THERMAL CAMERA
Field of view: 45°, IFOV: 1.3 mrad
Detector Type: Focal Plane Array (FPA),
uncooled microbolometer 320 × 240 pixels
Spectral range: 7.5–13 μm
Temperature range, standard:
-40–+120 °C or 0 – 500°C
Accuracy: ± 2 °C or ± 2 % of reading.
The specification is valid when the ambient
Temperature is between +5 °C and +45 °C.

Tab 4.3: Thermal camera specifications

*Fig4.6: The two calibration sessions, the outdoor calibration at 4 degree Celsius (left),
and the indoor calibration at 20 degree Celsius (right)*
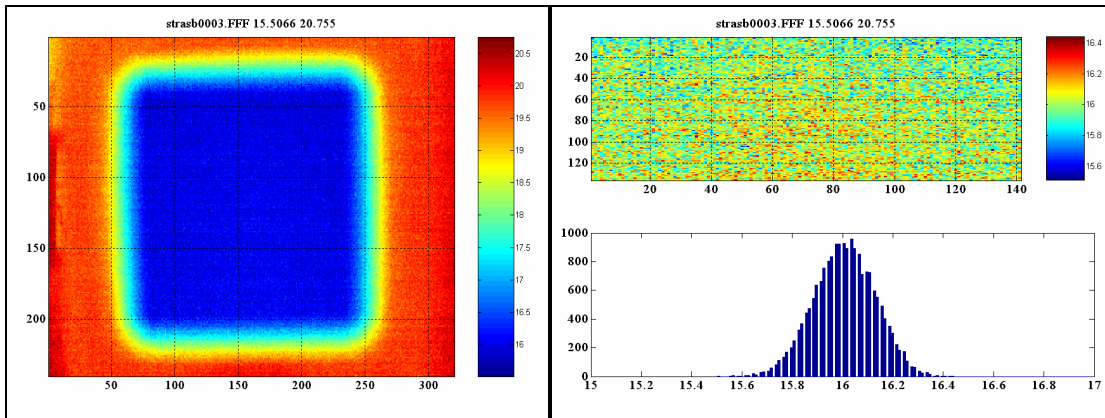
*Fig4.7: Thermal image with Black body temperature at 16°C and the ambient temperature at 20°C, during
indoor acquisition*
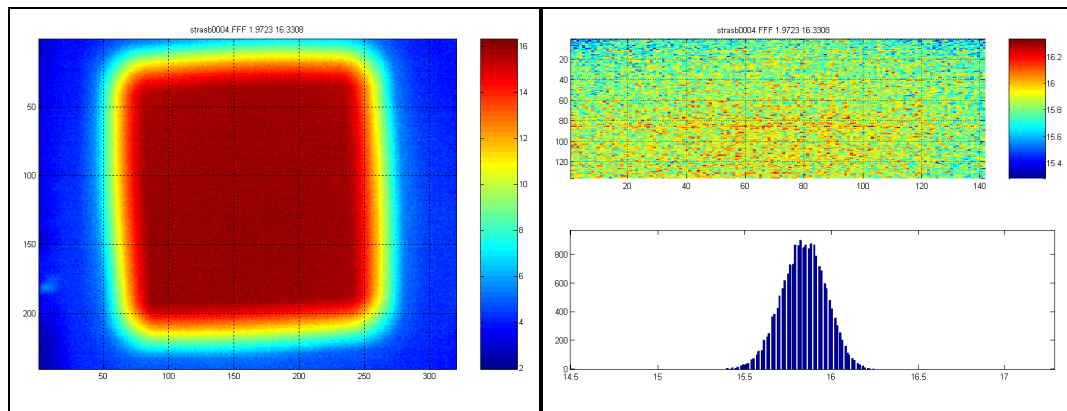
*Fig4.8: Thermal image with Black body temperature at 16°C and the ambient temperature at 4°C, during
outdoor acquisition*

4.4.2 The results

To find the relation between the radiance and the temperature we have used the "power law" approach (equation 4.12).

From the equation 4.10 and 4.15 we can state that:

$$L^{sensor}(\theta, \varphi) = \int L_\lambda^0(T_B) f_\lambda d\lambda \cong \alpha T^n \qquad (4.16)$$

Applying the logarithms at both the members of the equations we have:

$$\ln(L^{sensor}) = \ln(\alpha) + n \times Ln(T) \qquad (4.17)$$

For each black body temperature, we calculate the "*equivalent spectral radiance*" by means of the plank's law, then we obtain the two coefficients *ln(α)* and *n* applying linear regression at the equation (4.17) (Fig 4.9).

The fitting precision on the derived temperature is better than the 0.02% in the temperature range 10-50°C, figure 4.10 shows the residual between the actual temperature of the black body source and the temperature derived by means of the equation 4.11.
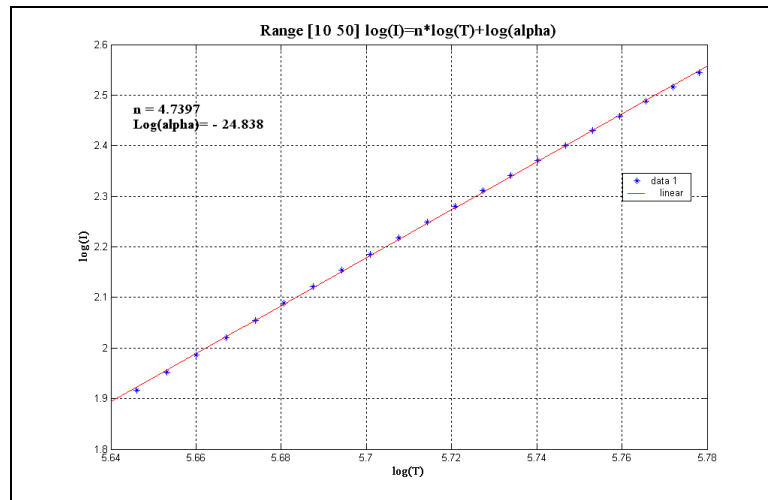
Fig4.9. the regression of the equation (4.17), on the range of temperature

from 10 to 50 degree Celsius
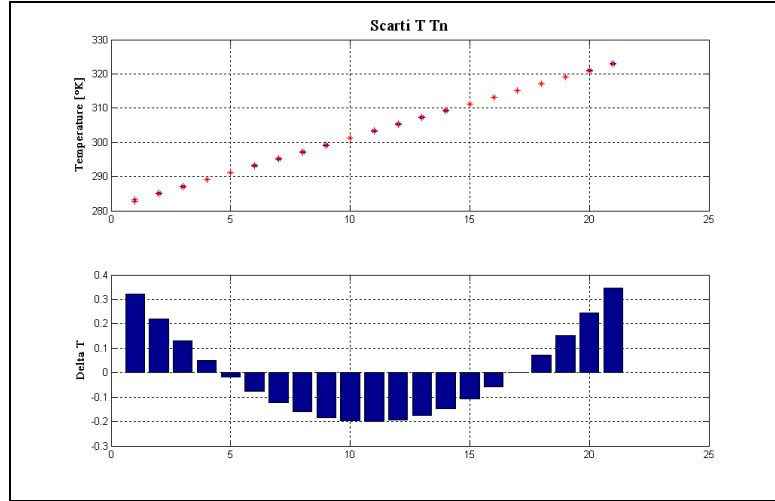
Fig4.10. the residuals between the actual temperature of the blackbody
and the temperature derived by means of the relation (4.17).

The calibration curves for the outdoor and indoor between radiances and digital counts are given by the following:

$$L_{10-50out} \approx 0.0018507 \times DN - 7.9808 \tag{4.18}$$

$$L_{10-50in} \approx 0.0018603 \times DN - 7.9812 \tag{4.19}$$

The relation between radiances and the brightness temperatures is obtained from the equation (4.14):

$$T_{10-50out} \approx \exp\left(\frac{\ln(L_{10-50out}) - \ln(\alpha)}{n} \right) \tag{4.20}$$

$$T_{10-50in} \approx \exp\left(\frac{\ln(L_{10-50in}) - \ln(\alpha)}{n} \right) \tag{4.21}$$

Where the coefficient used are the those relatives at the range 10-50°C and at the range 50-94°C are reported in the table below:

RANGE	n	$\ln(\alpha)$
10 – 50 °C	4.7397	-24.838
50 – 94 °C	4.2660	-22.101

Tab 4.4: regression coefficient

The relevant quantity for calibration of the camera is the difference in digital counts between the output signal delivered by the sensor viewing successively the black body at temperature T_B and at ambient temperature T_a:

$$S = \frac{c(T_B) - c(T_a)}{L(T_B) - L(T_a)} \qquad (4.22)$$

Where S is the radiometric sensitivity of the sensor at that ambient temperature (figure 4.11).
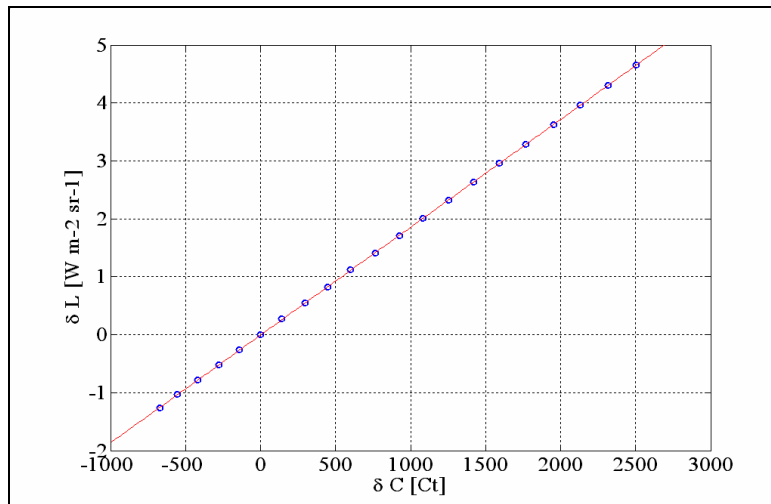
Fig4.11: The sensitivity of the camera, the difference in radiance

Vs the difference in digital counts
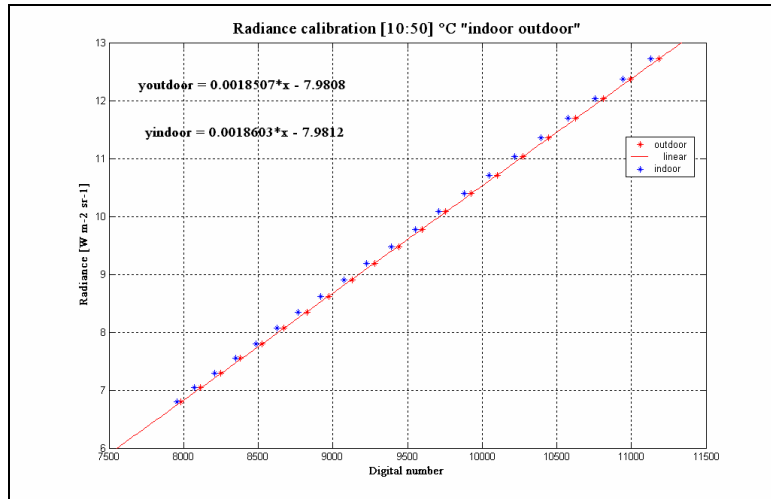
Fig4.12: The two calibration curves Radiance Vs Digital Counts

(outdoor/indoor) for the range 10-50°C
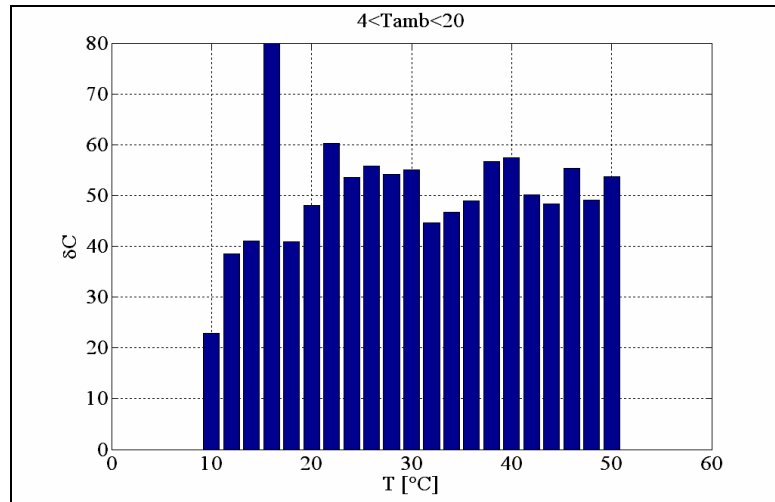
Fig4.13: Differences in digital counts between respects at the two ambient temperatures

for the range 10-50°C

4.4.2.1   Output signal noise

For each temperature were made ten acquisitions at frame rate of 1Hz, this is done to evaluate the output signal noise of the sensor during a long enough time. The fluctuations measurements of the output signal allowed to determine a standard deviation σ_c in terms of counts. Figure 4.14 show the digital counts standard deviation for the entire range of measurements and for both the acquisition sessions. It is possible to note a more stable behaviour of the sensor at the ambient temperature of 20°C.
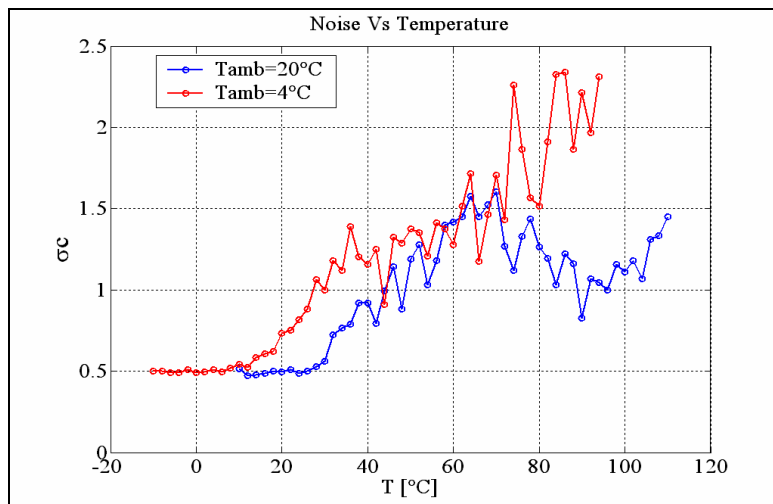
Fig4.14: The standard deviation of the digital counts on
10 images for each black body temperatures

For the sensor is then possible to derive the Noise Equivalent Delta Temperature (NEDT) from the equation below:

$$NEDT = \frac{\sigma_c}{S \times \dfrac{dL}{dT}} \qquad (4.23)$$

Figure 4.15 and 4.16 show it for the two ranges [10 50] and [50 94]°C.
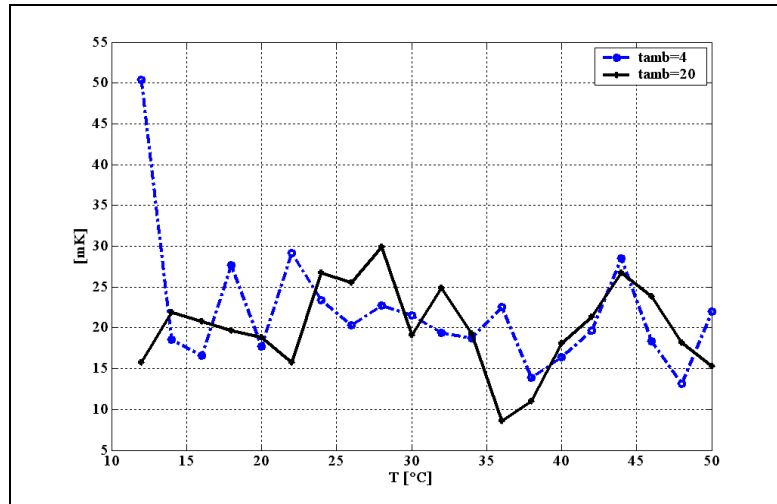
Fig4.15:The Noise Equivalent Delta Temperature on the range 10 – 50°C at two ambient temperatures
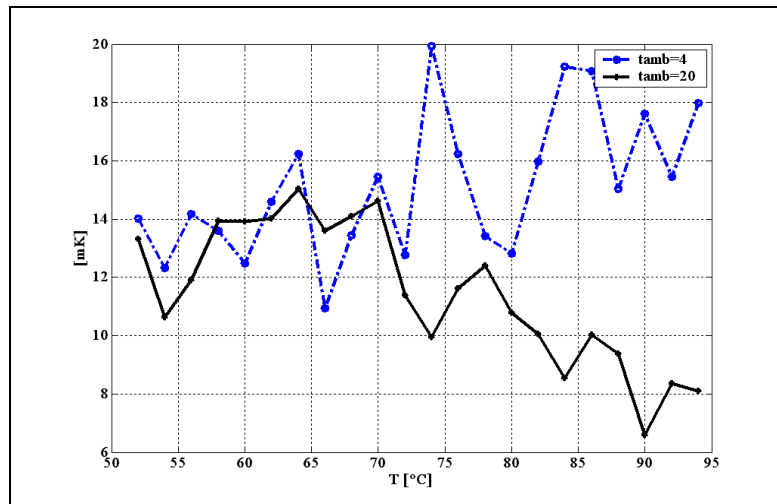
Fig4.16:The Noise Equivalent Delta Temperature on the range 50 – 94°C at two ambient temperatures

Applying the calibration curve found on the data set acquired at the ambient temperature of 20°C, from the figure 4.17 is possible to see the deviation from the black body temperature (blue bars), the standard deviation in the range [10 50] at T_{amb} = 20°C is of 0.0075. Applying the same calibration curve at the dataset acquired at T_{amb} = 4°C we have a standard deviation of 0.6125
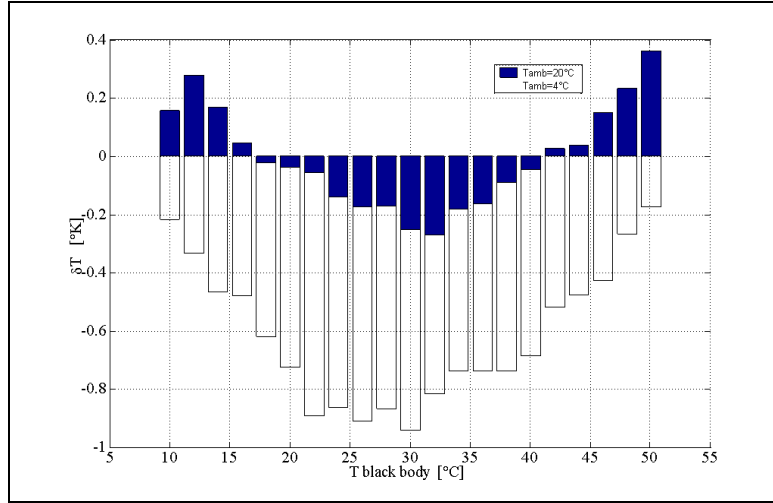
Fig4.17:The deviation from the black body temperature applying the calibration curve
at different ambient temperatures

4.4.2.2 Error analysis

We estimate the absolute uncertainty ΔT on the determination of the brightness temperature
T of a target by using Eq. (4.20). Three kinds of uncertainties are identified:

1. ΔT^c due to the uncertainty in numerical output counts, associated with detector and electronic noise and digitizing of the output voltage;
2. ΔT^p due to the uncertainty in the temperatures given by black body source;
3. ΔT^s due to the uncertainty in the sensitivity obtained from calibration, as shown in figure (4.10) .
4. ΔT^T due to the change in response of the camera related at changes in ambient temperature as shown in figure 4.17.

As a first approximation, by considering these various sources of uncertainty as independent, we estimate the total uncertainty.

$$\Delta T = \sqrt{\left(\Delta T^c\right)^2 + \left(\Delta T^p\right)^2 + \left(\Delta T^s\right)^2 \left(\Delta T^T\right)^2}$$

(4.24)

The global uncertainty applying the calibration curve over the range [10 50] °C by means of
the equation 4.24 is less than ±1°C considering ambient temperatures from 4 to 20°C.

Flight comparison

During the "Carboeurope Regional Experiment" hold in south west France in June 2005, was performed a flight comparison between the thermo-camera FLIR A40M and the EVERST interscience 4000, mod 400-4zl, also calibrated at LSSIT laboratory (Figure 4.18).
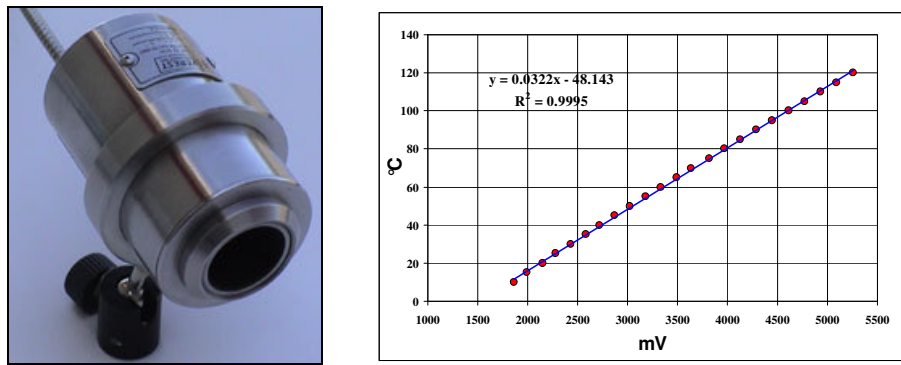

Fig4.18: The Everest Radiomete and it's calibration curve

The comparison was performed over the forest transect, that is the blue transect in figure 4.19 (north – south).

The FLIR A40M flew on board the first SkyArrow at an mean high of 2200m above ground level. The Everest radiometer instead flew onboard the second SkyArrow at a mean high of 100m during carbon dioxide, water vapour and heat fluxes measurement.
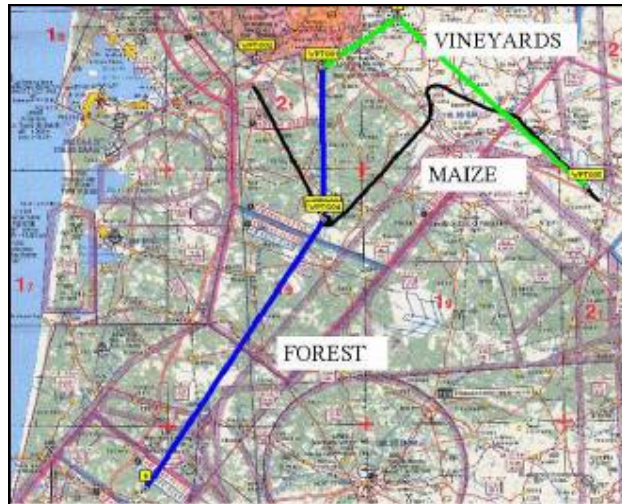
Fig4.19: Planning for the Carboeurope Regional Intensive Campaign over Les Landes

Coupled with the thermo-camera there was the composite infrared camera Duncantech MS4100, that provided images in three spectral range from the visible to the near infrared.

The along track swath of the radiometer was of 7m, instead the swath of the camera was of about 2000m, to compare the two data sets, we have done the average of each thermal image and the average of the radiometer data over the area covered by each image, Figure 4.20 shows the result.
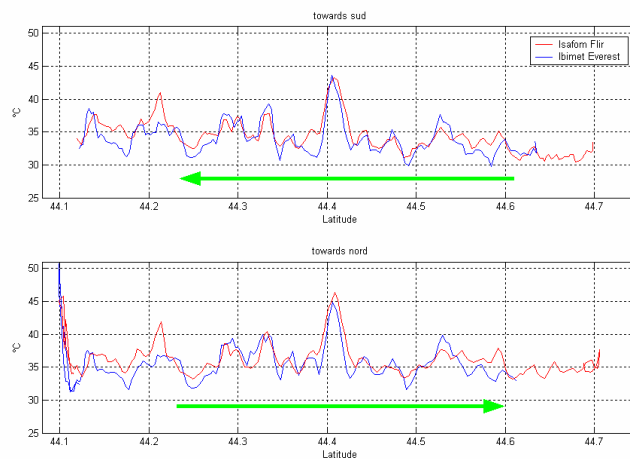
Fig4.20: Comparison between the moving average temperatures by the thermocamera
and the Everest radiometer

Figure 4.21 shows instead the comparison over a specific field highlighted in the thermal image below. The difference of the measured temperature is always below one degree.
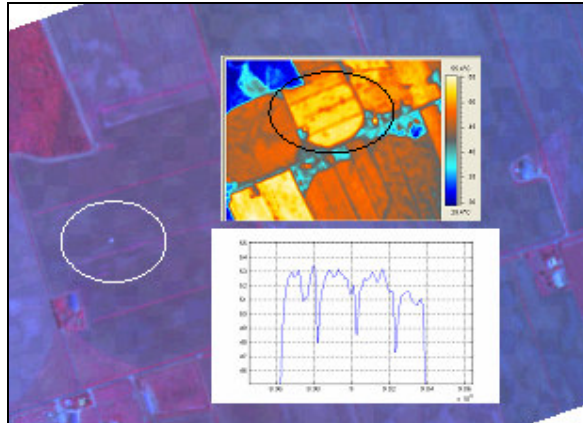
Fig4.21: Comparison between the thermocamera
and the Everest radiometer

PART II: IN-SITU MEASUREMENTS

AIRBORNE WIND CALCULATION

5.1 Introduction

The air-motion sensing technique used to calculate the three dimensional wind vector, in the earth centred coordinate system, starting from airborne measurements, from SkyArrow airborne data is described for measurement of the three dimensional wind vector

The use of research aircraft to measure atmospheric motions, from mean horizontal winds to turbulent eddies, has improved greatly on the last few decades.

Measurements techniques are evolved along two lines:

1. use of aircraft's response to wind

2. the installation of a variety of velocity sensors on the tips of long nose booms ahead of the aircraft.

Aircraft response technique are presented by Lenshow (1976) and Lawson (1979).

The system used in this work use the second approach, it consist of a boom installed in front of the fuselage of the aircraft. Here we present the technique developed by Brown (Brown et al 1983) first. It is based on the measurement of the surface pressure distribution on the nose of the aircraft itself, from which, by suitable calibrations, the angles of attack and sideslip, and the dynamic pressure are obtained.

Here we define the angle of attack and sideslip as the flow angles of the air with respect to the longitudinal axis of the airplane in the vertical and lateral directions (with respect to the airplane axis), respectively. These angles and the true air speed, which is calculated from the dynamic pressure, air temperature and static pressure, define the velocity vector relative to the aircraft (Ekman, 1999). Combining this data with data on the aircraft motion with respect to the earth (as measured by the 4-antenna attitude GPS receiver), we can calculate the wind vector with respect to the earth (Lenschow 1972).

5.2 The wind calculation chain

The three-dimensional wind vector is computed by taking the vector sum of the aircraft relative air velocity and the ground-relative aircraft velocity.

$$\overline{V} = \overline{V_p} + \left[\overline{\overline{M}}\right] \times \overline{V_a'} \qquad (5.1)$$

Figure 5.1 shows the block diagram for the airborne wind calculation chain.
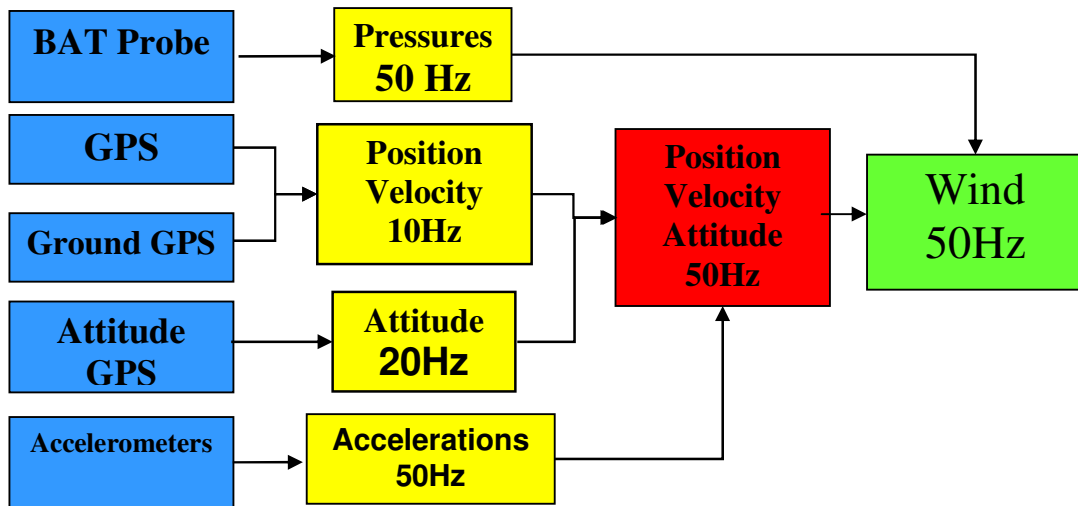
Fig 5.1: wind calculation block diagram

The diagram, from the left to the right, shows the sensors used (blue boxes), the data collected and the frequency of acquisition (yellow boxes), which of them are merged to obtain congruent frequencies (red box), to obtain the three dimensional wind vector in the earth centred inertial reference frame (green box).

The motion of the aircraft is composed by the motion of the centre of gravity of the aircraft, as it is a material point, and the motion of the aircraft around the centre of gravity, as it is a rigid body.

The position and velocity of the probe is given by the GPS Novatel antenna that is mounted on the nose of the aircraft, they are collected at the frequency of 10Hz. The motion of the aircraft around the centre of gravity is described by the three Eulerian's angles, that are

provided by the 4-antenna GPS Javad, calculated by the master receiver by means of the relative position measured by the slave receivers.

These data are enough to calculate the motion of the sphere in respect to the ground and to construct the rotation matrix from the system . To calculate the motion of the sphere to respect the air we start from the pressure measurements provided by the sphere itself, and then, adding these two motion we obtain the three dimensional wind vector.

To better explain the algorithm used, we divide the procedure in the following steps:

1. Flow angles calculation

2. True air speed calculation

3. Development of rotation matrix $\overline{\overline{M}}$ to rotate vectors from "*Body Reference Frame*" to "*Inertial Reference Frame*".

4: Ground speed calculation

5. Wind calculation (**V**) in the earth reference.

6. Optimization of wind calculation.

5.2.1   *Flow angles*

The use of pressure distribution around a fixed body of revolution to measure incident flow angles has been known for some time.

Probes for this purpose were apparently first developed by van der Hegge-Zijen (Eckert, 1938).

In High number of Reynolds number flow past a sphere, the pressure distribution for potential flow is:

$$P_\gamma - P_s = \frac{1}{2}\rho U^2 \left(1 - \frac{9}{4}\sin^2\gamma\right)\qquad(5.2)$$

where $q = \frac{1}{2}\rho U^2$ is the dynamic pressure, p_s is the static pressure, and p_γ is the pressure at an angle γ from the flow stagnation point on the sphere. (γ is the angular separation as measured from the pressure sphere's center.- see figure 5.2).

The probe is designed so that on average the stagnation point of the flow will be at port 0 (Fig. 3), but this point will move over the face of the probe as a result of variations in the relative wind vector $\mathbf{V_a}$.
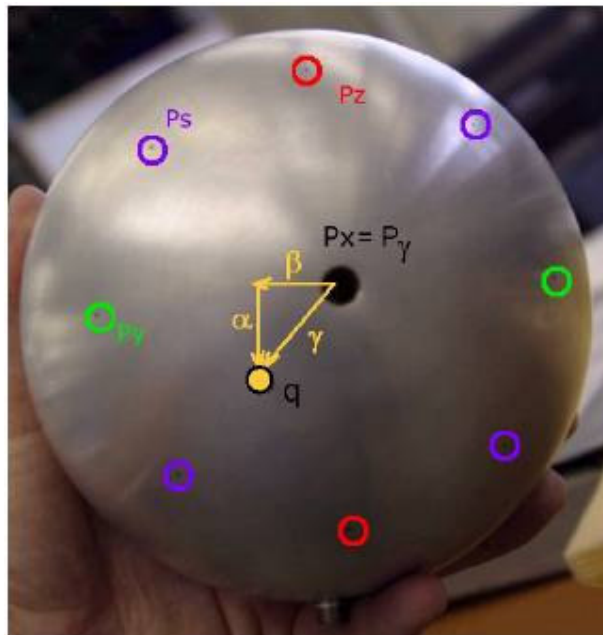
Fig 5.2:The pressure sphere: highlighted the nine holes for static, total and differential pressure measurements

At any given time, the relative wind vector will form an angle with the probe x axis, as shown in figure 5.3. The relative wind can have both an angle of attack α in the x-z plane (similar to latitude on the earth) and angle of sideslip β in the x-y plane (similar to longitude). Nonzero values of these angles will directly lead to displacements of the flow stagnation point away from port 0.
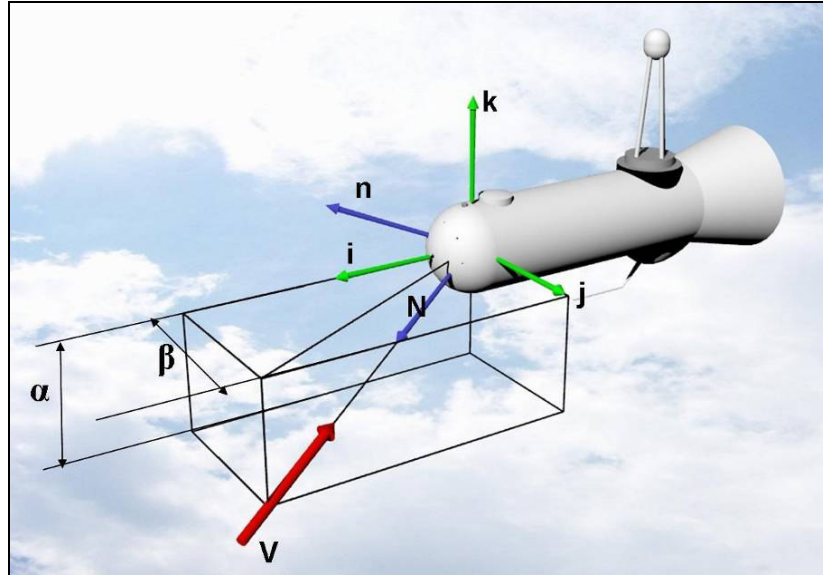

Fig 5.3:The scheme shows how the flow angle are described in the sensor reference

The equation 5.2 can be rewritten as:

$$P(n) = P_s + \frac{q}{4}\left[9(N \cdot n)^2 - 5\right]$$ (5.3)

Where:

$$N = \frac{1}{D}i - \frac{\tan \beta}{D}j - \frac{\tan \alpha}{D}k$$ (5.4)

$$D = \sqrt{1 + \tan^2 \alpha + \tan^2 \beta}$$ (5.5)

N is a unit direction vector (Leise and Master, 1991) that is normal to the sphere's surface at the stagnation point, and n is the normal direction vector at some chosen point on the sphere.

Assumed that the right-left and top-bottom ports are located at an angle ϕ away from the central port, equation 5.3 gives us the relation between the delta pressure and the flow angles as:

$$\delta P_y = 9q \frac{\sin\phi\cos\phi}{D^2} \tan\beta \tag{5.6}$$

$$\delta P_z = 9q \frac{\sin\phi\cos\phi}{D^2} \tan\alpha \tag{5.7}$$

To calculate the dynamic pressure as the difference between the total pressure and the static pressure (Bernoulli equation), first we have to define exactly the "*static pressure*" from the "*reference pressure*" measured as the average on the four holes (purple holes in figure 5.2) on the sphere. Assuming that the static pressure holes are located at an angle ϕ_r:

$$p_r = p_s + \frac{q}{4}\left[9 \frac{\cos^2\phi_r + 0.5\left(\tan^2\alpha + \tan^2\beta\right)\sin^2\phi_r}{D^2} - 5\right] \tag{5.8}$$

Then the appropriate equation to measure $\delta p_x = p_0 - p_r$ is:

$$\delta P_x = \frac{9q}{8D^2} \sin^2\phi_r \left[3 - D^2\right] \tag{5.9}$$

Equations 5.6, 5.7 and 5.9 form a closed system of equation that can be solved for the unknowns α β and q. To solve this system of equations, it is useful to define the ratios below, that for $\phi = \phi_r$ we have:

$$H_\alpha = \frac{2}{9} \frac{\delta\hat{P}_z}{\delta\hat{P}_x} \tag{5.10}$$

$$H_\beta = \frac{2}{9} \frac{\delta\hat{P}_y}{\delta\hat{P}_x} \tag{5.11}$$

The flow angles can be obtained as:

$$\tan\alpha = 4H_\alpha\left[1+\sqrt{1+8\left(H_\alpha^2+H_\beta^2\right)}\right]^{-1} \qquad (5.12)$$

$$\tan\beta = 4H_\beta\left[1+\sqrt{1+8\left(H_\alpha^2+H_\beta^2\right)}\right]^{-1} \qquad (5.13)$$

And the dynamic pressure as:

$$q = \frac{8}{9}\frac{\delta p_x}{\sin^2\phi_r}\frac{1+\tan^2\alpha+\tan^2\beta}{1-\tan^2\alpha-\tan^2\beta} \qquad (5.14)$$

5.2.2 *True air speed*

When combined with a temperature measurement T (which can be either the probe or hatch temperature), the computed values of α, β, and q provide the information required to estimate the True Air Speed V_a. The temperature must first be corrected for adiabatic heating resulting from the aircraft motion. The corrected temperature T' is related to the measured temperature T through the equation (Lenschow 1986; Leise and Masters 1991):

$$T' = T\left(1 + r\frac{\gamma - 1}{2}M^2\right)^{-1} \tag{5.14}$$

Where $\gamma = C_{pm}/C_{vm}$, with C_{pm} the the specific heat at constant pressure for moist air, and C_{vm} the specific heat at constant volume for moist air, M is the Mach number, r is an empirical temperature recovery factor for the probe.

Defining the Mach number as:

$$M^2 = \frac{2}{\gamma - 1}\left[\left(1 + \frac{q}{p_s}\right)^{\frac{(\gamma-1)}{\gamma}} - 1\right] \tag{5.15}$$

Since $q \ll p_s$ for the velocity flown by the SkyArrow, expanding the 5.15 in a Taylor series and taking the first term we obtain:

$$M^2 \approx \frac{2}{\gamma}\frac{q}{p_s} \tag{5.16}$$

that can be used for the temperature correction due at the adiabatic heating. The 5.14 can be rewritten as:

$$T' = T\left(1 + r\frac{\gamma - 1}{\gamma}\frac{q}{p_s}\right)^{-1} \tag{5.17}$$

Once the Mach number and the corrected temperature are known the true air speed can be computed as (Lenschow 1986):

$$U_a = M \sqrt{\gamma R_m T'} \tag{5.18}$$

The three components of the relative-wind vector are then obtained from the equations:

$$\hat{u}_a = -\frac{U_a}{\sqrt{1 + \tan^2 \alpha + \tan^2 \beta}} \tag{5.19}$$

$$\hat{v}_a = -\hat{u}_a \tan \beta \tag{5.20}$$

$$\hat{w}_a = -\hat{u}_a \tan \alpha \tag{5.21}$$

The aircraft-relative air velocity is determined by the gust probe system and is rotated into the earth coordinate system using a transformation matrix, $\overline{\overline{M}}$ defined by the aircraft attitude as is showed in the next section.

5.2.3 The rotation matrix $\overline{\overline{M}}$

The collected data and the calculated results will appear in different coordinate systems – each in the most appropriate for the respective use. Accordingly data will have to be transformed from the measurement coordinate system to the final system.

Figure 5. shows the the aircraft coordinate system and the Earth-centered coordinate system, attitude angles, and angles of attack and sideslip.
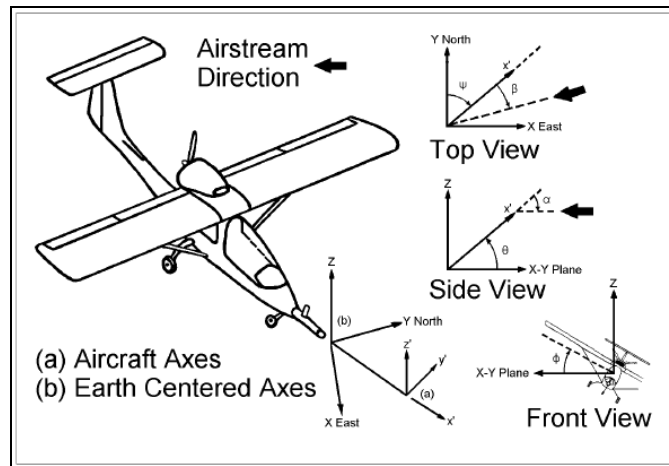

Fig 5.4:Aircraft coordinate system

Figure 5.6 shows the locations of the 4-antenna GPS attitude sensor, and of the two three dimensional set of accelerometers, on the nose of the aircraft and in the back seat in the auxiliary box near the centre of gravity..

Attitude 3D GPS (20 Hz)

accelerometers (50 Hz)
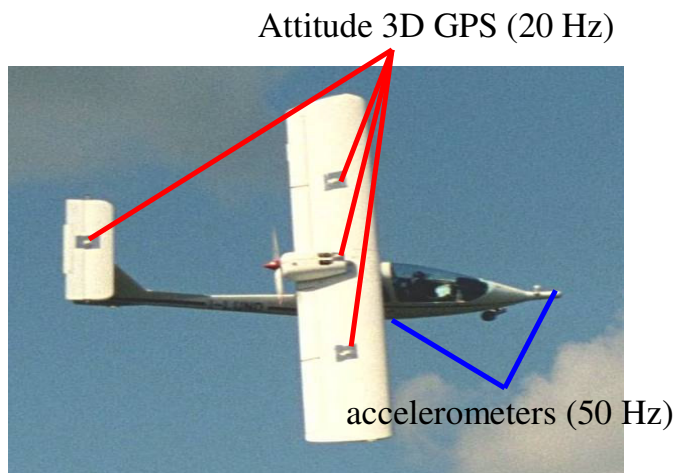
Fig 5.6: Position of the 4-antenna attitude sensor and of the three-dimensional accelerometer

Some of the aircraft sensors, such as the GPS subsystem, provide vector quantities that are oriented in the earth coordinate system (x; y; z). Others, such as the probe sensors, produce vectors in the probe coordinates (x'; y';z'). The relationship between these coordinate systems varies with time and must be measured so that the proper rotations can be applied to vector quantities. Three angles are used to express the relative orientation of the two systems: the roll ϕ, pitch θ, and yaw ψ. Rotations such as these in three dimensions are not commutative, so the three rotations cannot be applied in arbitrary order. In transforming from probe to earth coordinates, the rotations are applied in the order ϕ, θ, and ψ.

The roll angle ϕ represents a rotation about the probe x' axis. The convention used here is that ϕ is zero when the probe y' axis is level with the horizon and the z' axis is pointing up (in case the pilot is collecting measurements while flying inverted). A positive change in the roll angle occurs when the y' axis is rotated clockwise while viewing the probe head-on (i.e., a roll to the left from the pilot's perspective). The pitch angle θ represents a rotation about the probe y' axis (with the qualification that the ϕ rotation must be applied first). Similar to the roll, $\theta = 0$ when the x' axis is level with the horizon. A positive pitch angle is present when the positive x' axis points above the horizon. After the roll and pitch rotations are applied, the yaw angle ψ represents rotation about the z' axis. The yaw angle is zero with the x' axis pointing east and is considered to be positive when measured in a clockwise direction from due east.

As we told the SkyArrow has two sets of three-dimensional accelerometers mounted both on the nose and in the Aux Box, that is close to the centre of gravity of the aircraft. The difference between the two measurements gives information about the attitude of the aircraft.

The acceleration data are collected at the frequency of 50Hz, then they can be used to resample the attitude data from 20Hz to 50Hz, so they will be comparable with the pressures and gases data collected by the others sensors mounted on the airplane.

For example equation 5.22 shows that the difference between the z-axes acceleration measured on the nose, and the z-axes acceleration measured on the centre of gravity divided by the distance between the two sets, is equal to angular acceleration around the y-axes, that is the second derivative of the pitch angle.

$$\frac{\partial \theta^2}{\partial t^2} = \frac{\hat{a}_z - \hat{a}_{bz}}{d} \qquad (5.22)$$

The same information is recovered for the yaw angle by means of the y-axis accelerations (equation 5.23).

$$\frac{\partial \psi^2}{\partial t^2} = -\frac{\hat{a}_y - \hat{a}_{by}}{d} \qquad (5.23)$$

To obtain the attitude angles from the accelerations it is needed to double integrate the quantity at the right side of the equations 5.22 and 5.23. This implies that all the acceleration errors at low frequency will be amplified by the double integrations in the angle results.

To avoid this effect only the high frequency of the accelerometers data will be considered.

Then we can call the high reference provided by the accelerometers $\phi_h, \theta_h, and \psi_h$. The GPS attitude data instead provide the low reference data for the angles, we call them: $\phi_l, \theta_l, and \psi_l$.

However, these integrations become much simpler to carry out after Fourier transformation, because integration in time becomes simple multiplication in frequency.

These signals were blended in frequency space by taking the Fourier transform of all the time series. Using the Fourier transform $\Theta(f)$ of the pitch θ at frequency f as an example, the blending took the form:

$$\Theta(f) = (1 - \eta)\Theta_l(f) + \eta\Theta_h(f) \qquad (5.24)$$

Where $\eta = \eta(f)$ is a weighting function between 0 and 1. Below a speci_ed frequency $f1$, η was set equal to zero. Above another frequency $f2 \ (> f1)$, η was unity. At frequencies f between $f1$ and $f2$, the weighting function took the form:

$$\eta = \frac{\log(f/f_1)}{\log(f_2/f_1)} \qquad (5.25)$$

This filtering is symmetric in that negative frequency are treated the same as positive frequency.

The reason the fillter is allowed to ramp between f_1 and f_2 is to avoid making the cut off the filter too sharp. Usually, these frequencies were de_ned so that they spanned a quarter decade: $\log(f_2/f_1) = 0.25$.

These frequency were chosen to ensure f_2 remained below the Nyquist frequency of the GPS data and also to account for data losses resulting from problems with the data acquisition system.

The use of Fourier transforms in blending the GPS and accelerometer data had another benefit in dealing with the accelerometer data. As shown in Eqs.(5.22) and (5.23), the accelerometers provide the second derivatives of the pitch and yaw angles.

Thus, the integrations in Eqs.(5.22) and (5.23) were performed by first taking the Fourier transform of the right sides, and then multiplying the resulting Fourier coefficients by the filter function.

$$I(f) = \frac{1}{(2\pi f)^2} \tag{5.26}$$

After the filtering and blending described above were completed, the resulting Fourier transforms were inverse transformed to their corresponding angles ϕ, ϑ, and ψ.

These 50Hz blended angles are the ones that are used to rotate vectors from the probe coordinate system to earth coordinates.

The figures 5.5 and 5.6 show the spectrum of the javad angle signal and of the accelerometer data, and of the blended results. In the last part of the spectrum of the accelerometers is present a strong noise, due probably, since the high sensitivity of the accelerometer sensors, at aliasing effect.

Aliasing means that the frequencies that are above the Nyquist frequency appear the same amount that they exceed the Nyquist Frequency, below the Nyquist Frequency in the power spectrum. In the case of the accelerometers the noise source is probably the vibration present inside the aircraft due for the presence of the engine and the blades.

In fact (Porsen, 2005), with a maximum power at 5800 rpm and so an estimated cruising rpm of 5000 and a 2.27:1 reduction gear ratio, the propeller would rotate with about 2000 rpm during most of the flight time. That is a frequency of 33 Hz.. So for a sampling rate of 50 Hz and accordingly a fny of 25 Hz, this vibration would appear 17 Hz in the power spectra.
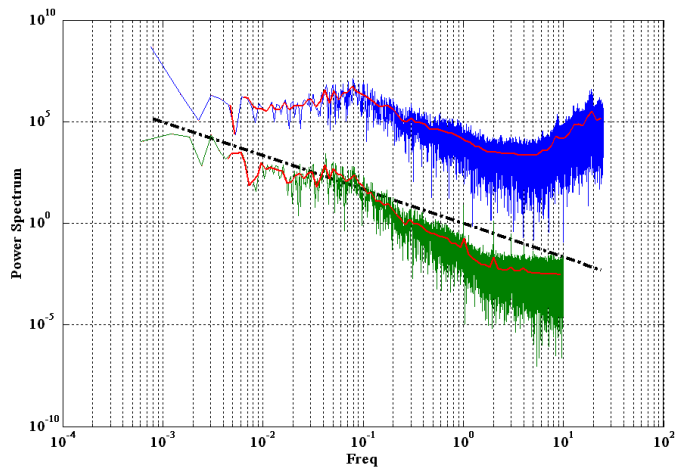
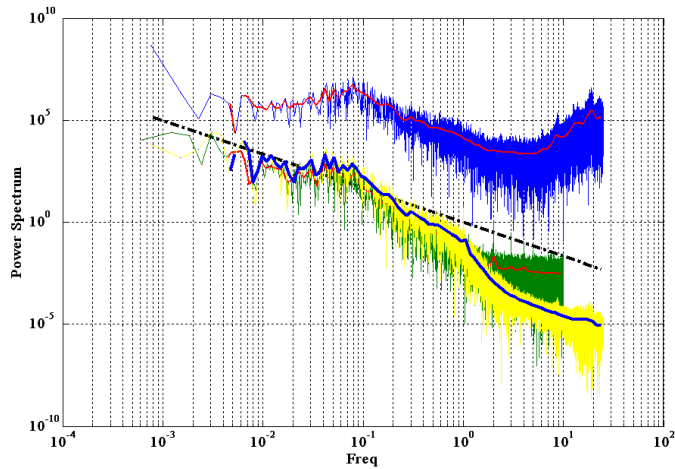*Fig 5.5: The spectrum of the javad signal (green) and of the accelerometer data (blue).*

.

Fig 5.6:The spectrum of the blended signal (yellow line), overlapped at the source signals

Figure 5.7 shows the time series of the pitch angle both before and after the frequency blending operation. It is visible from both the figures 5.6 and 5.7 that the noise is drastically diminished, in fact the power spectrum of the blended signal do not present the increase of noise at high frequency that before the javad spectrum shows. Moreover from figure 5.7 is clear that the blended signal is not affected from the random noise that is visible in the source signal in red.
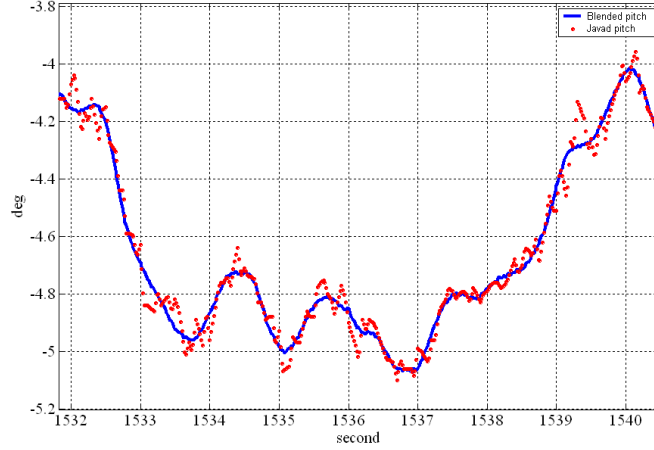
Fig 5.7:The pitch angle time series both before and after the frequency blending. The noise of the javad attitude sensor is filter-out.

At this point is possible to construct the rotation matrix $\overline{\overline{M}}$, as the following relation:

$$\overline{\overline{M}} = \overline{\overline{M}}_h * \left(\overline{\overline{M}}_p * \overline{\overline{M}}_r \right) \tag{5.27}$$

Where:

$$\overline{\overline{M}}_r = \begin{bmatrix} 1 & 0 & 0 \\ 0 & \cos(\phi) & \sin(\phi) \\ 0 & -\sin(\phi) & \cos(\phi) \end{bmatrix} \tag{5.27}$$

$$\overline{\overline{M}}_p = \begin{bmatrix} \cos(\vartheta) & 0 & -\sin(\vartheta) \\ 0 & 1 & 0 \\ \sin(\phi) & 0 & \cos(\phi) \end{bmatrix} \tag{5.27}$$

$$\overline{\overline{M}}_h = \begin{bmatrix} \sin(\psi) & -\cos(\psi) & 0 \\ \cos(\psi) & \sin(\psi) & 0 \\ 0 & 0 & 1 \end{bmatrix} \tag{5.27}$$

5.2.4 Ground speed

The primary source of the probe velocity Vp measurements on the SkyArrow was the GPS subsystem. The GPS provides direct measurements of the probe velocity in a digital form.

Using these data is straightforward except for one problems. The GPS velocities have the same problem as the attitude angles described in the foregoing section, namely that they did not have a fast enough sampling rate to provide Vp measurements up to the desired 50 Hz.

The problem with the GPS data was that the positions and velocities are limited to a 10Hz sampling rate. Additional data are required to fill the gap between the GPS sampling rate and the 50Hz rate required for Vp. This was supplied by the accelerometers on the probe. The raw 50 Hz data coming from the probe accelerometers are the acceleration vector a' = (ax'; ay'; az') in the probe coordinate system. This vector is rotated into the (x; y; z) coordinate system using the roll, pitch, and yaw angles. The resulting rotated acceleration is a = (ax; ay; az).

After rotation of the accelerations, the GPS velocity measurements and the acceleration are blended using an approach very similar to that used with the attitude angles. The GPS platform velocity V_{pg} is assumed to be a low-frequency reference for V_p, and the acceleration is assumed to be a high-frequency reference. Both vectors are Fourier transformed to frequency space. The acceleration is then time integrated by multiplying the Fourier transform A(f) of a by the filter

$$G(f) = \frac{i}{(2\pi f)^2} \qquad (5.25)$$

where i is equal to $\sqrt{-1}$. This integration converts acceleration into a Fourier-transformed velocity Vpa(f). The accelerometer coefficients V_{pa} are then blended with the GPS Fourier coe_cients $V_{pg}(f)$ using the same method as described by Eqs. (5.24) and (5) for the attitude angles. After blending, the resulting Fourier coefficients Vp(f) are inverse Fourier transformed to provide the 50Hz probe velocity V_p.

Chapter 6

WIND CALIBRATION

6.1 Introduction

The presence of the aircraft in the airstream causes input errors to the measuring instruments, hence the aircraft disturbs the air that it flies through, thereby also disturbing the airdata measurements.

Local flow angles also differ from the free-stream flow direction. In straight-and-level flight, the airflow rises to the wing leading edge and falls below the trailing edge, causing errors in flow direction measurements. To some extent these errors can be studied in wind tunnels, but wind-tunnel measurements cannot replace in-flight measurements.

A meteorological research aircraft that measures air motions in additions to many other parameters has to measure with extreme accuracy not only the airspeed, but the complete vector of the velocity of a reference point relative to the air. To do that the distortion of the flow field at the reference point must be taken into account. Furthermore, the measured data must be carefully synchronized to each other if high-frequency atmospheric fluctuation are to be solved.

For the calibration of a wind measuring system, maneuvers in still air are indispensable. The method of testing and calibrating a wind measuring system by maneuvers is mainly based on the condition that all three components of the calculated wind vector should remain unchanged while the aircraft is maneuvering. In practice this can only be verified if the wind field is homogeneous and free of turbulence, which means that the components of the wind vector are constant during the flight. The more the atmosphere fluctuates, the greater the uncertainty of the results will be. This uncertainty is reduced by applying maneuvers containing steady portions and periodic maneuvers.

The SkyArrow maneuvers are designed so that as many variables as possible remain constant during each maneuver. This greatly facilitates the interpretation of the results, the

isolation of errors and the assessment of the effects of changes in the computer algorithms, and makes cross effects visible.

Each maneuver is preceded and followed by steady, straight horizontal flight of at least 30 s. This provide the reference values for the wind components and information about the state of the atmosphere at that special site. All maneuvers are intended to fly close to one of the four cardinal headings. Then, for example, if the aircraft heading is to the north, the east component of the calculated wind vector is influenced primarily by the angle of sideslip and the north component by the airspeed, and the effects of these two important variables can be isolated conveniently. The altitude and the airspeed should be maintained as steady as possible during the maneuvers (except for the acceleration maneuver).

Following are presented the classical maneuver performed by the skyarrow, where the an iterative post processing is applied, the result shown regards the last step of the iteration.

6.2 Calibration Flight Maneuvers

The calibration flight maneuvers should be performed in as smooth air as can be found. The quality of the data system calibration depends on the absence of turbulence during the entire flight. At least once per field campaign, a calibration flight should be performed. Ideally, a calibration flight should be performed anytime there is a significant modification to the data system, such as gust probe removal and replacement.

The best time of the day to find good conditions for a calibration flight is early morning or late evening.   Calibration maneuvers have been flown at night, although this may not always be feasible. The best areas to fly are those where terrain is flat, and there are no mountains, ridges, or other obstructions that could disturb airflow. If an inversion condition can be found (air temperature increasing with increasing altitude), this will generally provide the most stable, turbulence-free conditions. Calibration flights should be performed at an altitude above the local boundary layer. In the morning or evening, boundary layers will be generally shallower than during the mid-day, and altitudes at or above 5000 feet AGL will generally work well.

As each calibration maneuver is started, attention should be paid to the perceivable turbulence level in the aircraft. If there is noticeable turbulence, the maneuver should be abandoned and a different location or time selected to complete the maneuver. Data quality is directly dependent on the "smoothness" of the flight. It is also helpful for the pilot to be familiar with the aircraft so that accurate judgements can be made as to whether vibrations that may be felt are airframe/engine induced or turbulence induced.

The maneuvers should be performed to the best of the pilot's ability. As experience is gained with executing the various maneuvers, the overall system performance should improve. To enhance the pilot's ability to fly cardinal headings, the directional gyro should be reset soon after takeoff to match the JAVAD heading. This will ensure the maneuvers are flown with respect to true headings.

Attention should also be paid to keeping the wings of the airplane level using the attitude indicator as a horizon reference. With practice, bank angles can be kept within $+2^{o}$ during most maneuvers, provided there is little or no turbulence.

Airspeed should always be kept as close to the target as possible. The Sky Arrow 650 ERA has a fine-scale airspeed indicator that allows airspeeds to be monitored precisely and small

airspeed variations to be easily detected. Use of the elevator trim is also advisable for making precise adjustments to airspeed.

Probably the most important flight parameter to maintain during the calibration flight is constant pressure altitude. For a given power setting, the airplane should be trimmed to fly "hands-off", so that altitude can be easily maintained within +10 feet. If the airplane climbs or descends more than 40 feet on its own after being trimmed, the air is not smooth enough.

It is probably best to pick a "round" altitude (5000, 5500, 6000, etc) that will be agreeable to Air Traffic Control (ATC), is relatively free of other aircraft traffic, and has enough maneuvering room to fly 10 minutes in one direction without changing altitude or heading.

The processed data showed in the sections below are referred to the calibration flight held on 1th of july 2004. The aircraft took-off at 19:47 Local time.

Figure 6.1 shows the path of the flight, it was performed on the Salerno's gulf. The site was chosen for two major reasons: first, it is close to the airport where the aircraft is recovered, then is simply to reach and is also possible to stay in contact with the aircraft when the pilot performs the flight without any operator onboard. Second, flying over the sea is the better location to find homogenous atmospheric conditions free of turbulence, that is the most primary requirement to calibrate the system for wind measurements.

To check the atmospheric conditions of the atmospheric boundary layer, in particular to check is the flight was performed outside it, in the free troposphere, vertical atmospheric profile was performed during the ferry flight from the airport to the chosen site for the calibration.

Figures 6.2, 6.3 and 6.4 show respectively the temperature, potential temperature and pressure profiles performed at the end of the flight. The temperature profile shows that in the vertical temperature gradient is of about 0.65 °C every 100 m, it means that the conditions are on the boundary between the *neutral* and *unstable* conditions. In fact, the profile is considered neutral if the temperature gradient is of about 0.7 °C, unstable if is less than 0.7°C.

To eliminate the air temperature variation caused by changes in pressure altitude of an air parcel the potential temperature is defined as reference temperature of a volume of air at a pressure level of 1000 hPa. This means that every volume of air that is dry adiabatically moved from any reference place to another altitude will maintain this potential temperature:

$$\Theta(z) = T(z) \cdot \left(\frac{p_0}{p_z} \right)^k \tag{6.1}$$

$$p_0 = 1000 \ hPa \qquad k = \frac{R}{C_p} \qquad\qquad (6.2)$$

The calculated potential temperature profile is reported in figure 6.3; from it is possible to evaluate the high of the mixing layer, where inversion of temperature gradient occurs. In this case the inversion arise at about 200m, it is very low because the profile was made in the evening and was very close to the coast. It is visible also from the figure 6.5 and 6.6 where the calculated wind direction and magnitude are showed. Is possible to see different direction of the wind on ground and at the high where the calibration flight was performed.

In figures from 6.7 to 6.10 are showed some of the variables that is possible to calculate from the raw data, in particular are reported the aircraft vertical velocity during the profile, the pitch angle, the angle of attack, the sideslip angle. From there is possible to reconstruct the entire dynamic of the flight.
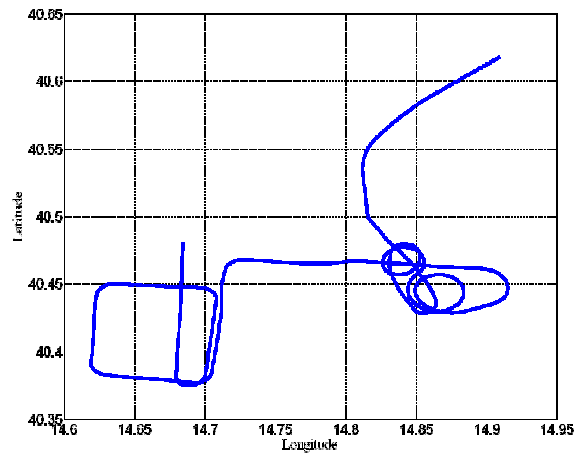
Fig 6.1:The path of the Calibration flight held on 1th of july 2004
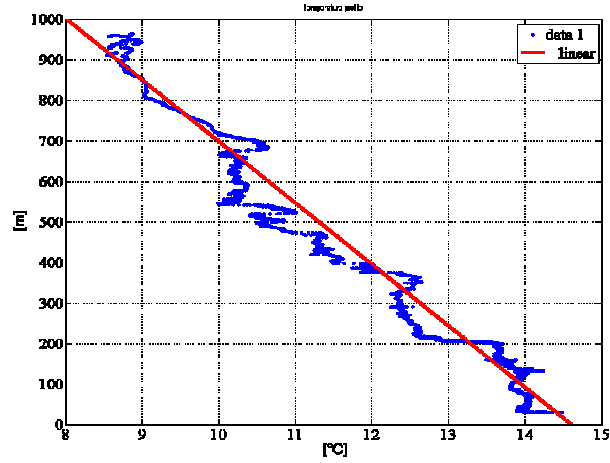
Fig 6.2: Graph of the temperature vs the altitude during the atmospheric profile
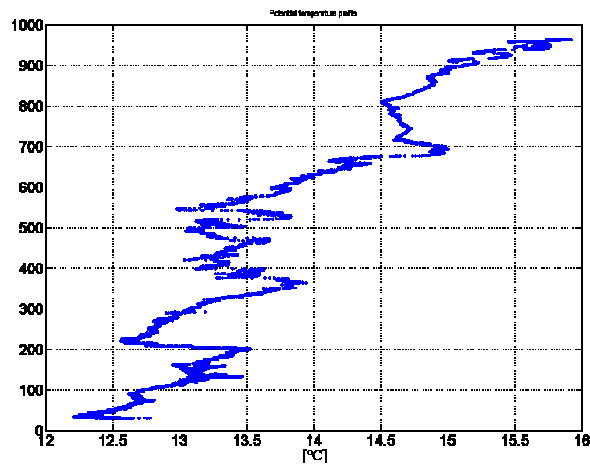
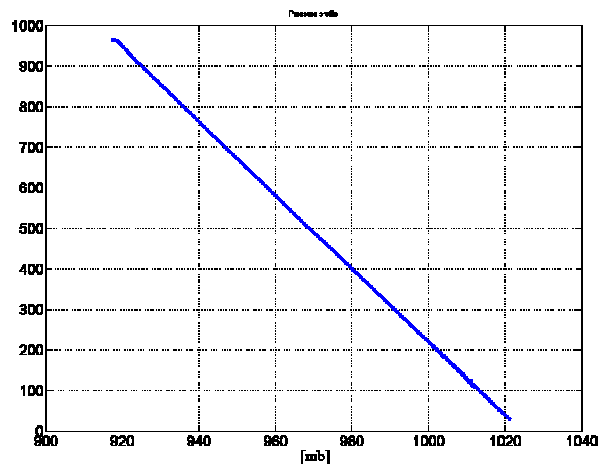*Fig 6.3: The potential temperature Vs the altitude during the atmospheric profile*

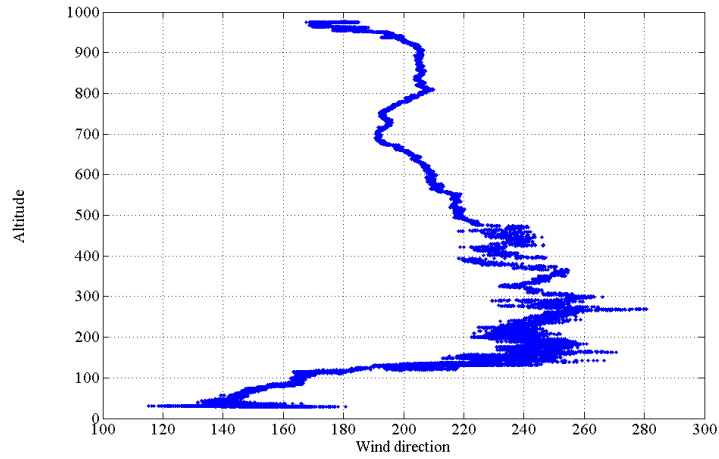*Fig 6.4: The pressure Vs the altitude during the atmospheric profile*

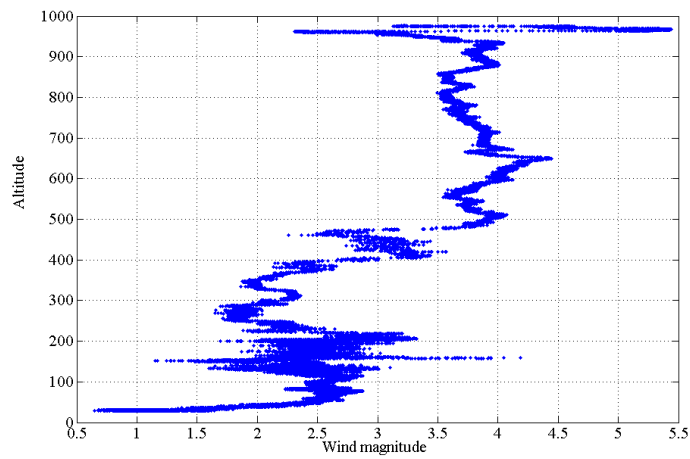*Fig 6.5: wind direction Vs the altitude during the atmospheric profile*

Fig 6.6: wind magnitude in [m s^{-1}] Vs the altitude [m] during the atmospheric profile
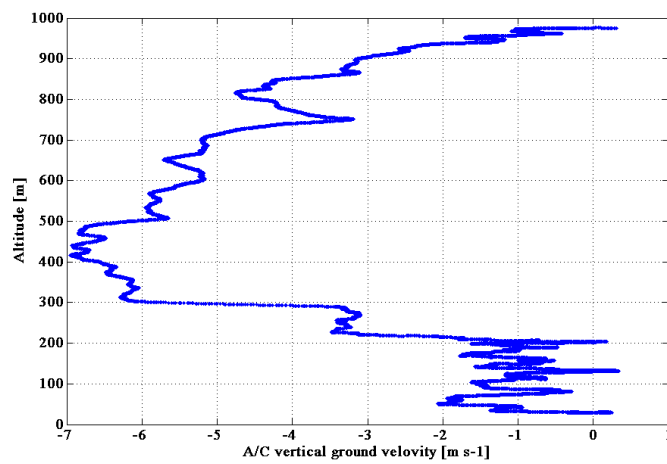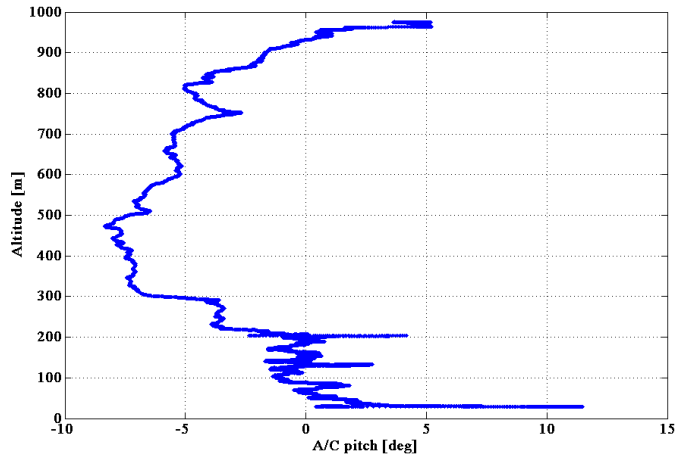

Fig 6.7: aircraft vertical ground velocity during the descending profile

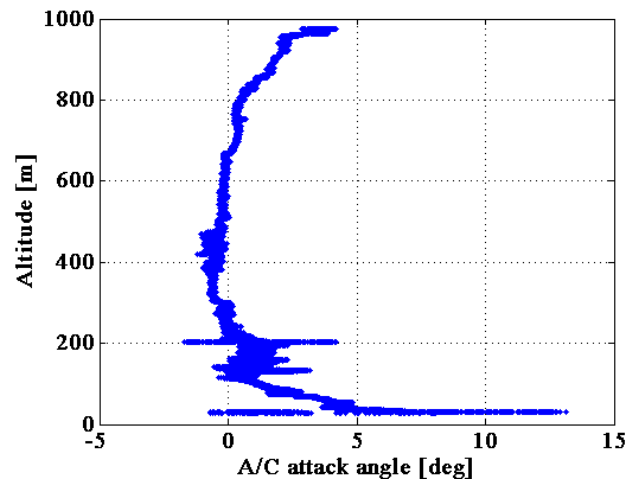*Fig 6.8: aircraft pitch angle during the descending profile*

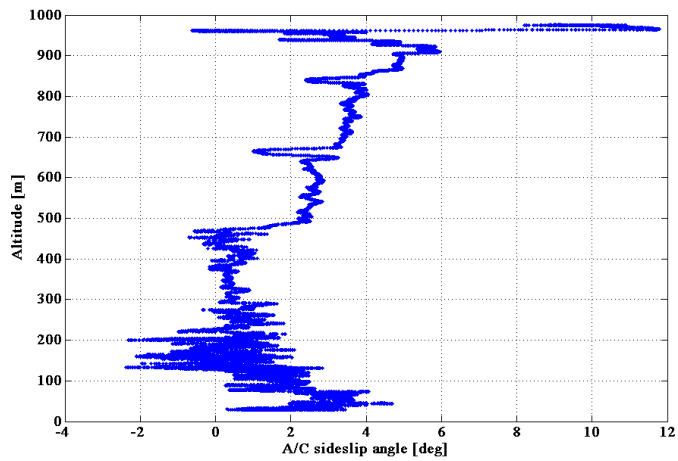*Fig 6.9: aircraft attack angle during the descending profile*

Fig 6.10: aircraft sideslip angle during the descending profile

6.2.1 Straight and Level

Flight direction straight, at constant cardinal heading (0°, 90°, 180°, or 270° true), wings level, constant airspeed of 70 KIAS, at constant pressure altitude. This condition should be established, the marker turned on, and the condition maintained for 2-5 minutes. Aircraft should be trimmed for hands-off flight during this maneuver. Altitude variance during this maneuver should be +10 feet, airspeed variance should be +1 knot, and heading variance should be +1o during the entire maneuver.

<u>TARGET</u>
FL 050
HDG:270°
IAS: 70 kts
Time: 4min

<u>TOLERANCE</u>
ALT: +10 feet
HDG: +1°
IAS: +1 knot

Start   IAS 70 kts   Finish

|————————270 °——————————————————|→
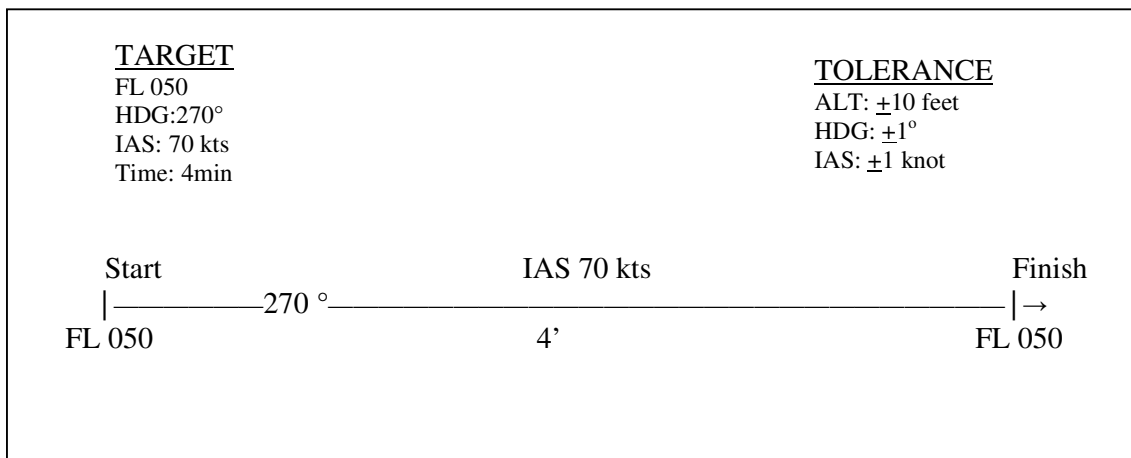
FL 050   4'   FL 050

Fig 6.4: The straight and level maneuver plan

From this maneuver is possible to evaluate the influence of the pitch on the average of the computed vertical velocity.
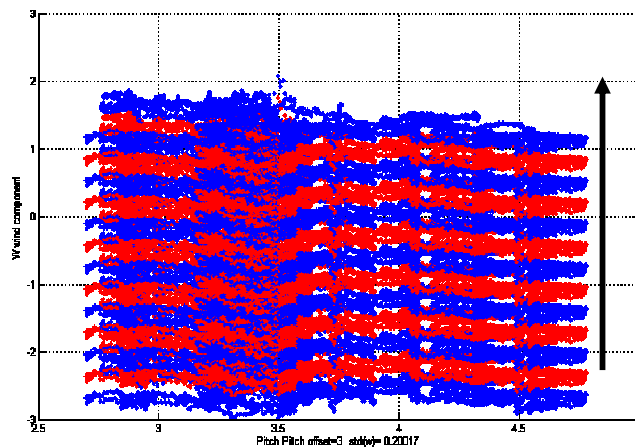

Fig 6.5: The computed vertical wind velocity Vs the pitch angle during the straight and level maneuver

In figure 6.5 is shows the computed vertical velocity Vs the pitch angle during the straight and level maneuver, at different pitch offset. We have run the algorithm for the wind calculation with pitch offset from -3 to 3, is clear that the value for that the mean vertical wind is more close to zero si Pitch_offset=1.

Plotting the mean value of the calculated vertical velocity Vs the pitch off set, is more clear this consideration. In fact the mean on the W is zero for the offset=1.
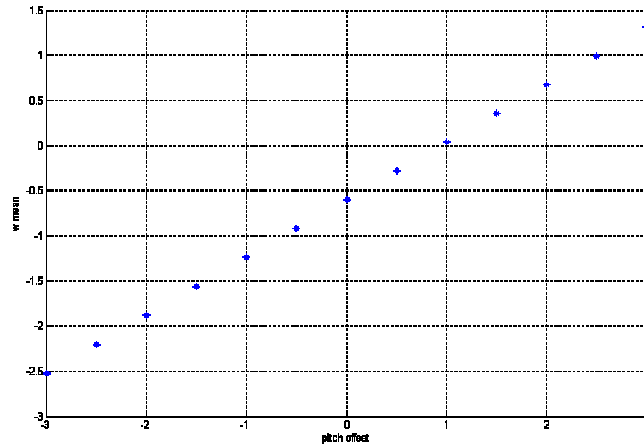

Fig 6.6: the mean of the computed vertical velocity Vs the pitch offset during the straight and level maneuver

6.2.2 Wind Box

This maneuver should begin with the aircraft on a heading of 0° true (due North), as measured by the JAVAD angle output on the laptop display. The airspeed should be 70 KIAS and the aircraft trimmed for hands-off flight at constant altitude. The marker should be turned on and a timer started. Fly at constant airspeed and constant heading for 2 minutes. Perform a standard rate turn to the left, maintaining altitude and airspeed during the turn. Aircraft should be rolled out of the turn on the heading 270° true (due West), and a timer started. After 2 minutes, the aircraft should be smoothly rolled into a left standard rate turn, maintaining constant airspeed and altitude. Roll out of the turn on a heading of 180° true (due South). Fly at constant airspeed and constant heading for 2 minutes, perform the standard rate turn to the left again, rolling out on a heading of 90° true (due East). Fly at constant airspeed and constant heading for 2 minutes, perform the standard rate turn to the left, rolling out on heading of 0° true (due North). Fly at constant airspeed and constant heading for 1 minute, and turn the marker switch off. Altitude variance during this maneuver should be +10 feet, airspeed variance should be +1 knot, and heading variance (during the straight portions, of course) should be +1° during the entire maneuver.
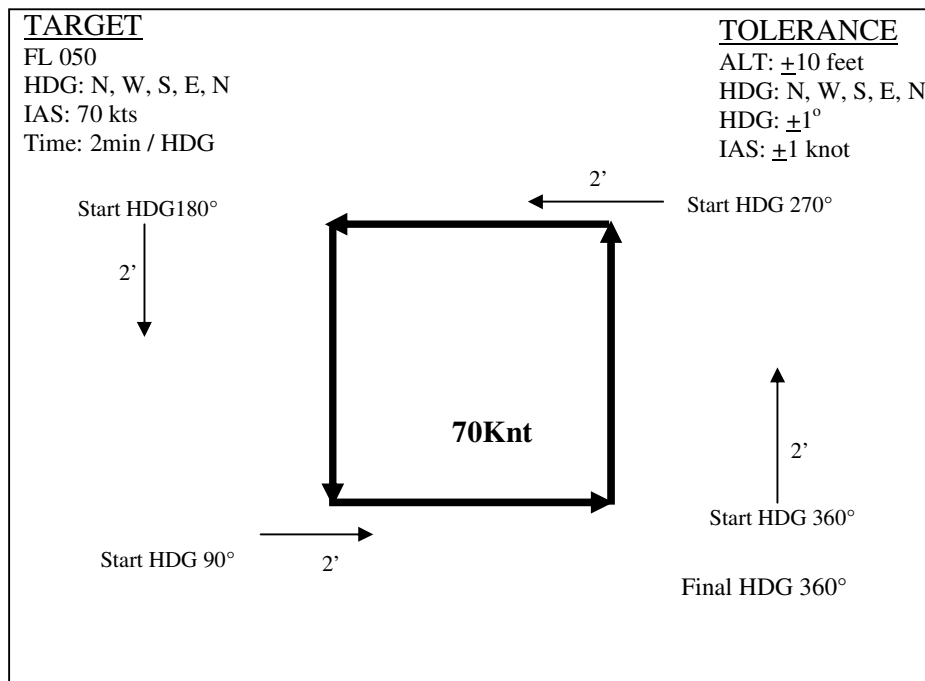

Fig 6.7: The wind box maneuver plan

From the box maneuver is possible to evaluate the best calibration factor for direction and magnitude of the calculated horizontal wind.

Mainly the horizontal wind is influenced by the error in the dynamic pressure computation regards the magnitude, and by the heading offset for the direction.

Flying with an heading of 90°, and after that flying with an heading of 270°, can be evaluated the error on the calculated north wind component, that is the component orthogonal at the flight headings. In fact if the wind field is homogenous, the value of this component should be the same in both the flight direction.

Figure 6.9 shows the north wind component along the two transect (red=90°, blue=270°) at different heading offset. The best value is of -2.8, that is the point where the two line have an intersection.

For the influence of the heading offset on the east wind component calculation, from the same consideration above, we have to consider the flight heading toward north and toward south. Figure 6.10 shows the best value at -3.2. Averaging the result above, the best heading offset to minimize the error in the calculation of the horizontal wind is -3.
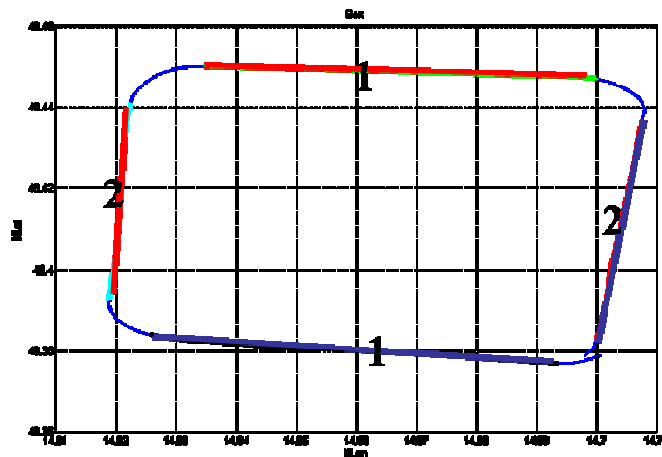

Fig 6.8: The wind box performed during the Calibration flight held on 1th of july 2004
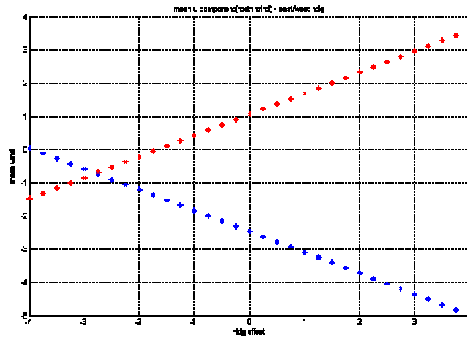
Fig 6.9: variation of the north wind component on the east-west transect, with heading of 90° (red) and heading of 270° (blue) Vs different heading offset
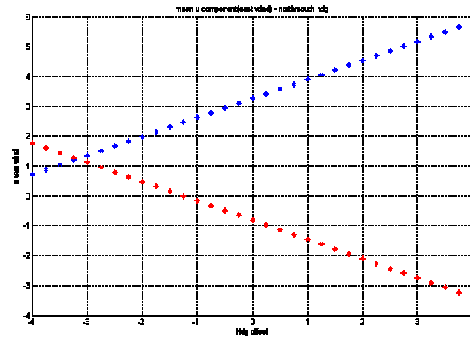
Fig 6.10: variation of the east wind component on the north-south transect, with heading of 0° (red) and heading of 180° (blue) Vs different heading offset
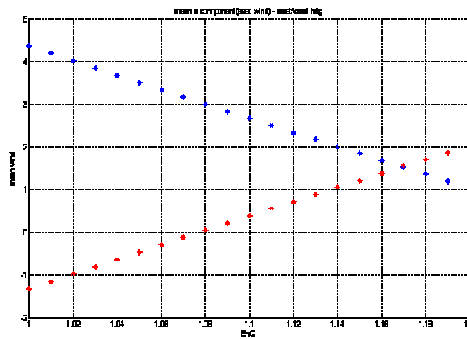

Fig 6.11: variation of the north wind component on the north-south transect, with heading of 0° (red) and heading of 180° (blue) Vs different dynamic pressure offset
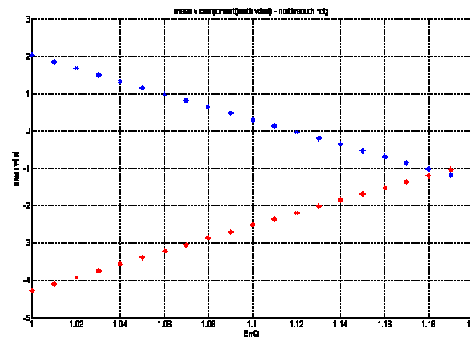
Fig 6.12: variation of the east wind component on the east-west transect, with heading of 90° (red) and heading of 270° (blue) Vs different dynamic pressure offset

The dynamic pressure is different if the aircraft is flying in-wind or out-wind, or in other words if the aircraft had the wind on the nose or on the tail. To minimize the error in the magnitude of the horizontal wind due the variation in dynamic pressure, we must evaluate the north wind component on north-south transect, and east wind component on east-west transect.

Figure 6.11 and 6.12 shows the variation of the north wind component at different dynamic pressure coefficient (ErrQ). The best ErrQ on both the heading is of 1.176.

6.2.3 Acceleration/Deceleration maneuver

This maneuver should be flown at constant pressure altitude, on a constant cardinal heading, wings level. Maintain a constant airspeed of 110 KIAS, at constant altitude, with the airplane in steady flight. Turn the marker switch on and fly for 30 seconds in this condition. Now start a timer and begin a smooth power reduction that allows airspeed to decrease constantly at a rate of 10 knots/minute. Maintain constant pressure altitude during this maneuver. Continue the smooth airspeed reduction until 60 KIAS is attained. This should take 5 minutes to complete. Note that the pitch angle of the aircraft will smoothly increase during this maneuver. Once 60 KIAS is attained, turn the marker switch off and immediately back on and begin a smooth power increase that allows airspeed to increase smoothly at a rate of 10 knots/minute. Again, maintain constant pressure altitude and continue the smooth airspeed increase until 110 KIAS is attained. This should again take 5 minutes to complete, and the pitch angle will smoothly decrease during this portion of the maneuver. After attaining 110 KIAS, turn the marker switch off. Altitude variance during this maneuver should be +10 feet, airspeed variance should be +1 knot, and heading variance should be +1° during the entire maneuver.

Note: This maneuver is probably the most difficult to complete smoothly with the Sky Arrow 650 ERA. Because the airplane doesn't have an autopilot, altitude must be maintained manually while performing smooth power and pitch changes. Pitch control should be done with the trim as much as possible. Perfecting this maneuver may take some practice.

FL 050	ALT: +10 feet
HDG: 270°	HDG: +1°
IAS: 90 kts	IAS: +1 knot

Time: 8 min 30 sec.

Start   30''   MKR ON   3min   MKR OFF / ON   5min   MKR OFF
Finish

|————————|————————————————|————————————————|————

—|→

FL 050   90 kts → 60 kts   60kts → 110 kts
FL 050
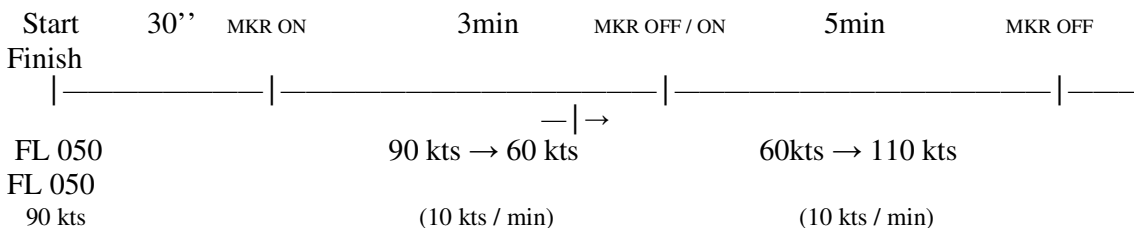90 kts   (10 kts / min)   (10 kts / min)

Fig 6.13: the pitch calibration maneuver plan

The wing in generating lift induces, among other things, an upward flow deflection ahead of the airplane (upwash), this directly influence the calculated vertical wind component (Crawford et al,1993).

The upwash effect increase with the lift and then with true air speed of the aircraft. In figure 6.14 is showed the calculated true air speed during the acceleration/deceleration maneuver.

In this maneuver we can see a variation of the airspeed of about 10 m s^{-1}, that is consistent range to evaluate the best calibration factor to minimize the error in the calculated vertical wind component.

Figure 6.15 shows the standard deviation of the vertical wind at different upwash coefficient. The best coefficient is in correspondence of the minimum of the curve, that is the minim variation of the calculated vertical wind component at different upwash effect on the nose of the airplane.

With Kupwash of 0.15 we have a W standard deviation of 0.055 m s^{-1}.
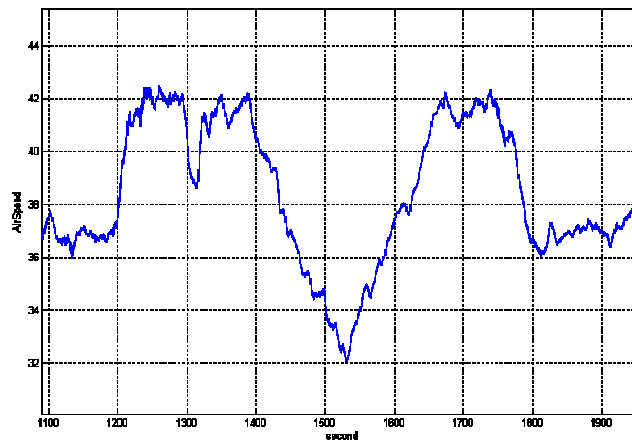

Fig 6.14: time series of the calculated true air speed during the pitch calibration maneuver
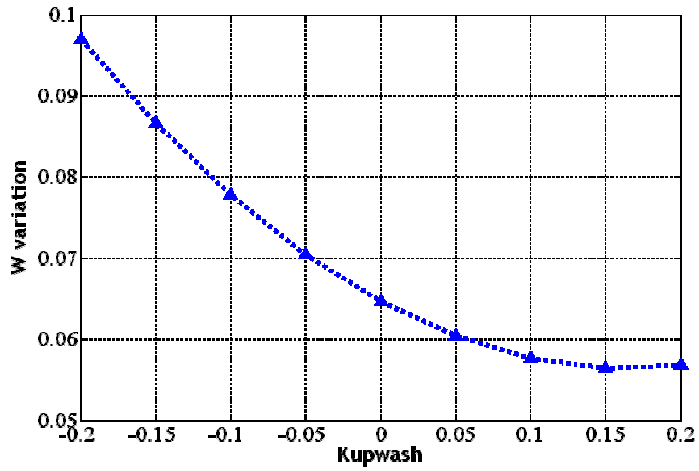
Fig 6.15: variation of standard deviation of the calculated vertical wind component Vs different upwash coefficients

6.2.4 Pitch Up/Down

This maneuver should be flown at constant pressure altitude, flying the airplane at a constant cardinal heading, maintaining 70 KIAS. To optimize the post processing is possible to turn the marker switch on before the maneuver. The first step consist to fly straight and wings level for 30 seconds. Next, the pilot has begin to pitch the airplane up allowing the nose to reach a maximum pitch angle (approximately 5° nose up) in a period of approximately 5 seconds. Immediately after the nose reaches the maximum nose-up angle, begins to pitch the nose down. After 5 seconds, the plane should be nose-level, and the pitch maneuver should continue smoothly until the nose is approximately 5o down, which again should take approximately 5 seconds. The nose should then be smoothly brought back to level, again taking approximately 5 seconds. The idea is to complete one pitch up/down cycle in 20 seconds. The 20-second cycle should then be smoothly repeated 6 times, taking two minutes for the full maneuver. After completion of the maneuver, the nose should be level and the airplane held straight and level for another 30 seconds. The marker switch should then be switched off. Altitude variance during this slow pitch maneuver should be allowed to vary as necessary, but altitude should always return to the original starting altitude as the plane passes through nose-level. The airspeed variance should be +1 knot and heading variance should be +1° during the entire maneuver.

This procedure should be repeated as outlined above, using a 2.5-second period instead of a 5-second period. This is the medium frequency pitch up/down maneuver. Begin the maneuver with marker switch on and 30 seconds of straight and level flight. In this case, each pitch up/down cycle should be repeated 6 times to make the duration of the complete maneuver one-minute. After the pitch cycles, finish the maneuver with 30 seconds of straight and level flight. Maintain the same altitude, airspeed, and heading tolerances as shown above. Note that the maximum pitch angle should be adjusted to keep the altitude excursions within a reasonable tolerance.

The final pitch up/down maneuver is made at high frequency. The complete pitch cycle (nose up, nose down, nose up) should take approximately 1 second to complete. Note that the altitude variation should not exceed approximately 20-50 feet during the pitching portion of this maneuver. Begin with marker on and 30 seconds of straight and level flight. Perform 30 pitch up/down cycles at high frequency and finish with 30 seconds of straight and level flight.

Maintain the same airspeed and heading tolerances as shown above. Again, adjust the maximum pitch up and down angle as necessary to prevent excessive altitude excursions.

Note that this maneuver has the potential to introduce large vertical accelerations on the aircraft unless the pitch angle is carefully monitored.

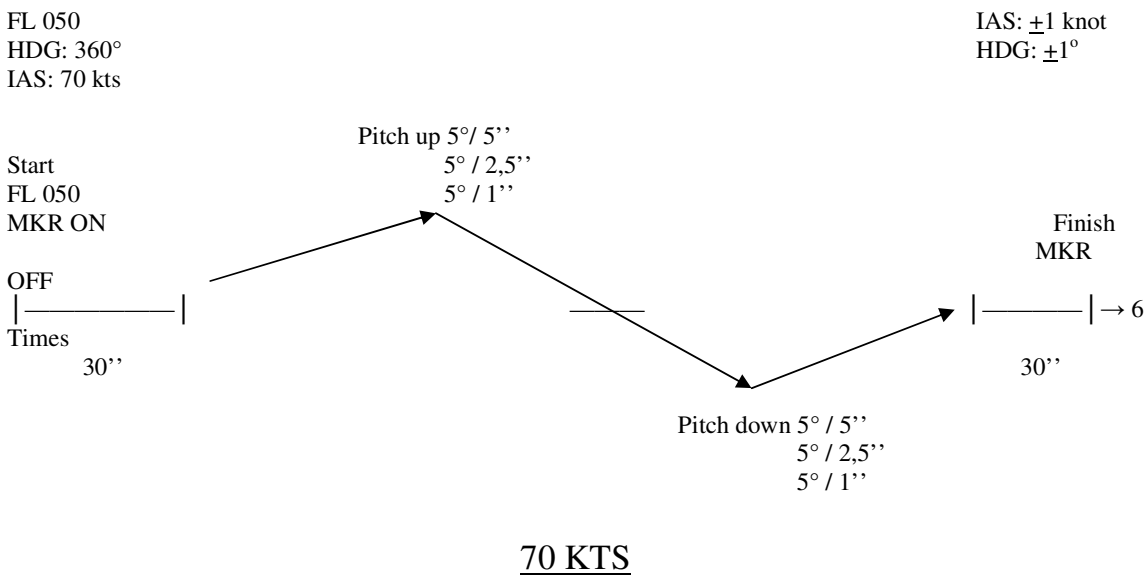See figure 6.16 where is showed the procedure explained above.

FL 050
HDG: 360°
IAS: 70 kts

IAS: ±1 knot
HDG: ±1°

Pitch up 5°/ 5''
5° / 2,5''
5° / 1''

Start
FL 050
MKR ON

Finish
MKR

OFF

| Times
30''

| → 6
30''

Pitch down 5° / 5''
5° / 2,5''
5° / 1''

70 KTS

Fig 6.16: pich up/down maneuver procedure

The angle of attack, the pitch angle, the static and dynamic pressures, and the vertical acceleration are synchronized by this manuever. The calibration factors for the measured angle of attack and for the attack angle effect on static and dynamic pressures can be determined very precisely.

For this calibration flight the pilot was not able to apply the entire procedure, as is showed in figure 5.17, the pilot performed an oscillation of a period of 5 seconds (0.2 hz), and 4 oscillation with a period of 2,5 seconds (0.4 Hz).

The "*pitch up/dn*" manuever is used calculate the optimum *"Kalpha"* coefficient, forcing the variance of the calculated vertical wind . The general rule of thumb criterion for acceptable calibration of the system is that peak-to-peak variation in the vertical wind should be less than 10% the variation of the ground-relative aircraft velocity. The high sampling

frequency of the air data and of the computed aircraft vertical velocity (50 Hz) is a great benefit for the analysis.

From figure 6.18 is possible to see that the optimum *Kalpha* calibration factor is of 0.205, for what we have a standard deviation for the vertical wind of 0.09 m s^{-1}.
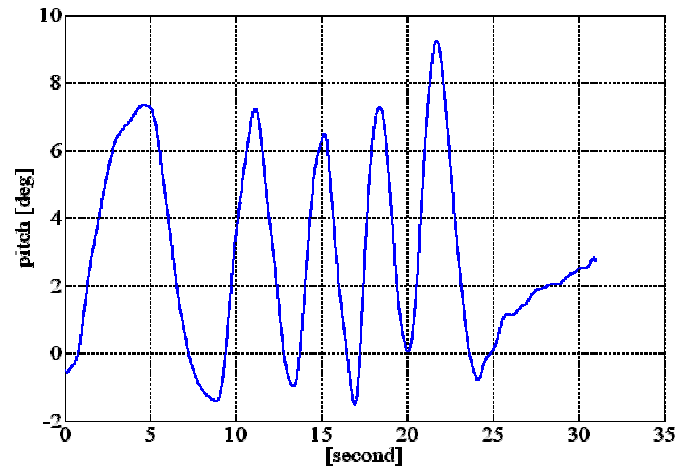

Fig 6.17: the pitch up/down maneuver performed during the calibration flight
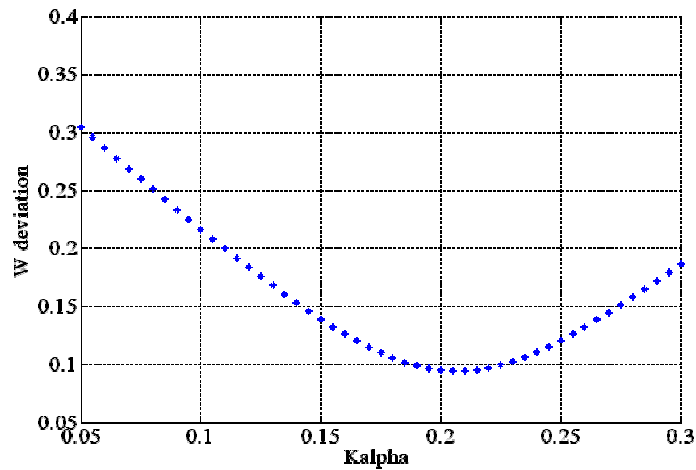

Fig 6.18: standard deviation of the calculated vertical wind component in respect with different angle of attack coefficients
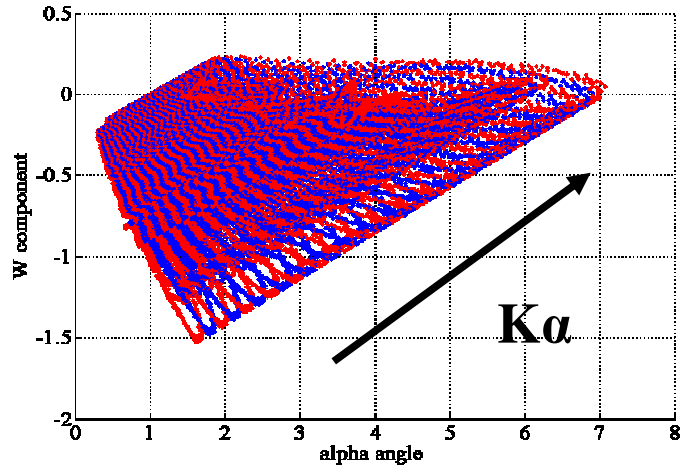
Fig 6.19: variation of the vertical wind component in respect with variation in angle of attack, for different angle of attack coefficients

Figure 6.19 shows how the vertical wind plume trend goes towards a line with zero angular coefficient while the *Kalpha* goes towards the optimum value, is also possible to see how the standard deviation diminish (figure 6.21 shows the vertical wind plume for *Kalpha*=0.205.

From the figure 6.20 can be checked if the calibration is well done, in fact as we told before the rule of thumb criterion for acceptable calibration of the system is that peak-to-peak variation in the vertical wind should be less than 10% the variation of the ground-relative aircraft velocity, the red line is the vertical aircraft velocity and for each oscillation we have that the rule of thumb is accomplisced.
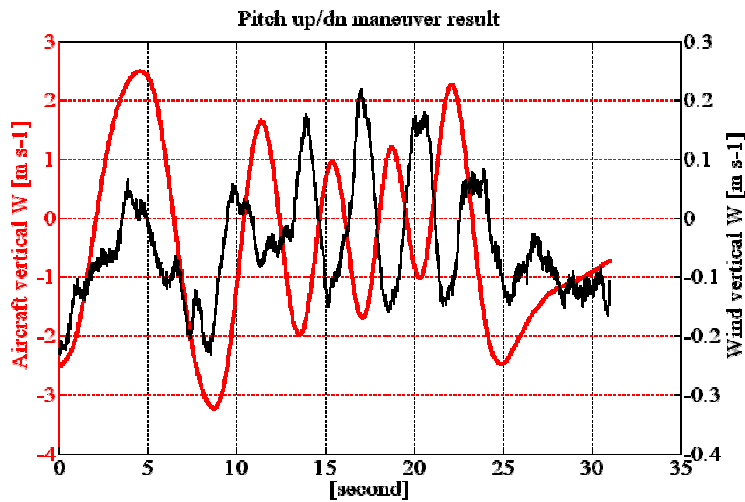
.

Fig 6.20: comparison between the vertical component of the aircraft ground speed and the calculated vertical wind component with the optimum angle of attack coefficient
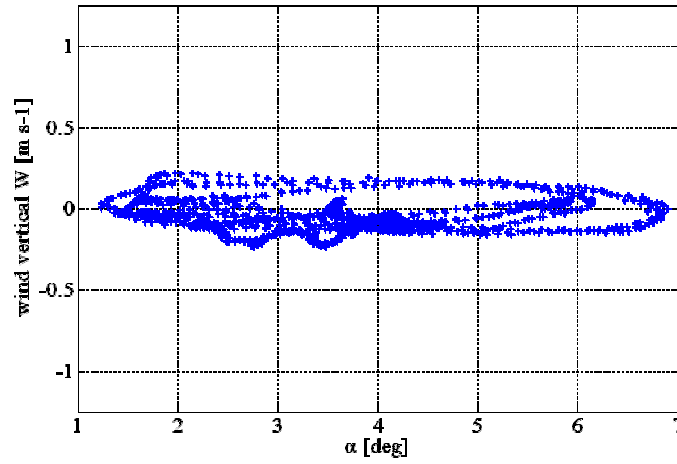

Fig 6.21: the computed vertical wind component Vs the angle of attack variation during the pitch oscillation maneuver
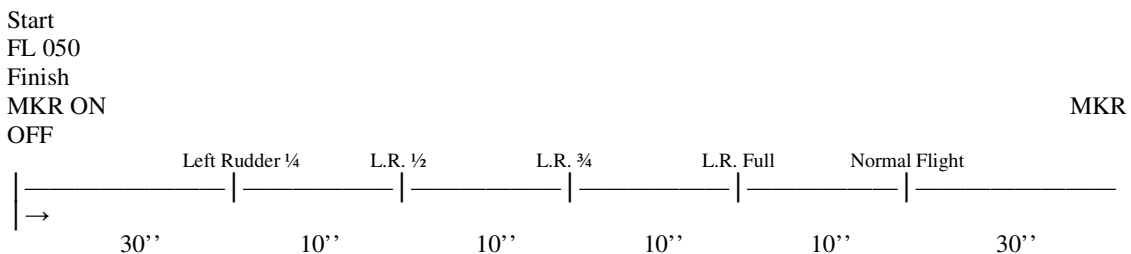
6.2.5 Yaw Left/Right

This maneuver should be flown at constant pressure altitude. It is started with the aircraft in straight and level flight on a cardinal heading at 70 KIAS. Start by turning the marker switch on and maintaining straight and level coordinated flight for 30 seconds. While maintaining wings level with aileron input, depress the left rudder pedal until the ball on the turn coordinator displaces approximately ¼ ball width. The heading of the aircraft will begin to change as rudder input is introduced. This is normal and should be allowed to continue as necessary. Maintain ¼ ball deflection for 10 seconds, then depress the left pedal further until the ball deflection is ½ ball width. Maintain this condition for 10 seconds. Depress the rudder pedal until the ball deflection is approximately ¾ ball width and maintain this for 10 seconds. Finally, depress the pedal until the ball is displaced a full ball width. Maintain this condition for 10 seconds, then smoothly return to properly coordinated flight. Maintain constant pressure altitude, airspeed, and heading for 30 seconds, then turn the marker switch off. Altitude variance during this maneuver should be +10 feet, airspeed variance should be +1 knot, and bank angle variance should be +2o during the entire maneuver.

Repeat the steps above using right rudder pedal deflections. Perform the right rudder deflections in the same order and maintain the same tolerances as shown above.

HDG: 270°   BANK: $\pm 2^{o}$
IAS: 70 kts   IAS: ± 1 knot

Start
FL 050
Finish
MKR ON   MKR
OFF

| | Left Rudder ¼ | | L.R. ½ | | L.R. ¾ | | L.R. Full | | Normal Flight |
|——————————————| | ——————————| | ——————————| | ——————————| | ——————————| | ————————————
| →
| 30''   10''   10''   10''   10''   30''

Note: Repeat the steps above using right rudder pedal deflections.

Fig 6.22: The yaw left/right maneuver procedure

The "*yaw left/right*" manuever is used calculate the optimum *"Kbeta"* coefficient, forcing the variance of the calculated horizontal wind magnitude and direction to the minimum.

Figure 6.23 shows the performed maneuver. In figure 6.24 are reported the standard deviation for the wind magnitude and direction versus the kbeta calibration factor. The best value found is of 0.19. Figures 6.25 and 6.26 show how the time series of the wind speed and direction rotate at the variation of kbeta, and how the deviation standard diminish.
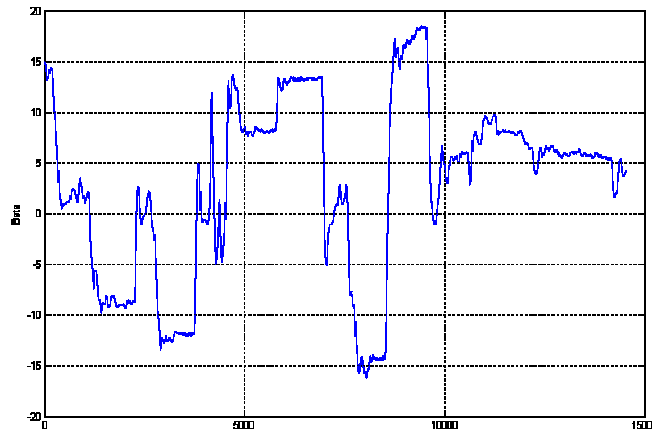
Fig 6.23: the sideslip angle during the maneuver

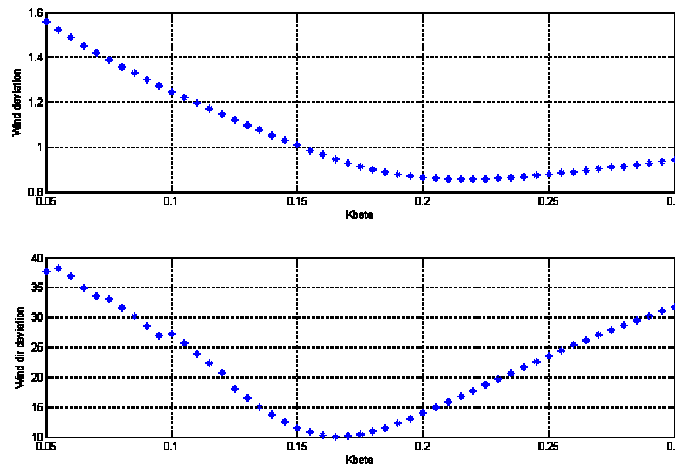Fig 6.24: standard deviation of the magnitude and direction wind Vs the calibration factor Kbeta
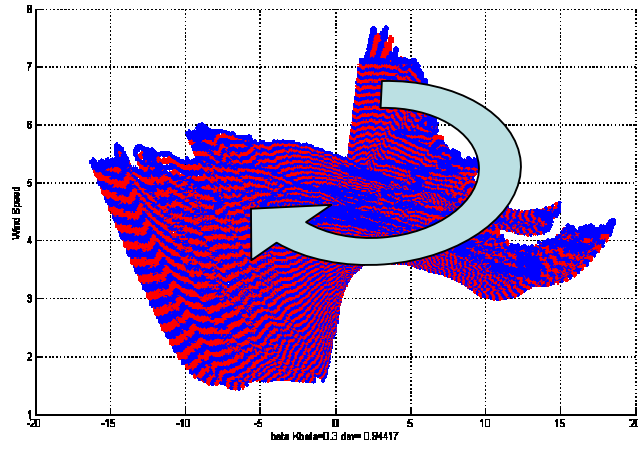
Fig 6.25: variation of the wind speed respect to variation in kbeta
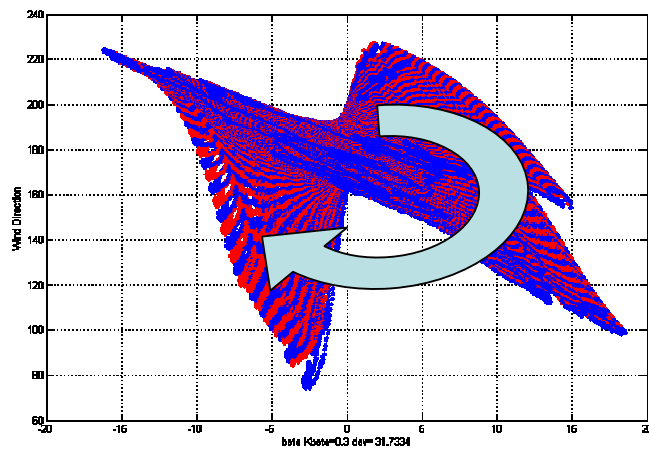

Fig 6.26: variation of the wind direction respect to variation in kbeta
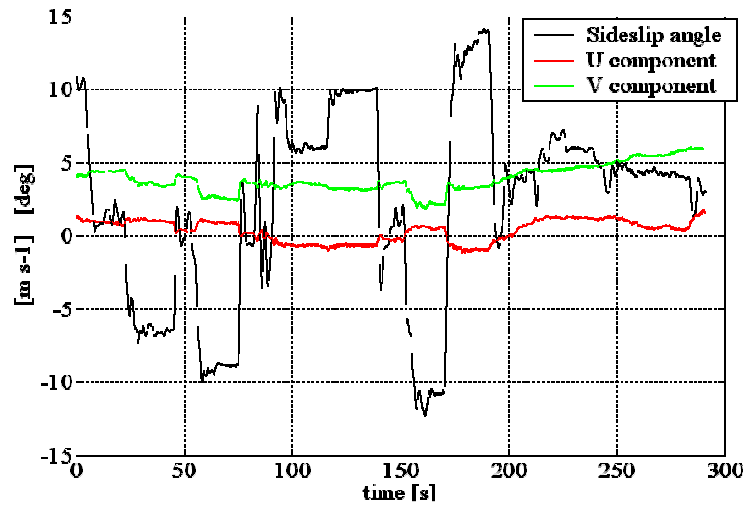
Fig 6.27: variation of the wind speed regards kbeta

In figure 6.27 are showed the residual error on the north and east component   after the calibration.

6.2.6 Wind Circle

This maneuver should be flown at constant pressure altitude. Roll the airplane into a left standard rate turn and establish and maintain 70 KIAS. As the heading passes through 0° true, turn the marker switch on. Maintain the condition through 360°, turning the marker off as the heading passes through 0° true again. Continue the left turn through another 45-90°, roll the plane back to the right and repeat the procedure for a turn to the right. Be sure the turn is established and everything is steady before turning the marker switch on. Altitude variance during this maneuver should be +10 feet, airspeed variance should be +1 knot, bank angle variance should be +2°, and the turn rate variance should be held to a minimum as much as possible during the entire maneuver.

FL 050   ALT: $\pm$10 feet
HDG: 360°   BANK: $\pm$2°
IAS: 70 kts   IAS: $\pm$1 knot
Time: Standard turn (360°/2min)

Step 1   Step 2

HDG 360°   HDG 360°
START → MKR ON   START → MKR ON
OFF   OFF
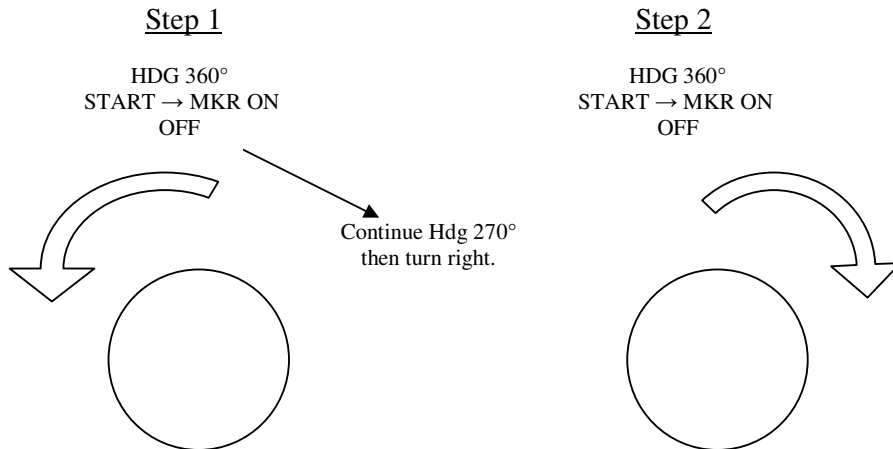
Continue Hdg 270°
then turn right.

Fig 6.28: wind circle maneuver procedure

The wind circle maneuver is used to test the performance of the set of the calibration factor found on this calibration flight. In the table below are showed the value of the calibration factor after an iteration to do stabilize the coefficients.

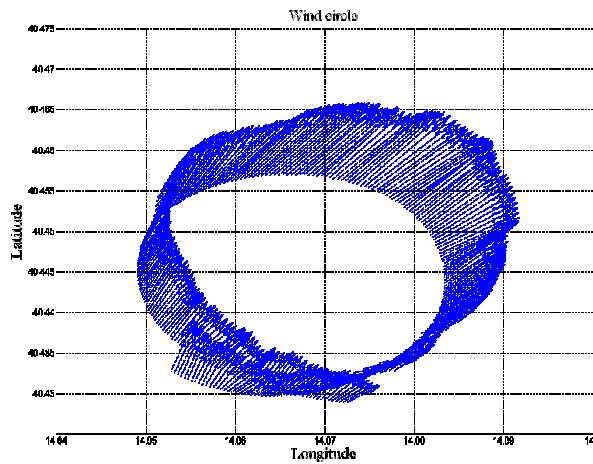| CALIBRATION FACTOR	VALUE
Kbeta	0.19
Kα	0.205
PitchOff	1
Kupwash	0.15
ErrQ	1.176
Hdg_off	-3

Tab 6.1

Fig 6.29: the calculated wind vector on the wind circle maneuver

In figure 6.29 is showed the wind vector on an circle performed by the aircraft. The circle is a good test because all the variation are done gradually, and bank, heading and sideslip angles are syncronized in the maneuver. The mean wind direction is of 225° with a standard deviation of 10°.

CONCLUSIONS AND OUTLOOK

A remote sensing system was developed and tested, with it is possible to collect multispectral images in the visible or in the near infra.red, and thermal infrared images at the same time. The system works at the same time of the *Mobile Flux Platform* and is synchronized with it by means of the TTL trigger signal from the GPS receiver. This allow to refer each image at the position of the aircraft, and to know which was the attitude of the aircraft at the time of the acquisition. By means of the other sensors mounted onboard the SkyArrow, that are also synchronized with the GPS, is possible also to know the air temperature, the humidity, PAR and Net radiation, wind direction and magnitude. This parameters could be used in radiative transfer modeling for atmospheric correction so will be possible to evaluate the actual radiation reaching the sensor.

The system can be improved in dimension and in power consumption by means of the new framegrabber model, the project is already in developing. The new device will allow to collect images from both the multispectral cameras (CIR/RGB) and to collect them at 10 bit of resolution.

The thermal camera has been calibrated by means of a black body source, after that is possible to have the relation between the digital counts of the image and the radiance comes out from the target observed. Moreover the accuracy in temperature was improved calibrating the camera in a short range of temperature compatible with the commonly temperatures present over forest and crop site, that are the main target of the operator of the aircraft.

Another calibration should be performed to check the stability of the camera.

A tools for wind calculation and calibrations were developed in Matlab environment and was tested over several campaigns of the SkyArrow aircraft, some of them are listed below:

1. Mind project – extremadura (Spain), Tolfa (Italy)

2. Carboeurope project - Les Landes (France),

3. Eagle project – Netherlands

4. ARPAEM – Forlì area (Italy)

5. ISAFoM sperimentations – Piana del Sele (Italy)

Problem on the calibration of the wind procedure arises because not always is possible to perform the maneuvers in the right manner, one of the reasons is related to the low weight of the aircraft that leads the instability of the aircraft during the maneuvers.

REFERENCES

Axford, D. N., 1968: On the Accuracy of Wind Measurements Using an Inertial Platform in an Aircraft, and an Example of a Measurement of the Vertical Mesostructure of the Atmosphere, *J. Applied Meteorology, 7, 645-646.*

Arin, A., 2002, Commercial regional space/airborne imaging, thesis at DEPARTMENT OF THE AIR FORCE AIR UNIVERSITY AIR FORCE INSTITUTE OF TECHNOLOGY

Boghel, W., and R.Baumann, 1991: Test and calibration of the DLR Falcon wind measuring system by maneuvers. *J. Atmos. Ocean. Technol., 8, 5-18.*

Brown, E. N., C. A. Friehe, and D. H. Lenschow, 1983: The use of pressure fluctuations on the nose of an aircraft for measuring air motion. *J. Climate Appl. Meteorol.,* **22,** 171-180.

Cooper, W. A., and D. Rogers, 1991: Effects of airflow trajectories around aircraft on measurements of scalar fluxes. *J. Atmos. Oceanic Technol.,* **8,** 66–77.

Crawford, T. L., and R. J. Dobosy, 1992: A sensitive fast-response probe to measure turbulence and heat flux from any airplane. *Bound.-Layer Meteor.,* **59,** 257–278.

----------- , and E. J. Dumas, 1996: Aircraft wind measurement considering lift-induced upwash. *Bound.-Layer Meteor.,* **80,** 79–94.

Desvignes, F., 1987, "Détection et détecteurs de rayonnements optiques », Masson, Mesures physiques, Paris.

Dobosy, R. J., and T. L. Crawford, 1996: Accurate aircraft wind measurements using the global positioning system (GPS). *Proc. Conf. and Exhibition on Airborne Remote Sensing,* San Francisco, CA, ERIM International, 24–27.

Eckman, R. M., T. L. Crawford, E. J. Dumas, and K. R. Birdwell, 1999: Air-borne meteorological measurements collected during the Model Validation Program (MVP) _eld experiments at Cape Canaveral, Florida, in press as a NOAA Technical Memorandum, NOAA Air Resources Laboratory, Atmospheric Turbulence and Diffusion Division, Oak Ridge, TN

Etkin, B., 1963: *Dynamics of Flight—Stability and Control.* Wiley and Sons, 519 pp.

Flēchard, C. R., R. L. Desjardins, J. I. MacPherson, T. Zhu, D. Wang, and E. Pattey, 2001: Measuring Trace Gas Fluxes on a Regional Scale Using Airborne Relaxed Eddy Accumulation, Proc. 11th AMS Symposiu

French, J. R., R. Johnson, S. Beard, and T. L. Crawford, 2004: Modification of an airborne gust probe for hurricane boundary layer research. *Proc. 26th Conf. On Hurricanes and Tropical Meteorol.* 332-333. Am. Meteorol. Soc., Boston, MA.

Gioli B.,*, Franco Miglietta, Biagio De Martino, Ronald W.A. Hutjes, Han A.J. Dolman, Anders Lindroth, Marcus Schumacher, Maria Jose` Sanz, Giovanni Manca, Alessandro Peressotti, Edward J. Dumas, 2004. Comparison between tower and aircraft-based eddy covariance fluxes in five European regions. Agricultural and Forest Meteorology.

Hacker, J. M., and T. L. Crawford, 1999: The BAT probe: The ultimate tool to measure turbulence from any kind of aircraft (or sailplane). *J. Tech. Soaring,* **23:**2, 43-46.

Haering, E. A., Jr., 1992: Airdata calibration techniques for measuring atmospheric wind profiles. *J. Aircraft,* **29,** 632–639.

Khelif, D., S. P. Burns, and C. A. Friehe, 1999: Improved wind measurements on research aircraft. *J. Atmos. Ocean. Technol.,* **16,** 860-875

Lowson, R.P.,1979: A system for airborne measurement of vertical air velocity. *J.Appl.Meteor.,* **18**, 1363-1368.

Leach, B. W., and J. I. MacPherson, 1991: An application of Kalman filtering to airborne wind measurement. *J. Atmos. Oceanic Technol.,* **8,** 51–65.

Legrand, M., Pietras, C., Brogniez, G., Haeffelin, M., Khalil Abuhassan, N., and Sicari, M.,: A High-Accuracy Multiwavelength Radiometer for In Situ Measurements in the Thermal Infrared. Part I: Characterization of the Instrument *Journal of Atmospheric and Oceanic Technolog*y, Volume **17**, Issue 9 (September 2000) pp. 1203–1214.

-------, and , 1994: Comments on ''Correction of inertial navigation with Loran C on NOAA's P-3 aircraft.'' *J. Atmos. Oceanic Technol.,* **11,** 1048–1053.

Leise, J. A. and J. M. Masters, 1991: Wind measurement from aircraft, draft report, NOAA Aircraft Operations Center, Miami, FL.

Lenschow, D. H., 1972: The measurement of air velocity and temperature using the NCAR Buffalo aircraft measuring system. NCAR Tech. Note EDD-74, 39 pp. [Available from UCAR Communications, P.O. Box 3000, Boulder, CO 80307-3000.]

-------, 1986: Aircraft measurements in the boundary layer. *Probing the Atmospheric Boundary Layer,* D. H. Lenschow, Ed., Amer. Meteor. Soc., 39–55.

-------, E. R. Miller, and R. B. Friesen, 1991: A three-aircraft intercomparison of two types of air motion measurement systems. *J. Atmos. Oceanic Technol.,* **8,** 41–50.

Lentz, W.A., 1998, Characterization of noise in uncooled IR bolometer array, Master of Engineering in Electrical Engineering and Computer Science.

MacPherson, J. I. and R. L. Desjardins, 1991: Airborne Tests of Flux Measurement by the Relaxed Eddy Accumulation Technique, 7th Symp. on Met. Observations & Instrumentation, 6-11, New Orleans.

-------, 1978: Wind tunnel and flight tests of temperature probes used on the NAE T-33 and Twin Otter atmospheric research aircraft. NRC Report NAE LTR-FR-62, 34 pp. [Available from Flight Research Laboratory, National Research Council, Ottawa, ON K1A 0R6, Canada.]

-------, 1985: Wind tunnel calibration of a PMS canister instrumented for airflow measurement. NRC Report NAE NAE-AN-32, 63 pp. [Available from Flight Research Laboratory, National Research Council, Ottawa, ON K1A 0R6, Canada.]

-------, 1990: Wind and flux calculations on the NAE Twin Otter. NRC Report NAE LTR-FR-109, 38 pp. [Available from Flight Research Laboratory, National Research Council, Ottawa, ON K1A 0R6, Canada.]

-------, 1993: Use of a wing-mounted airflow pod for airborne wind and flux measurement. Preprints, *Eighth Symp. on Meteorological Observations and Instrumentation,* Anaheim, CA, Amer. Meteor. Soc., 169–174.

-------, and D. Baumgardner, 1987: Studies of aircraft flow effects about wing-mounted PMS probes. Preprints, *Sixth Symp. on Meteorological Observations and Instrumentation,* New Orleans, LA, Amer. Meteor. Soc., 144–147.

Masters, J. M., and J. A. Leise, 1993: Correction of inertial navigation with Loran C on NOAA's P-3 aircraft. *J. Atmos. Oceanic Technol.,* **10,** 145–154.

Menenti, M., Choudhury, B.J., 1993, "Parameterization of land surface evaporation by means of location dependent potential evaporation and surface temperature range". *Exchanges processes at the land surface for a range of space and time scales*, pp. 561-568.

NASA. NASA System Engineering Handbook. Washington D.C.: NASA, 1995.

Pietras, C. 1996, "Développement d'un radiomètre infrarouge thermique multicanal : qualification du prototype large champ CLIMAT", Ph.D. thesis, Université des Sciences et Technologies de Lille, Lille, France.

Pisani, 2005, Ph.D thesis on "Optical characterization of tropospheric aerosols in the urban area on Naples", University of Study of Naples.

Rees, W.G., 2001, Physical principles of remote sensing, second edition.

Riegel, C. A., 1992: *Fundamentals of Atmospheric Dynamics and Thermodynamics,* World Scientific, 496 pp.

Rosemount, 1981: Total temperature sensors. Rosemount Engineering Company Technical Bulletin 5755 (Rev. A), 29 pp. [Available from Rosemount Engineering Company, P.O. Box 35129, Minneapolis, MN 55435.]

Rossow, W.B., and Miriam D. Roiter, Update of Radiance Calibrations for ISCCP, Christopher L. Brest, *Journal of Atmospheric and Oceanic Technology, Volume 14, Issue 5 (October 1997) pp. 1091–1109.*

Sensor Inc, 2004, The Sensitivity of Focal Plane Arrays and Cameras, Sensor Unlimited technical note.

Slater, P.N., 1980: "Remote Sensing, Optics and Optical System", Addison-Wesley publishing Company, 1980

------, and Stuart F. Biggar, 1996, "Suggestions for Radiometric Calibration Coefficient Generation", *Journal of Atmospheric and Oceanic Technology, Volume 13, Issue 2 (April 1996) pp. 376–382*

Shaw, W. J., 1988: Inertial drift correction for aircraft-derived wind fields. *J. Atmos. Oceanic Technol.,* **5,** 774–782.

Su, Z., 2002, Hydrology and Hearth system Sciences 6(**1**), pp. 85-99.

Tjernstrorm, M., and C. A. Friehe, 1991: Analysis of a radome airmotion system on a twin-jet aircraft for boundary-layer research. *J. Atmos. Oceanic Technol.,* **8,** 19–40.

Whitmore, S. A., T. R. Moes, and T. J. Larson, 1992: High angle-ofattack flush air data sensing system. *J. Aircraft,* **29,** 915–919.

Wyngaard, J. C., 1991: On the maintenance and measurement of scalar fluxes. *Land Surface Evaporation—Measurement and Parameterization,* T. J. Schmugge, and J.-C. Andre´, Eds., Springer- Verlag, 199–229.

-------, L. Rockwell, and C. A. Friehe, 1985: Errors in the measurement of turbulence upstream of an axisymmetric body. *J. Atmos. Oceanic Technol.,* **2,** 605–614.

WEB SITES REFERENCES

[1]   http://www.via.com.tw/

[2]   http://www.pc104.org/

[3]   http://www.eduspace.esa.int/

[4]   http://ccrs.nrcan.gc.ca/resource/tutor/fundam/chapter2/03_e.php

[5]   http://ara.es.flinders.edu.au/

[6]   http://ara.es.flinders.edu.au/

[7]   http://www.noaa.inel.gov/Capabilities/Bat

[8]   http://www.edgetech.com/mh_200.htm

[9]   http://www.everestinterscience.com/Products/4000.4ZLprod.htm

[10]   http://www.javad.com

[11]   http://env.licor.com/Products/GasAnalyzers/7500/7500.htm

[12]   http://www.novatel.ca/Products/oem4g2.asp

[13]   http://www.rieglusa.com/

[14]   http://www.flatpanel.com/products/M3300Series.html

APPENDIX: AIRBORNE EDDY COVARIANCE

The flux calculation procedure requires the wind components to be derived from the 50 Hz raw data out of the MFP. The subsequent calculation of carbon dioxide, water vapour, sensible and latent heat and momentum fluxes are made using conventional eddy covariance technique taking into account all the necessary corrections for open-path gas analyzers. The main difference between airborne and ground-based eddy covariance is in the averaging technique (Gioli et al, 2004). It has been found that there is a correlation between vertical air motion and aircraft ground speed, causing some type of turbulent structures being sampled more densely than others (Crawford et al., 1993); this can introduce bias up to 20% in the fluxes computed simply by using a time average. Hence, turbulent fluctuations (wind and associated scalars) are calculated using averages calculated over space (per meter) rather than over time (per second). This ''spatial average'' is defined, for instance for the vertical wind component w, by the following equation (Crawford et al., 1993):

$$\bar{w} = \frac{1}{\bar{S}T} \sum_i w_i S_i \Delta t \qquad (1)$$

where S is the instantaneous ground speed of the aircraft, $\bar{S}$ the mean speed, Dt time increment, and T total time. A similar averaging procedure is applied to all the variables involved in the covariance calculation

The definition of a proper averaging length I critical to ensure that all significant flux-carrying wavelengths are taken into account. Such a length depends on the flying altitude, on the surface roughness, and on atmospheric stability. Desjardins et al. (1989) have used the cumulative integral of the cospectrum to determine the frequency at which there is no more contribution to the covariance. The reciprocal of this frequency is the minimum averaging time necessary to include all the flux contributions.

When the covariance are computed using the above defined spatial averages, the cospectrum is computed toward a spatial frequency [m_1], whose reciprocal is the corresponding averaging length. The cumulative integral is an ogive defined by:

$$O_{xy}(f_0) = \int_{\infty}^{f_0} C_{xy}(f)df \qquad (2)$$

where x and y are two variables, and Cxy(f) the cospectrum of xy.

The ability of eddy covariance to resolve the higher frequencies carrying flux is limited by a number of factors, including the insufficient dynamic frequency response of the sensors and the length of the scalar path averaging. The dynamic response time of each sensor can be, in fact, not fast enough to adequately resolve the measurements up to the measured frequency, introducing some loss in the fluxes. Hence, proper correction factors must be applied as a function of the flying altitude, the wind speed, and the atmospheric stability. A simplified formula (Horst, 1997) has been applied in this study to estimate the attenuation of a scalar flux measurement made using linear, first order response scalar sensors with characteristic time constant t_c

$$\frac{\langle w'c' \rangle_m}{\langle w'c' \rangle} = \frac{1}{1 + \left(2\pi n_m \tau_c \overline{u}/z\right)^\alpha} \qquad (3)$$

where hw0c0im is the measured covariance between vertical wind velocity w and the scalar c, hw0c0i the expected covariance, u the air speed magnitude, z the flight height above ground level, and, for neutral and unstable conditions, a = 7/8 and nm = 0.085.